

---

# Novel dynamics of driven nonlinear resonators

Ian Grant Hendry

A thesis submitted in fulfilment of the requirements for the degree of  
Doctor of Philosophy in Physics,  
The University of Auckland, October 2020.

---

# Abstract

This Thesis is comprised of theoretical and experimental investigations designed to shed light on novel dynamics of nonlinear optical resonators. The theoretical investigations focus on cavity soliton (CS) dynamics in the presence of pulsed or amplitude modulated driving fields, while the experimental investigation focusses on frequency comb generation in second-order nonlinear microresonators.

First, we describe theoretical investigations into the dynamics of CSs in the presence of amplitude inhomogeneities of the driving field (such as pulsed driving) where the repetition rate of the inhomogeneity and the soliton are synchronised. We show that, in contrast to phase inhomogeneities, CSs are attracted towards (and trapped to) specific values of the driving field. We link our findings to a spontaneous symmetry breaking instability that physically arises from a competition between coherent driving and nonlinear propagation effects. We then consider the impact due to the presence of desynchronization between the CS and the repetition rate of the inhomogeneity. We show that the trapping positions can be manipulated and even erased, such that single-soliton operation can be assured. Further investigation into the interplay of this desynchronization and stimulated Raman scattering has allowed us to explain recent experimental observations.

The experimental portion of this Thesis focusses on the demonstration of internally pumped optical parametric oscillations in a lithium niobate microresonator. We demonstrate through numerical simulations that frequency combs can form around the pump and the second harmonic in a doubly resonant second order nonlinear microresonator. We then report on our experimental method for comb generation in a naturally phase matched lithium niobate microresonator by thermally tuning the birefringence of the crystal. Our observations of cascaded internally pumped optical parametric oscillation producing sidebands around the pump and the second harmonic bring us one step closer to achieving full comb generation in quadratically nonlinear optical microresonators.



# Acknowledgements

First, I would like to express my most heartfelt thanks to my supervisor, Miro Erkintalo, and my co-supervisors Stuart Murdoch and Stéphane Coen. To work under a world class group of supervisors has been a truly world-class experience. Your valuable guidance over the course of my study, be it necessary criticisms or fervent support, has made the most challenging accomplishment in my life the most rewarding as well.

I would also like to thank the postdocs that helped me when I was out of my depth in the lab. Bruno Garbin, Yiqing Xu and Vincent Ng, you always made time to share your vast wealth of knowledge and experience with myself and others.

To Harald Schwefel and Luke Trainor of The University of Otago, thank you for you never ending hospitality. Your willingness to accommodate me on visits to your university, so that I could learn from an extremely knowledgeable research group, made my research possible.

I must also acknowledge the other students of our research group, former and current, that shared time with me during my journey and offered support, debate, discussion, and humour, Alexander Nielsen, Noel Sayson, Toby Bi, Karen Webb, Yadong Wang, Andrew Su, and Max Li. I would also like to extend this acknowledgment to the people that I had the pleasure of sharing an office with, Nikolett Némit, Darcey Graham and Alexander Nielsen, again.

A very special thanks goes to the Rutherford Discovery Fellowship for providing me with a PhD scholarship.

To friends of mine that have supported me without knowing what I've been doing for nearly four years, I would like to give you all a big thanks. The distractions and comedic relief is all that kept me sane at times.

The last thanks is the largest and it goes out with love to my family. To Mom, and Dad, your endless support and unwavering belief that I am capable of doing anything I work hard at has made me who I am today. The shining example of work ethic and capability that the two of you represent is the most powerful driving

## IV

force in every one of my endeavours. And to my sister Leah, you've always been a role model to me in so many ways. Your drive and determination has always been a inspiration.



# Contents

1	INTRODUCTION	1
2	FUNDAMENTAL CONCEPTS	5
2.1	Electromagnetic waves . . . . .	5
2.2	Chromatic dispersion . . . . .	7
2.3	Birefringence . . . . .	8
2.4	Dielectric waveguides . . . . .	9
	2.4.1 <i>Waveguide modes</i> . . . . .	10
	2.4.2 <i>Waveguide dispersion</i> . . . . .	10
2.5	Nonlinear optics . . . . .	11
	2.5.1 <i>Nonlinear polarization</i> . . . . .	11
	2.5.2 <i>Second-order nonlinearity</i> . . . . .	12
	2.5.3 <i>Third-order nonlinearity</i> . . . . .	14
	2.5.4 <i>Light propagation in nonlinear optical waveguides</i> . . . . .	16
2.6	Optical resonators . . . . .	19
	2.6.1 <i>Linear resonator properties</i> . . . . .	19
	2.6.2 <i>Linear cavity response</i> . . . . .	20
3	KERR CAVITY DYNAMICS	25
3.1	Impact of Kerr nonlinearity on cavity resonances . . . . .	25
3.2	Lugiato-Lefever equation . . . . .	26
3.3	Numerical methods . . . . .	28
	3.3.1 <i>Split-step Fourier method</i> . . . . .	29
	3.3.2 <i>Newton-Raphson method</i> . . . . .	30
3.4	Intracavity modulation instability . . . . .	31
3.5	Temporal Kerr cavity solitons . . . . .	32
3.6	Cavity solitons in the presence of driving field inhomogeneities . . . . .	34

3.6.1	<i>Illustrative numerical simulations of phase modulation trapping</i> . . . . .	35
3.6.2	<i>Theory of cavity soliton plasticity</i> . . . . .	37
4	INTENSITY TRAPPING OF CAVITY SOLITONS	41
4.1	Numerical model . . . . .	42
4.2	Illustrative simulations . . . . .	43
4.3	Intensity-modulation-induced drift rate . . . . .	49
4.3.1	<i>Physics of cavity soliton motion</i> . . . . .	51
4.4	Summary . . . . .	54
5	IMPACT OF DESYNCHRONIZATION ON INTENSITY TRAPPING OF TEMPORAL CAVITY SOLITONS	55
5.1	Numerical model . . . . .	56
5.2	Illustrative simulations . . . . .	57
5.3	Detuning dependent dynamics and effect of stimulated Raman scattering . . . . .	64
5.4	Summary . . . . .	69
6	INTERNALLY PUMPED OPTICAL PARAMETRIC OSCILLATION IN $\chi^{(2)}$ MICRORESONATORS	71
6.1	Illustrative simulations of a doubly resonant $\chi^{(2)}$ cavity . . . . .	73
6.2	Experimental methods and results . . . . .	75
6.3	Summary . . . . .	82
7	CONCLUSIONS	83
	BIBLIOGRAPHY	1

# List of Figures

2.1	The refractive index $n$ and the group index $n_g$ of fused silica glass . . .	8
2.2	Waveguide schematics . . . . .	10
2.3	Schematic of SHG and PDC . . . . .	13
2.4	Schematic of FWM . . . . .	15
2.5	Schematic of an optical resonator . . . . .	20
2.6	Linear cavity resonances . . . . .	21
3.1	Nonlinear cavity resonances . . . . .	26
3.2	MI and CS branches . . . . .	32
3.3	LLE detuning scan of Kerr system . . . . .	33
3.4	CS phase trapping . . . . .	36
3.5	Inner product values . . . . .	39
4.1	Numerical simulation of CS moving away from the driving pulse peak	44
4.2	Plots demonstrating desired trapping value for a given detuning . . . .	45
4.3	Plots using co-sinusoidal driving to investigate dependence of trapping on local gradient . . . . .	46
4.4	Numerical simulations results demonstrating the detuning dependence of the trapping value . . . . .	48
4.5	Cavity soliton symmetry breaking bifurcation curve for a Gaussian driving field . . . . .	49
4.6	Colour plot demonstrating dependence of drift coefficient $a$ on driving amplitude and detuning . . . . .	51
4.7	Simulation results from an Ikeda-like cavity map at the trapping position	52
5.1	Demonstration of trapping in the absence of desynchronization . . . .	58
5.2	Numerical simulation demonstrating the effect of desynchronization on CS trapping at high detuning . . . . .	60

5.3	Numerical simulation demonstrating the effect of desynchronization on CS stability . . . . .	61
5.4	Numerical simulation demonstrating the effect of desynchronization on CS trapping at low detunings . . . . .	63
5.5	Colour plot the effect of desynchronization on the detuning dependence of CS existence . . . . .	66
5.6	Colour plot the combined effects of SRS and desynchronization on the detuning dependence of CS existence . . . . .	68
6.1	Schematic illustration of the generation of spectral sideband . . . . .	73
6.2	Proof of concept numerical simulation of sideband formation . . . . .	75
6.3	Schematic illustration of the experimental setup . . . . .	76
6.4	Scanning dynamics . . . . .	77
6.5	Experimental steady state sideband formation near and far around fundamental . . . . .	79
6.6	Experimental measurement of dual sideband formation around fundamental and second harmonic . . . . .	80
6.7	Experimental measurement of cascaded PDC . . . . .	81

# Abbreviations

BPF	band-pass filter
CS	cavity soliton
CW	continuous-wave
ECDL	external-cavity diode laser
EM	electromagnetic
FSR	free-spectral range
FWM	four-wave mixing
LLE	Lugiato-Lefever equation
MI	modulation instability
NLSE	nonlinear Schrödinger equation
OPO	optical parametric oscillation
OSA	optical spectrum analyser
PC	polarization controller
PD	photodetector
PDC	parametric down conversion
PID	proportional–integral–derivative controller
SFG	sum frequency generation
SH	second harmonic
SHG	second harmonic generation
SPM	self-phase modulation
SRS	stimulated Raman scattering
TE	transverse electric
TM	transverse magnetic
TWM	three-wave mixing
WGM	whispering-gallery-mode
XPM	cross-phase modulation
YDFA	ytterbium-doped fibre amplifier
ZDW	zero dispersion wavelength



# Chapter 1

## Introduction

With the introduction of light amplification by stimulated emission of radiation (ubiquitously known as the laser) in 1960 [1], a door opened on a new chapter of scientific discovery and advancement. The introduction of lasers was quickly followed by the demonstration of nonlinear optical processes. Second harmonic generation was achieved in 1961 [2] with other frequency conversion processes following closely [3, 4]. The high intensity light that can be produced with lasers has facilitated the investigation of many novel nonlinear phenomena [5–7].

The culmination of research into nonlinear frequency conversion techniques is the generation of broad-band spectra of light. A narrow-band pulse of light in the frequency domain corresponds to a broad temporal pulse and vice-versa. Launching this temporally broad pulse into a highly nonlinear waveguide with strong Kerr nonlinearity causes it to compress. As the pulse compresses temporally, its spectrum broadens. The result is a spectrum of light that can span as much as an octave, known as a supercontinuum [8–10]. Repeating this pulse to create a train of pulses forces this broad spectrum to form into thousands of discrete lines in the frequency domain, with the frequency separation determined by the pulse repetition rate. These so called frequency combs have revolutionised the field of precision metrology, acting as rulers which allow for the measurement of unknown frequencies of light with incredible precision. Indeed, the 2005 Nobel prize was partially awarded to Theodor Hänsch [11] and John Hall [12] for work on frequency combs and the subsequent contributions to the field of spectroscopy.

Many early combs and currently commercially available frequency comb sources are made using mode-locked lasers [13]. Although any method which generates a train of pulses can allow one to realise a frequency comb, an intriguing concept is that of a repeating train of *soliton* pulses. Solitons are wave packets that

can maintain constant properties such as shape and velocity during propagation. They have been observed and studied for over a century in such diverse physical systems as biology [14], plasmas [15], nonlinear optics [16] and cold atoms [17]. The first recorded observation is credited to John Scott Russell in Scotland in 1834 [18] when a horse-drawn canal boat stopped abruptly. He witnessed a wave of water created by the boat "*which continued its course along the channel apparently without change of form or diminution of speed.*" Mathematically, solitons are generally associated with exact solutions to "*completely integrable*" nonlinear models describing many varied physical systems [19].

Though solitons have been observed and studied in many varied fields of research, optics has become a growing front from which to study solitons due to the ease with which optical solitons can be studied. The *optical* soliton can manifest temporally (spatially) due to the competing effects of dispersion (diffraction) spreading the wave packet and self-phase modulation (self-focusing) compressing it. In this Thesis, we are specifically interested in temporal solitons which arise due to the effects of dispersion and Kerr nonlinearity. Such solitons can be classified into two categories depending on the physical system in consideration. In a *conservative* system, solitons persist due to a *single* balance between the dispersion and the Kerr nonlinearity [20] as little (or no) dissipation of energy occurs. In a *dissipative* system, however, we must also consider the notion that energy will be both lost and gained during propagation. These dissipative temporal solitons are analogous to localised dissipative structures that have been widely studied in a number of non-equilibrium systems [21] and persist due to a precise *double*-balance of effects. Specifically, in addition to maintaining constant shape through the balancing of dispersion and Kerr nonlinearity, dissipative solitons also maintain constant energy due to the cancellation of dissipation by some form of energy inflow.

In this Thesis, we are interested in a particular class of temporal dissipative solitons known as temporal Kerr cavity solitons (CSs). These are pulses of light that can persist in passive ring resonators that are coherently driven with laser light [22]. Temporal CSs were first studied in macroscopic fiber ring cavities in 2010 in the context of bits of information stored in an optical buffer [23], demonstrating that an optical soliton could be excited in a passive, driven Kerr resonator and recirculate indefinitely. By extracting a portion of the intracavity field from the resonator, the CS produces an identical pulse with every trip around the cavity, forming a stable train of pulses at the output. As noted above, this train of pulses

corresponds to a coherent optical frequency comb in the spectral domain [24]. The ability to use CSs as sources of optical frequency combs has attracted significant attention in the context of another resonator platform: high-Q monolithic whispering-gallery-mode microresonators.

Oxford dictionary defines a whispering gallery as "*a gallery or dome with acoustic properties such that a faint sound may be heard round its entire circumference*". This acoustic phenomenon can be applied to optics by injecting light into a circular medium which allows light to travel around its circumference in a tightly confined modal area with very low loss. The ultra low loss and large nonlinearity of these resonators has enabled many nonlinear effects – including second harmonic generation, third harmonic generation, four-wave mixing and optical parametric oscillation – to be observed at very low pump powers [25–30]. The generation of broadband frequency combs from a single continuous wave (CW) laser light source in an optical whispering-gallery-mode microresonator was first achieved in a Kerr microresonator in 2007, though the system was not operating in the CS regime, but rather in a noisy regime corresponding to so-called chaotic modulation instability patterns. The association with CSs was not demonstrated in microresonators until 2014 [24]. With this, however, the first soliton-based microresonator frequency combs were generated and displayed high coherence and stability, motivating new efforts to understand the dynamics of CSs in passive, driven Kerr microresonators.

Kerr CS-based microresonator frequency combs have shown immense potential for a wide range of applications, from telecommunications [31] to optical ranging (LIDAR) [32]. Nonetheless, they suffer from certain shortcomings. First, CW driving of CSs exhibits inherently low conversion efficiency from the driving field to the CS. The localised nature of the CS means that it will only interact with the driving field in its vicinity while the field in the rest of the cavity serves little purpose. The homogeneity of a CW driving field also makes it difficult to lock the repetition rate of the CS to an RF signal. Phase modulation of the driving field has been identified as one method for controlling the positions of CSs, as well as their repetition rate [33], though this method does not address the conversion efficiency. Intensity modulated (or pulsed) driving fields aim to provide the benefits offered by phase modulation by locking CSs to RF signals while also increasing the pump to CS conversion efficiency [34].

Second, due to the nature of the frequency mixing process which dominates Kerr frequency comb generation, sidebands are only generated around the pump wavelength [35]. This limits spectral access to regions where pump light can easily

be generated. It has been recently shown that this problem can be overcome in resonators dominated by the  $\chi^{(2)}$  nonlinearity. In such second-order nonlinear resonators, the pump can undergo a conversion process (such as second harmonic generation) to generate a second frequency capable of generating a frequency comb in a distant region of the spectrum. This was first achieved in macroscopic resonators in 2015 [36], but it has also been proposed that these results can be achieved in microresonators [37, 38], bringing with them the aforementioned benefits that they offer.

In this Thesis, we will investigate novel dynamics of nonlinear resonators which are applicable over a broad range of research platforms. We will shed light on some of the more nuanced approaches towards the use of CSs as the basis for optical frequency combs through an investigation into CS dynamics in the presence of driving fields with inhomogeneous amplitude profiles (such as pulsed pumping). We will also explore new ways of generating frequency combs in hard to reach spectral regions through the use of second-order nonlinear microresonators. The main body of this Thesis is made up of six chapters that are presented as follows. Chapter 2 covers the fundamental concepts that one would need to grasp before tackling the remainder of the work. This includes the basics of electromagnetic waves, linear and nonlinear optical effects, dielectric waveguides, the behaviour of light as it propagates through optical waveguides and the linear properties of optical resonators. Chapter 3 details Kerr cavity dynamics which underpin CSs, as well as the ability to manipulate temporal CSs via (phase) inhomogeneities in the CW driving field. Chapter 4 investigates and describes the interaction between temporal CSs and *amplitude* modulated (or pulsed) driving fields and details the phenomenon of intensity trapping in synchronously driven resonators [39]. Building on this, Chapter 5 investigates the limits of CS stability in the presence of desynchronization between the solitons and driving field [40]. Chapter 6 investigates the ability of second-order nonlinear microresonators to produce frequency combs via cascaded second-order phenomena. We then describe our methods for experimentally demonstrating this ability and our detection of initial stages of comb formation [41].

## Chapter 2

# Fundamental concepts

The purpose of this Chapter is to outline the basic principles of electromagnetism and optics that we will be drawing on throughout this Thesis. We will lay out the basic physics of electromagnetic radiation and nonlinear optics, as well as dielectric waveguides and optical resonators. This Chapter will also detail how we model such systems in order to grasp the rich dynamics of nonlinear optical resonators.

### 2.1 Electromagnetic waves

An electromagnetic wave (EM wave) is the synchronized oscillation of electric and magnetic fields over time created by the acceleration of electrically charged particles. Maxwell's equations form a set of coupled partial differential equations that govern all electromagnetic phenomena [42]

$$\begin{aligned}\nabla \cdot \vec{D} &= \rho_f, \\ \nabla \cdot \vec{B} &= 0, \\ \nabla \times \vec{E} &= -\frac{\partial \vec{B}}{\partial t}, \\ \nabla \times \vec{H} &= \vec{J}_f + \frac{\partial \vec{D}}{\partial t}.\end{aligned}$$

Here,  $\vec{D}$  is the electric displacement field,  $\vec{B}$  is the magnetic field,  $\vec{E}$  is the electric field,  $\vec{H}$  is the magnetic displacement field,  $\vec{J}_f$  is the density of free current and  $\rho_f$  is the density of free charge. The electric and magnetic displacement fields are

related to the electric and magnetic field via the relationships

$$\vec{D} = \epsilon_0 \vec{E} + \vec{P}, \quad (2.1)$$

$$\vec{H} = \frac{1}{\mu_0} \vec{B} - \vec{M}, \quad (2.2)$$

where  $\vec{P}$  and  $\vec{M}$  are the induced electric polarization and magnetization of the medium respectively,  $\mu_0$  is the vacuum permeability and  $\epsilon_0$  is the permittivity of vacuum. The electric polarization and magnetization occur due to the electromagnetic field interacting with the electric charges and magnetic dipoles associated with individual atoms of the medium.

For the purposes of this Thesis, we will be focusing on the electric field  $\vec{E}$ , though we know that there is always an inseparable associated magnetic field. We will also be interested in dielectric, non-magnetic materials with no free charge or currents such that  $\rho = 0$ ,  $\vec{J}_f = 0$  and  $\vec{M} = 0$ . Because the electric polarization of the medium does not occur instantaneously, the induced electric polarization  $\vec{P}$  can be expressed as the convolution of a time-dependent susceptibility  $\chi(t)$  and the electric field [20]

$$\vec{P}(\vec{r}, t) = \epsilon_0 \int_{-\infty}^t \chi(t - t') \vec{E}(\vec{r}, t') dt'. \quad (2.3)$$

This representation holds true for small electric field amplitudes only, and  $\vec{P}$  will be redefined shortly to accommodate high electric field amplitudes.

From Maxwell's equations and the definitions of the electric and magnetic field displacements, we are able to obtain a second-order partial differential equation (wave equation) to describe the propagation of an electromagnetic wave in a medium [20]:

$$\nabla^2 \vec{E} = \frac{1}{c^2} \frac{\partial^2}{\partial t^2} \vec{E} + \mu_0 \frac{\partial^2}{\partial t^2} \vec{P} \quad (2.4)$$

where  $\nabla^2$  is the Laplace operator and  $c = 1/\sqrt{\mu_0 \epsilon_0}$  is the speed of light in vacuum. The simplest solution to Eq. (2.4) is a plane wave of the form:

$$\vec{E}(\vec{r}, t) = \vec{A} e^{(i\omega t - i\vec{k} \cdot \vec{r})} \quad (2.5)$$

where  $\vec{A}$  is the amplitude of the field,  $\omega$  is the angular frequency and  $\vec{k}$  is the wave vector. The direction of the electric field vector  $\vec{E}$  is known as the *field* polarization and should not be confused with the *electric* polarization  $\vec{P}$  of the medium. The wave vector  $\vec{k}$  indicates the direction of propagation and the phase delay per unit length. The magnitude of  $\vec{k}$  is the angular wavenumber and is defined as

$$k = \frac{2\pi}{\lambda}, \quad (2.6)$$

where  $\lambda$  is the wavelength in the medium. This wavenumber is related to angular frequency  $\omega$  according to the dispersion relation

$$\frac{\omega}{k} = \frac{1}{\sqrt{\mu_0 \epsilon_0 (1 + \tilde{\chi}(\omega))}} = v_p, \quad (2.7)$$

where  $\tilde{\chi}(\omega)$  is the Fourier transform of the time dependent susceptibility  $\chi(t)$  and  $v_p$  is the *phase* velocity. Of course, in a vacuum  $\chi = 0$  and the phase velocity becomes the speed of light in a vacuum,  $c$ . All other media are characterised by their refractive index,  $n(\omega) = c/v_p(\omega)$ , which is a ratio of the speed of light in a particular medium and the speed of light in a vacuum. Therefore we can write the refractive index as

$$n(\omega) = \sqrt{1 + \tilde{\chi}(\omega)}. \quad (2.8)$$

## 2.2 Chromatic dispersion

Chromatic dispersion refers to the frequency dependence of the refractive index of matter, and hence the phase velocity of EM waves. This can be easily seen in the frequency dependence of the linear electric susceptibility  $\tilde{\chi}(\omega)$  and therefore the frequency dependence of  $n(\omega)$  in Eq. (2.8). This frequency dependent refractive index leads to a frequency dependent phase velocity  $v_p(\omega)$ . The refractive index  $n(\omega)$  accurately describes the velocity of monochromatic light of the form of Eq. (2.5). Absorption around specific atomic resonance frequency bands are the root cause of chromatic dispersion. At frequencies far from these resonance frequencies, the refractive index can be well approximated by the Sellmeier equation [20]

$$n(\omega) = \sqrt{1 + \sum_{j=1}^m \frac{B_j \omega_j^2}{\omega_j^2 - \omega^2}}, \quad (2.9)$$

where  $B_j$  represents the strength of an absorption band centred at  $\omega_j$ . Figure 2.1 shows how the refractive index  $n$  for silica glass changes with frequency.

In reality, electromagnetic waveforms are more complicated than simple plane waves described by Eq. (2.5), exhibiting temporal and spatial variances. These waveforms are made up of many frequencies, each travelling at a different phase velocity. Wave packets or pulses of light containing many different frequencies travel at the *group* velocity  $v_g$  which is defined by the group refractive index  $n_g$  [20], which is shown in Fig. 2.1, as

$$v_g = \frac{c}{n_g} = \frac{c}{\left(n + \omega \frac{dn}{d\omega}\right)}. \quad (2.10)$$

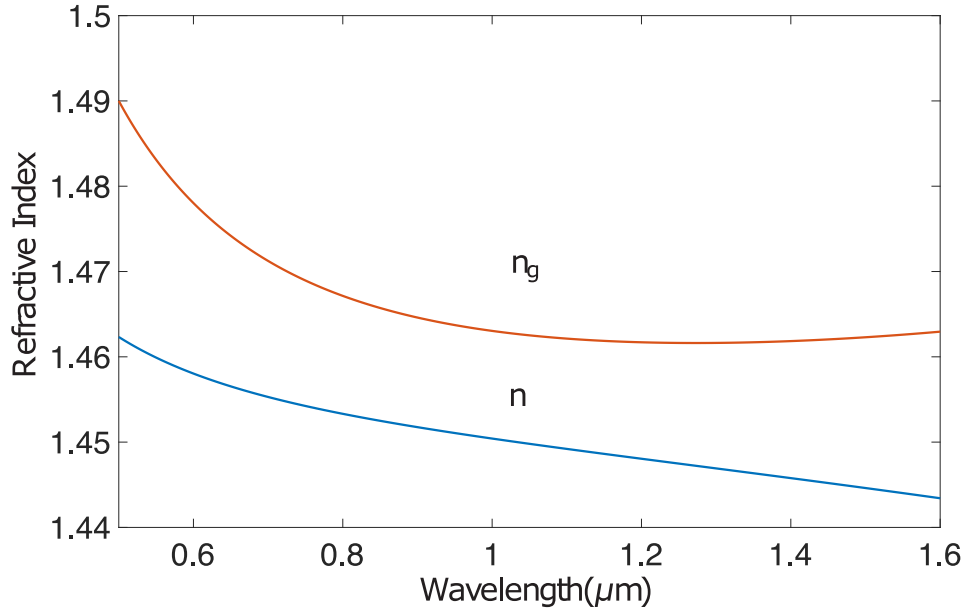


Figure 2.1: The refractive index  $n$  and the group velocity index  $n_g$  of fused silica glass calculated from Eq. (2.9) and Eq. (2.10).

In general  $dn/d\omega \neq 0$  due to dispersion. Therefore, the group refractive index  $n_g$  differs from the refractive index  $n$  for a single frequency field (as shown in Fig. 2.1), and accordingly, the group velocity differs from the phase velocity. It is also important to note that the refractive index of a material can be effected by macroscopic environmental variables. Factors such as temperature, pressure, stress and electric and magnetic fields can all have an effect, and can be accounted for with additional terms to Eq. (2.9).

### 2.3 Birefringence

Birefringence is a property of materials having polarization dependent refractive indices. In an anisotropic material, the susceptibility is not uniform in all directions. In this case, the linear susceptibility  $\chi$  should be understood as a tensor of rank 2 and the dielectric polarization  $\vec{P}$  arises as a tensor product between that tensor and the electric field vector. It follows that different orientations of the electric field in an anisotropic medium will experience different indices of refraction. This phenomenon is known as birefringence.

In order to analyse EM wave propagation in birefringent materials it is useful to be able to describe the polarization of the optical field with respect to the optical axis of the material. In this research, we are interested in so-called uniaxial birefringent crystals. Such crystals exhibit a single optical axis which is oriented in the direction along which propagating light will not experience birefringence. This axis exhibits a uniform refractive index,  $n_o$  for ordinary, for all polarizations. In any other propagation direction, the refractive index experienced by light polarized parallel to this axis is denoted ordinary ( $n = n_o$ ) and the refractive index experienced by light polarized perpendicular to the optical axis is denoted extraordinary ( $n = n_e$ ). The birefringence of the material (largely crystals with non-cubic structures) is quantified as the difference between the extraordinary and ordinary refractive indices,  $\Delta n = n_e - n_o$ , and can be positive or negative. The birefringence of a material can also depend on external factors which affect the structure of the crystal such as electric fields or temperature.

## 2.4 Dielectric waveguides

In this Thesis, we will be focussing on optical phenomena occurring in resonators that can be understood to be made out of dielectric waveguides. Such waveguide devices have assumed major roles in today's society, enabling technologies such as optical fibre telecommunications. A waveguide is a structure that confines the spatial region in which a wave can travel. In optics, this is typically achieved via the process of total internal reflection (TIR). When light is travelling in a transparent dielectric material that is surrounded by a material of lower refractive index ( $n_1 > n_2$  in Fig. 2.2), light with a direction of propagation which satisfies TIR criteria will remain in the dielectric. The dimensions of the waveguide can be set to confine the guided light in one dimension as in planar waveguides or two dimensions such as in optical fibers and rectangular waveguides. Shown below in Fig. 2.2 are examples of such dielectric waveguides.

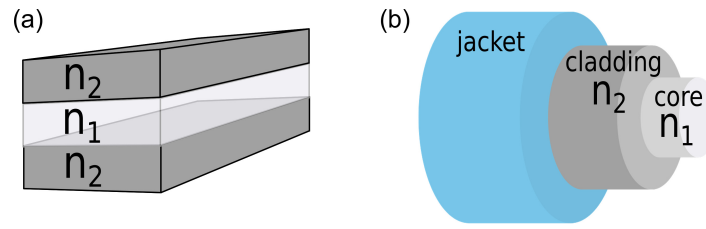


Figure 2.2: Schematic showing refractive index profiles for common waveguide types of (a) a slab (planer) waveguide which confines light in one dimension and (b) cross section of an optical fibre which confines the light in two dimensions in its core.

### 2.4.1 Waveguide modes

Full analysis of waveguides requires application of Maxwell's equations [20]. For light of a single frequency and polarization, it is useful to view the field distribution in a plane perpendicular to the direction of propagation (e.g. a circular cross section of an optical fiber). A given optical waveguide admits particular transverse profiles that do not change as they propagate. Such field configurations are known as the modes of the waveguide. Mathematically, a mode of a waveguide can be written as

$$\vec{E}(x, y, z, t) = A(z, t)\vec{F}(x, y)e^{i\omega t - i\beta z}, \quad (2.11)$$

where  $\vec{F}(x, y)$  corresponds to the transverse profile which is invariant with the propagation direction  $z$ , while  $A(z, t)$  is a slowly-varying amplitude. Here  $\beta$  is known as the propagation constant and can be understood as an effective wave number and can be written as:

$$\beta = n_{\text{eff}} \frac{\omega}{c}, \quad (2.12)$$

where  $n_{\text{eff}}$  is an effective refractive index. The mode profiles  $\vec{F}(x, y)$  and propagation constants  $\beta$  can be obtained by solving the wave equation, Eq. (2.4) with boundary conditions of the waveguide geometry.

### 2.4.2 Waveguide dispersion

The refractive index experienced by an electromagnetic wave is frequency dependent due to material dispersion of the medium as discussed earlier. In waveguides, there is an additional frequency dependence due to the fact that the mode *area* itself is frequency dependent. Because of material and waveguide dispersion, the

mode propagation constant  $\beta$  depends on frequency ( $\beta \equiv \beta(\omega)$ ). It is conventional to represent the frequency dependence of the propagation constant by means of a Taylor series expansion about a reference frequency  $\omega_0$ :

$$\beta(\omega) = n_{eff} \frac{\omega}{c} = \beta_0 + \beta_1(\omega - \omega_0) + \frac{\beta_2}{2}(\omega - \omega_0)^2 + \frac{\beta_3}{6}(\omega - \omega_0)^3 + \dots \quad (2.13)$$

where  $\beta_m = (d^m \beta / d\omega^m)_{\omega=\omega_0}$  for  $m = 0, 1, 2, \dots$ . The constant  $\beta_1$  relates to the group velocity:

$$\beta_1 = \frac{1}{c} \left( n_{eff} + \omega \frac{dn_{eff}}{d\omega} \right) = \frac{n_g}{c} = \frac{1}{v_g}. \quad (2.14)$$

The next coefficient,  $\beta_2$ , is the group velocity dispersion and describes how a pulse broadens as it propagates through a medium:

$$\beta_2 = \frac{1}{c} \left( 2 \frac{dn_{eff}(\omega)}{d\omega} + \omega \frac{d^2 n_{eff}(\omega)}{d\omega^2} \right). \quad (2.15)$$

Under normal dispersion (positive  $\beta_2$ ) longer wavelength components travel faster than shorter, and under anomalous dispersion (negative  $\beta_2$ ) the opposite is true. The wavelength at which  $\beta_2 = 0$  is known as the zero dispersion wavelength (ZDW). Higher orders of dispersion ( $\beta_k$  for  $k > 2$ ) can generally be ignored far from the ZDW. Additionally, it is useful to define a parameter known as the *dispersion length*. If we consider a Gaussian pulse envelope of width  $\tau_0$ , this length is given by

$$L_D = \frac{\tau_0^2}{|\beta_2|}, \quad (2.16)$$

which is the length over which a Gaussian pulse envelope will spread by a factor of  $\sqrt{2}$  under the influence of second order dispersion alone [20].

## 2.5 Nonlinear optics

In Eq. (2.3) we assumed the material polarization to be linearly dependent on the electric field. This relationship is only accurate for comparatively small field amplitudes. For large electric fields, the relationship becomes nonlinear, and gives rise to a variety of effects [20]. The branch of optics that deals with such nonlinear light-matter interactions is known as nonlinear optics.

### 2.5.1 Nonlinear polarization

All media are susceptible to electric polarization (different from the polarization of the optical field). This occurs because the polarization density of the medium is

dependent on the electric field of the incident light, creating a polarization wave that travels through the medium. At low powers, the effect is *linearly* proportional to the electric field strength, as in Eq. (2.3); however, when light of sufficient intensity propagates in a medium, *nonlinear* effects begin to play a role. The total induced polarization  $P$  in this case can be expressed as a power series of the incident electric field  $E$ :

$$P = \epsilon_0 \sum_{k=1}^{\infty} \chi^{(k)} E^k, \quad (2.17)$$

where  $\chi^{(k)}$  is the  $k^{\text{th}}$  order susceptibility with rank  $k + 1$  of the material. Equation (2.17) hides a number of simplifications of the complicated underlying physics and mathematics. In general, and as in Eq. (2.3),  $P$  and  $E$  are vectors and each term of the sum on the right hand side represents a tensor convolution of the susceptibility tensor and the electric field vector. In the scalar approximation however, where the electric field is linearly polarised and the susceptibility tensor has only one dominant (diagonal) term, Eq. (2.17) becomes valid under the assumption of instantaneous material response. The first-order susceptibility,  $\chi^{(1)}$  describes the *linear* susceptibility from the previous Section and is responsible for such common optical phenomena as reflection, refraction and chromatic dispersion. When non-zero, the higher-order effects give rise to nonlinear effects as the induced electric polarization is a nonlinear function of the electric field. This Thesis will rely heavily on phenomena arising from the second and third-order nonlinear susceptibilities,  $\chi^{(2)}$  and  $\chi^{(3)}$ . Nonlinearities of order above 3 have negligible impact with power levels used in our research, and can be ignored. In what follows, we will briefly summarise the most important nonlinear effects pertinent to this Thesis.

### 2.5.2 Second-order nonlinearity

We first discuss the second-order nonlinear susceptibility  $\chi^{(2)}$ . This susceptibility is responsible for important three-wave mixing (TWM) processes and arises in non-centrosymmetric materials, which do not possess inversion symmetry. It is important to note that the third-order nonlinearity  $\chi^{(3)}$ , is still present in such materials, though  $\chi^{(2)}$  nonlinearities can be orders of magnitude stronger than their third-order counterparts, and tend to dominate the nonlinear response when present. What follows are the second-order nonlinear effects that will be pertinent to our studies.

### 2.5.2.1 Second harmonic generation

Second harmonic generation (SHG) is the TWM phenomenon by which a pump at frequency  $\omega_p$  induces a polarization wave in a medium that oscillates at the second harmonic (SH) frequency,  $\omega_{SH} = 2\omega_p$ . Second harmonic generation is a TWM process due to the fact that it requires two pump photons to generate one second harmonic photon. This process is demonstrated by the diagram shown in Fig. 2.3(a). For efficient SHG momentum must be conserved, meaning that the wavenumber mismatch,  $\Delta k = 2k(\omega_p) - k(2\omega_p)$ , must equal zero. Remembering that  $k = \omega_p/v_p$  and  $v_p = c/n$ , our wavenumber mismatch condition requires  $n(\omega_p) = n(2\omega_p)$ . Due to chromatic dispersion, it may not be straightforward to satisfy the phase-matching condition. With the pump and second harmonic travelling at different phase velocities, the second harmonic generated at one point will destructively interfere with previously generated second harmonic. However, methods of achieving this condition have been developed and will be discussed in detail later.

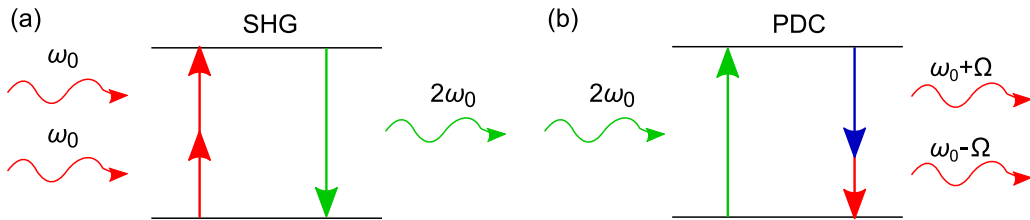


Figure 2.3: (a) during SHG two pump photons at  $\omega_0$  combine to generate one photon at  $2\omega_0$ . (b) during PDC one pump photon at  $\omega_p = 2\omega_0$  is broken into two in order to form sidebands around  $\omega_0$  which are spaced by  $\Omega$ .

### 2.5.2.2 Parametric down conversion

Parametric down conversion (PDC) is the second-order nonlinear process by which a single photon of frequency  $\omega_p = 2\omega_0$  can break down into two photons of lower frequencies  $\omega_s$  and  $\omega_i$  such that  $\omega_p = \omega_s + \omega_i$ . These signal and idler frequencies are positioned such that  $\omega_s = \omega_0 + \Omega$  and  $\omega_i = \omega_0 - \Omega$ , as demonstrated by the diagram shown in Fig. 2.3(b). As is the case with SHG, momentum must also be conserved for PDC, requiring that  $k(\omega_p) = k(\omega_i) + k(\omega_s)$ . This phase matching condition determines the value of  $\Omega$  for given parameters.

### 2.5.3 Third-order nonlinearity

In materials with inversion symmetry such as silica glass, the even order susceptibility tensors vanish. For this reason, the lowest order, and therefore dominant, nonlinear susceptibility that these materials exhibit is the third-order,  $\chi^{(3)}$  susceptibility. This nonlinear susceptibility is capable of mixing four distinct waves, giving rise to such phenomena as four-wave mixing (FWM) and nonlinear refraction (Kerr effect). Just as  $\chi^{(2)}$  systems can give rise to SHG,  $\chi^{(3)}$  systems can give rise to third harmonic generation. As with second-order processes, phase matching must be achieved. However, in the systems we consider in this Thesis, third harmonic generation cannot generally be phase-matched, and hence plays no role in our work and will be neglected. In what follows we will describe the relevant third-order effects for our work.

#### 2.5.3.1 Intensity-dependent refractive index

We know that materials exhibit a frequency-dependent refractive index, but light of sufficient intensity also experiences an *intensity*-dependent refractive index:

$$n(\omega, I) = n_0(\omega) + n_2 I, \quad (2.18)$$

where  $n_0(\omega) = \sqrt{1 + \chi^{(1)}(\omega)}$  represents the linear dependency of the refractive index on the frequency of the light (chromatic dispersion),  $n_2 \propto \chi^{(3)}$  corresponds to the nonlinear refractive index (units of  $m^2/W$ ) and  $I$  is the electric field intensity,  $I \propto |E|^2$ . This nonlinear dependence of the refractive index on the intensity is known as the Kerr effect.

#### 2.5.3.2 Self-phase and cross-phase modulation

The intensity dependence of the refractive index leads to an intensity dependent phase shift of the electromagnetic wave propagating in a  $\chi^{(3)}$  material. As seen from Eq. (2.5), an EM wave propagating through a material of length  $L$  accumulates a phase shift  $\phi = kL = n(\omega)L\omega/c$ . Since the refractive index  $n(\omega)$  depends on intensity we see that the wave accumulates an intensity dependent, nonlinear phase shift. The nonlinear phase shift  $\phi_{NL}$  after propagating a distance  $L$  is given by

$$\phi_{NL} = \frac{\omega n_2 L}{c} I. \quad (2.19)$$

This phenomenon is known as *self-phase modulation* (SPM) as the electric field is modifying its own phase. There is another similar phenomenon that arises from

the Kerr effect in which a field at one carrier frequency,  $E_1$ , can cause a phase shift for a field at another carrier frequency,  $E_2$ . This is known as cross-phase modulation (XPM) and combining SPM and XPM gives the total accumulated nonlinear phase shift of each field as

$$\phi_{NL,1} = \frac{\omega n_2 L}{c} [I_1 + 2I_2], \quad (2.20a)$$

$$\phi_{NL,2} = \frac{\omega n_2 L}{c} [I_2 + 2I_1]. \quad (2.20b)$$

On the right hand side of these equations, the first term in the brackets refers to self-phase modulation while the second term is the cross-phase modulation. From this it is easy to see that XPM is twice as efficient as SPM.

### 2.5.3.3 Kerr four-wave mixing

Kerr four-wave mixing (FWM) is the process by which two photons of frequency  $\omega_1$  and  $\omega_2$  can be annihilated in order to create two new photons of frequencies  $\omega_3$  and  $\omega_4$  such that energy is conserved,  $\omega_1 + \omega_2 = \omega_3 + \omega_4$ , as shown in Fig. 2.4. In order to conserve momentum, the wavenumbers,  $k$ , must satisfy the condition  $k(\omega_1) + k(\omega_2) = k(\omega_3) + k(\omega_4)$ . As with TWM processes, this condition is known as the phase-matching requirement and enables efficient four wave mixing processes. Many other FWM processes exist, but phase-matching of these processes is generally not possible in the systems considered in this Thesis. Fortunately, the Kerr FWM process can be spontaneously phase-matched via SPM and XPM, giving it significant importance.

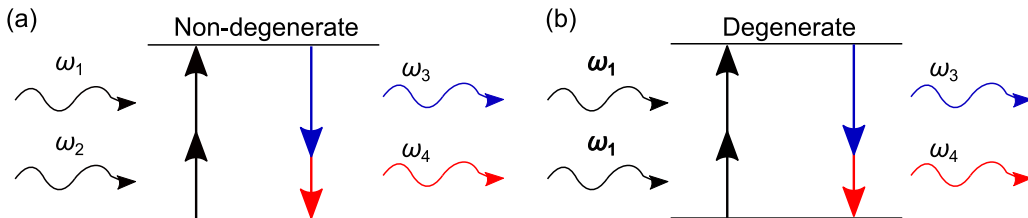


Figure 2.4: (a) during non-degenerate FWM two pump photons of different frequencies  $\omega_1$  and  $\omega_2$  (where  $\omega_1 - \omega_2 = \Omega$ ) combine to generate two photons of frequencies  $\omega_3 = \omega_1 + \Omega$  and  $\omega_4 = \omega_2 - \Omega$ . (b) during degenerate FWM two pump photons of the same frequency  $\omega_1$  combine to generate two new photons with frequencies of  $\omega_3 = \omega_1 + \Omega$  and  $\omega_4 = \omega_1 - \Omega$ .

The above descriptions pertain to a non-degenerate FWM process where all four frequency components are different, as shown in Fig. 2.4(a). However, degenerate Kerr FWM can also occur when two of the four mixed waves coincide, as

shown in Fig. 2.4(b). Here you can see that two pump photons of the same frequency produce one signal photon and one idler photon equally spaced from the pump. The time domain representation of this degenerate Kerr FWM is known as modulation instability (MI) and will be discussed in the context of optical cavities in Chapter 3.

#### 2.5.3.4 Stimulated Raman scattering

Another nonlinear effect that arises from the third-order nonlinear susceptibility is Raman scattering [5, 20]. Spontaneous Raman scattering occurs when a pump photon at  $\omega_p$  is inelastically scattered by a material resulting in part of the energy of the photon being transferred to the material. This can be understood as a photon-phonon coupling between the electric field and the vibrational modes in the material. The result is a Raman side band forming at a frequency of lower energy, Stokes photons of frequency  $\omega_s = \omega_p - \Omega$ , with the difference in energy between the pump photon and Stokes photon being transferred to a phonon of frequency  $\Omega$ . The reverse can also take place, allowing the pump photon to gain energy from a phonon to generate anti-Stokes photons at frequency  $\omega_a = \omega_p + \Omega$ . The scattering rate can be increased beyond that of the spontaneous case by injecting the Stokes or anti-Stokes photons along with the pump. This is known as stimulated Raman scattering (SRS) and can cause shifts in the spectrum of spectrally broad optical pulses.

#### 2.5.4 Light propagation in nonlinear optical waveguides

Nonlinear optical effects are particularly significant in waveguides, where the electric field is confined to a small area thus giving rise to large intensities. Indeed, an electromagnetic field can undergo significant temporal and spectral changes as it propagates through a nonlinear waveguide. To first order, as discussed in Subsection 2.4.1, the transverse mode profile remains constant while it is the slowly-varying field amplitude  $A(z, t)$  from Eq. (2.11) which changes. The Fourier transform of  $A(z, t)$  gives the corresponding changes in the EM wave spectrum. In this Thesis, we will be considering resonators which can be described as a waveguide that is looped on itself such that it begins and ends at the same position. To describe the dynamics of such systems, we need to have theoretical models which describe the evolution of electromagnetic waves as they propagate through a section of waveguide. The equations detailed in this Section only govern the evolution over a single pass of the waveguide, while the necessary boundary conditions will

be added in later Sections in order to describe the dynamics of the evolution in resonator configurations.

#### 2.5.4.1 Coupled equations for SHG in $\chi^{(2)}$ materials

The experiments to be described in Chapter 6 consider a resonator constructed of a  $\chi^{(2)}$  crystal and they operate under conditions where SHG is close to phase-matching. It can be shown [43] that the evolution of the slowly-varying intracavity fields  $A(z, t)$  and  $B(z, t)$  at frequencies of  $\omega_p$  and  $2\omega_p$  respectively, over a single round trip across the resonator obey the coupled equations:

$$\frac{\partial A}{\partial z} = -i\frac{\beta_{2A}}{2}\frac{\partial^2}{\partial\tau^2}A + i\kappa BA^*e^{-i\Delta\beta z}, \quad (2.21a)$$

$$\frac{\partial B}{\partial z} = -\Delta\beta_1\frac{\partial}{\partial\tau}B - i\frac{\beta_{2B}}{2}\frac{\partial^2}{\partial\tau^2}B + i\kappa A^2e^{i\Delta\beta z}, \quad (2.21b)$$

Here,  $A(z, \tau)$  and  $B(z, \tau)$  describe the electric field envelopes at position  $z$  along the waveguide with  $\tau = t - \beta_1 z$  being the time coordinate in the reference frame travelling at the group velocity of the envelope at  $\omega_p$  which we will refer to as the *fast time* frame. On the right hand sides of Eq (2.21a) and Eq. (2.21b),  $\Delta\beta = 2\beta(\omega_p) - \beta(2\omega_p)$  is the effective wave vector mismatch,  $\Delta\beta_1 = d\beta_1/d\omega|_{2\omega_p} - d\beta_1/d\omega|_{\omega_p}$  is the group-velocity mismatch and  $\beta_{2A,B} = d^2\beta_{2A,B}/d\omega^2|_{\omega_p,2\omega_p}$  are the group velocity dispersion coefficients at the fundamental and second-harmonic frequencies, respectively. The nonlinear coupling coefficient  $\kappa$  is normalised such that  $|A|^2$  and  $|B|^2$  are measured in Watts and it satisfies

$$\kappa = \frac{\sqrt{8}\omega_0\chi_{eff}^{(2)}}{\sqrt{c^3n_1^2n_2\epsilon_0}}, \quad (2.22)$$

where  $\chi_{eff}^{(2)}$  is an effective second-order susceptibility (measured in  $V^{-1}$ ) that includes the spatial overlap between the interacting fields and  $n_{1,2}$  are the refractive indices at  $\omega_p$  and  $2\omega_p$  respectively. Note that these coupled equations can describe both (degenerate) PDC and SHG, with the initial condition governing the distinction.

#### 2.5.4.2 Nonlinear Schrödinger equation

When the waveguide is composed of a  $\chi^{(3)}$  Kerr nonlinear material, the slowly-varying field envelope evolves according to the so-called nonlinear Schrödinger equation (NLSE):

$$\frac{\partial A(z, \tau)}{\partial z} = \left[ -i\frac{\beta_2}{2}\frac{\partial^2}{\partial\tau^2} + i\gamma|A|^2 \right] A(z, \tau). \quad (2.23)$$

Here  $A(z, \tau)$ ,  $\beta_2$ ,  $z$  and  $\tau$  are defined in the same way as Eqs. (2.21). On the right hand side, the final term (containing  $|A|^2$ ) describes the combined effects of SPM, XPM and Kerr FWM. Again, the slowly-varying envelope is normalized such that  $|A|^2$  is the instantaneous power in Watts. Here,  $\gamma$  represents the nonlinear interaction coefficient and is defined as

$$\gamma = \frac{\omega n_2}{c A_{\text{eff}}}, \quad (2.24)$$

where  $A_{\text{eff}}$  is the effective area of the confined mode in the waveguide, defined as

$$A_{\text{eff}} = \frac{\left[ \iint_{-\infty}^{\infty} |F(x, y)|^2 dx dy \right]^2}{\iint_{-\infty}^{\infty} |F(x, y)|^4 dx dy}, \quad (2.25)$$

with  $F(x, y)$  being the transverse mode profile from Eq. (2.11). The simplest solution to Eq. (2.23) is a plane wave of the form  $A = \sqrt{P_0} \exp(i\gamma P_0 z)$ . From this, it is easy to see that the wave does indeed accumulate a nonlinear, intensity-dependent phase shift as it propagates. Similar to the dispersion length [see Eq. (2.16)], we can also define a parameter for the *nonlinear length*

$$L_{NL} = \frac{1}{\gamma P_0}, \quad (2.26)$$

which corresponds to the length over which the accumulated nonlinear phase shift  $\phi_{NL} = 1$ .

In this work, we will be focussing heavily on one class of solutions to the NLSE which describes a solitary localised structure known as the soliton [19]. This solution describes a field envelope in the shape of a pulse which is capable of propagation without distortion in a Kerr nonlinear optical waveguide [20]. A careful balancing between dispersion and the nonlinear Kerr effect allows the pulse to maintain its shape for an indefinite propagation distance. The soliton corresponds to an exact analytical solution of the NLSE and can be written as [16]

$$A_{\text{sol}}(z, \tau) = \sqrt{P_s} \text{sech} \left( \frac{\tau}{\tau_s} \right) e^{(i\frac{\gamma P_s z}{2})}, \quad (2.27)$$

where  $P_s$  and  $\tau_s$  are the soliton peak power and temporal width, respectively, and are related through the condition  $1 = \gamma P_s \tau_s^2 / |\beta_2|$ .

One important characteristic of the NLSE soliton is the universality of the solutions across physical systems. Such structures have been observed in many varied systems from plasma physics [15] to cold atoms [17]. In a conservative system, the soliton will propagate without losing energy to the medium. However,

in dissipative systems, such as the ones we will be considering, energy lost to the medium must be replenished by an underlying driving field [44]. Details about solitons in dissipative systems will be covered in the following Chapter.

## 2.6 Optical resonators

A resonator is a system that allows a physical property, such as displacement or amplitude, to oscillate at a *resonant* frequency. If energy is put into the system at the resonant frequency it will increase the magnitude of the oscillating physical property beyond that of the driving force (as long as the energy dissipation is less than the injected driving energy). For this reason a resonator is said to be able to store resonant energy. In optics, this is achieved by creating a cavity to confine light. An optical cavity can be a system of mirrors or waveguides which directs a ray of light back to its origin in the cavity. Such cavities are capable of storing large amounts of optical power in the intracavity field. As this Thesis pertains to resonators exhibiting different dominant nonlinear effects, this Section will only cover the linear properties of optical resonators, with the relevant nonlinear behaviours being discussed in future Chapters.

### 2.6.1 Linear resonator properties

In our work, we consider ring-type resonators such as the one shown in Fig. 2.5 where coherent driving field is injected into the cavity by a coupler. This representation is valid for many resonator platforms from fiber rings to microresonators [45, 46]. The light trapped inside the cavity will interfere with the driving field each round trip of the cavity. This means that the maximum amplitude of the field will occur when the phase of the light is an integer multiple of  $2\pi$  after one round trip, causing the light to constructively interfere with the coherent driving field. The frequencies of light which accumulate an integer multiple of  $2\pi$  phase shift in one round trip are known as the resonant frequencies. These frequencies describe the longitudinal resonator modes which we will primarily use throughout this work as we normally only consider single transverse mode operation.

During propagation in the cavity, the slowly varying envelope will evolve according to cavity environment ( $A^m(0, \tau) \rightarrow A^m(L, \tau)$ ) before returning to the input coupler where it is superimposed with the coherent driving field. The evolution of the slowly-varying field envelope  $A(z, \tau)$  over consecutive round trips  $m$

in a cavity of length  $L$  can be described mathematically by the following infinite-dimensional map [20]:

$$A^{(m+1)}(0, \tau) = \sqrt{\rho}A^{(m)}(L, \tau)e^{i\phi_0} + \sqrt{\theta}A_{in}. \quad (2.28)$$

This equation relates the intracavity field at the start of the  $(m + 1)^{th}$  round trip  $A^{(m+1)}(0, \tau)$  to the intracavity field at the end of the previous round trip  $A^{(m)}(L, \tau)$ . The coefficient  $\rho$  represents the portion of the intracavity field intensity that is transmitted from one round trip to the next and stays in the cavity. For simplicity,  $\rho$  accounts for all the losses accumulated by the field over one round trip (e.g. coupling losses, absorption, scattering). The transmission coefficient  $\theta$  represents the portion of the input field power  $|A_{in}|^2 = P_{in}$  that is transmitted into the cavity. The term  $\phi_0 = \beta_0 L$  is the accumulated linear phase shift over one round trip and must be explicitly included here at the boundary as the evolution  $A^{(m)}(0) \rightarrow A^{(m)}(L)$  is governed by an envelope equation (such as the NLSE) which ignores the linear phase shift.

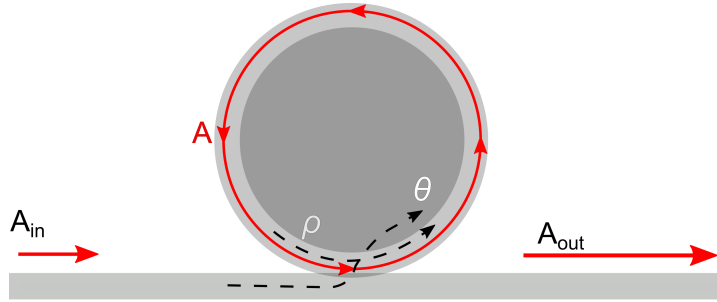


Figure 2.5: Simple schematic of an optical resonator with a single coupler acting as the transmitter/reflector.

### 2.6.2 Linear cavity response

Let us first consider the linear cavity behaviour under conditions of continuous wave (CW) driving such that  $A_{in}$  does not depend on time. Under conditions where no nonlinearity occurs, the slowly-varying envelope will remain CW and not evolve during one pass through the resonator. Thus, we have the simple case of  $A^{(m)}(L) = A^{(m)}(0)$ . The steady-state solutions of Eq. (2.28) can be obtained by setting  $A^{(m+1)}(0) = A^{(m)}(0)$  which produces

$$A^{(m)}(0) = \frac{\sqrt{\theta}A_{in}}{1 - \sqrt{\rho}e^{i\phi_0}}. \quad (2.29)$$

In terms of field powers  $P = |A^{(m)}|^2$  and  $P_{in} = |A_{in}|^2$ , we obtain the well-known Airy function of optical resonators

$$\frac{P}{P_{in}} = \frac{\theta/(1 - \sqrt{\rho})^2}{(1 + F \sin^2(\phi_0/2))}, \quad (2.30)$$

where  $F = 4\sqrt{\rho}/(1 - \sqrt{\rho})^2$ . The maximum intracavity power is achieved in the cavity when  $\phi_0 = 2k\pi$  where  $k$  is an integer. Consequently, the maximum power is then

$$P = P_{max} = \frac{P_{in}\theta}{(1 - \sqrt{\rho})^2}. \quad (2.31)$$

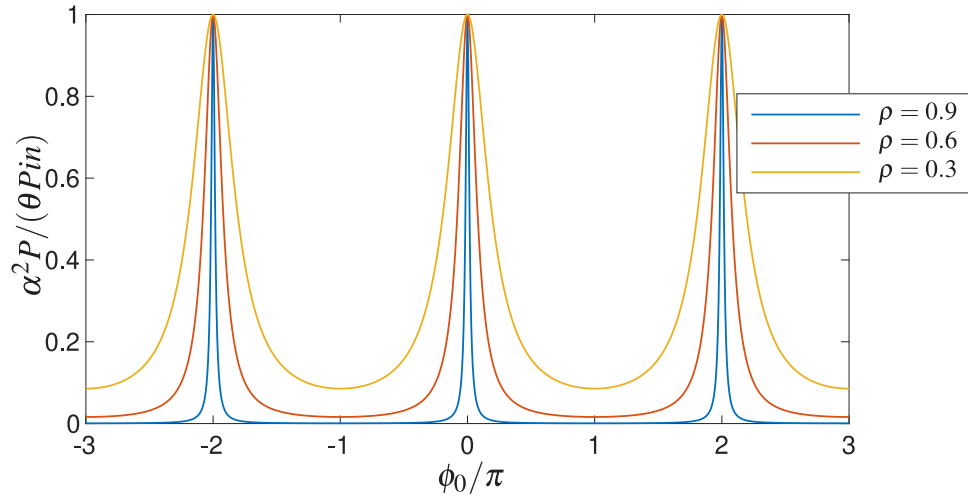


Figure 2.6: Plot of the linear intracavity energy profile with respect to the linear phase shift  $\phi$  for different values of  $\rho$ .  $\alpha \approx 1 - \sqrt{\rho}$  for cavities with high finesse.

Figure 2.6 shows an example of a linear resonator frequency response described by the Airy function (Eq. (2.30)). As can be seen, for phase shifts  $\phi_0$  that correspond to integer multiples of  $2\pi$ , the intracavity field attains a maximum; this corresponds to the phenomenon of resonance. Recalling that  $\phi_0 = \beta_0 L = \omega_0 n_{eff} L / c$ , we see that, to first order (neglecting group velocity dispersion), the resonances occur at frequencies  $f_k = kc / n_{eff} L$  with  $k$  being an integer [45].

These resonant frequencies are equally spaced and the separation between resonances is known as the *free spectral range* (FSR) [45] and is given by

$$\text{FSR} = f_{k+1} - f_k = c / (n_{eff} L). \quad (2.32)$$

We must emphasize that Eq. (2.32) is strictly valid only when dispersion is not present. In particular, non-zero group-velocity dispersion  $\beta_2$  renders the resonant frequencies non-equidistant. For all cases, the free-spectral range corresponds to the reciprocal of the time it takes for a wave packet to complete one round trip  $t_R$ , i.e.,  $FSR = 1/t_R$  where  $t_R = L/v_g = L/\beta_1$ . From this, it should be evident that non-zero  $\beta_2$  causes the FSR to change with frequency (since  $\beta_1$  changes with frequency).

As noted above, resonators allow for the storage of optical energy. Referring to Eq. (2.31), we see that the maximum power inside the resonator is inversely proportional to the resonator losses: a low-loss resonator (with  $\rho$  close to unity) can enable large powers to build up. This power storage makes resonators very interesting for nonlinear optical applications, as it becomes possible to obtain a strong intracavity nonlinear response even with comparatively low injected power levels [47].

As shown in Fig. 2.6 the loss can have great effect on the width of the resonances. It is customary, therefore, to characterize losses in optical resonators by referring to the ratio between the spacing (FSR) and width of a cavity resonance ( $\Delta f$ ). This ratio is known as the cavity *finesse*  $\mathcal{F}$  [45, 48], and it is defined by:

$$\mathcal{F} = \frac{\text{FSR}}{\Delta f}. \quad (2.33)$$

It can be shown that, for low-loss cavities (with large finesse and  $\rho$  close to unity), the finesse can be approximated as

$$\mathcal{F} \approx \frac{2\pi}{1 - \rho}. \quad (2.34)$$

Typical finesse values can range from the tens or hundreds in a macroscopic bow tie resonator [36] or fiber ring resonator [33], to the tens and even hundreds of thousands in monolithic microresonators [49, 50].

In addition to finesse, other metrics (related to the finesse) also exist that are often used to characterize resonator losses. One is the quality factor  $Q$  which is ubiquitous throughout all resonator fields. This factor is used when comparing the energy stored to the energy lost per cycle in a resonant system and is related to the finesse in optical resonators by [51]

$$Q = \frac{\mathcal{F}2\pi\omega}{\text{FSR}}. \quad (2.35)$$

The cavity photon lifetime  $t_{ph}$ , which describes the rate at which the intracavity field decays without pumping can also be related to the finesse by

$$t_{ph} = \frac{\mathcal{F}t_R}{2\pi}, \quad (2.36)$$

where  $t_R = 1/\text{FSR}$  is the cavity round trip time [51].



## Chapter 3

# Kerr cavity dynamics

This thesis deals both with resonators dominated by the  $\chi^{(2)}$  nonlinearity and the  $\chi^{(3)}$  Kerr nonlinearity. We will first describe the pertinent dynamics of Kerr nonlinear cavities as they are more established in the literature [52–58]. To this end, the purpose of this Chapter is to describe how the Kerr nonlinearity changes the properties of the linear resonators described in Chapter 2. This includes a description of the model which governs these dynamics and is used in all numerical simulations for Kerr nonlinear resonators in this Thesis. The phenomena of intracavity modulation instability and cavity solitons will also be explained along with the numerical methods used to simulate their dynamics as they feature heavily in this Work. We will conclude the Chapter by beginning the discussion of how temporal cavity solitons react in the presence of modulated driving fields, which will be carried over to the following Chapters.

### 3.1 Impact of Kerr nonlinearity on cavity resonances

The phase shift term  $\phi_0$  from Eq. (2.28) only accounts for the linear phase shift over one round trip. In a Kerr nonlinear optical resonator however, we must also account for the intensity dependent phase shift due to the Kerr effect. For a simple CW driving field, the intracavity field at the end of one round trip is described as

$$A^{(m)}(L) = A^{(m)}(0)e^{i\gamma PL}, \quad (3.1)$$

where  $\gamma$  is the nonlinear coefficient described in Subsection 2.5.4 and  $P = |A^{(m)}(0)|^2$  is the power of the intracavity field. This allows us to re-write Eq. (2.30) to include the Kerr effect as

$$\frac{P}{P_{in}} = \frac{\theta/(1 - \sqrt{\rho})^2}{1 + F \sin^2[(\phi_0 + \gamma PL)/2]}. \quad (3.2)$$

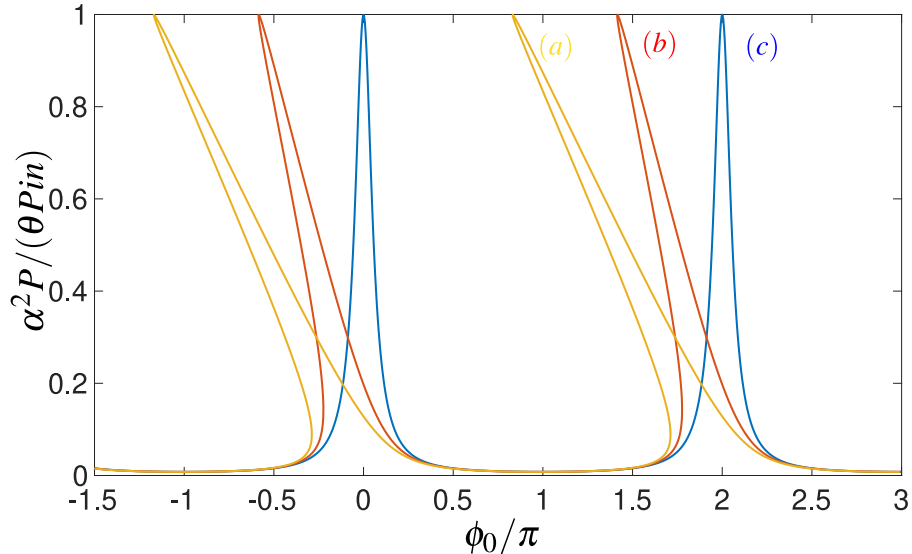


Figure 3.1: Plot of nonlinear cavity resonances for differing nonlinear strengths: (a)  $\gamma L = 0.3$ , (b)  $\gamma L = 0.15$  and (c)  $\gamma L = 0$ . In all cases,  $\rho = 0.7$ .

When  $P = P_{max} = P_{in}\theta/(1-\rho)^2$ , corresponding to the peaks of the resonance, the nonlinear phase shift  $\phi_{NL}$  is maximised and the total phase shift  $\phi = \phi_0 + \phi_{NL} = 2k\pi$  where  $k$  is an integer. At other points on the resonance the shift is much less and becomes negligible at the wings. The result is a tilted resonance as shown in Fig. 3.1 with the maximum nonlinear phase shift being  $\gamma P_{max}L$ . This tilt can become large, causing the resonance peak to shift a distance greater than the resonance width ( $\phi_{NL} > 2\pi/\mathcal{F}$ ) as demonstrated by Figs. 3.1(a,b). In this regime the cavity response becomes multi-valued, exhibiting a feature known as optical bistability (two stable states linked by an unstable state) that is typical of Kerr nonlinear cavities [59–61].

### 3.2 Lugiato-Lefever equation

So far, our analysis of resonator steady states concerns CW fields. Of course, in general the intracavity field may not be CW, and it becomes necessary to include the effects of group-velocity dispersion in the analysis. In this case, and considering a Kerr nonlinear resonator, the evolution of the field envelope over one single round trip ( $A^{(m)}(0, \tau) \rightarrow A^{(m)}(L, \tau)$ ) is described by the NLSE, Eq. (2.23). The boundary condition Eq. (2.28) and the NLSE then form an infinite-dimensional

map that together allow the modelling of the change in the intracavity field envelope from roundtrip to roundtrip in Kerr nonlinear optical resonators. However, when very little happens to the field envelope from one round trip to the next it is computationally much quicker to consider a *mean-field* description. This replaces the cavity map with a single nonlinear partial differential equation with driving. In order to apply this description, we must assume that we have high finesse and long nonlinear and dispersive lengths ( $L_{NL}$  and  $L_D \gg L$ ) allowing us to average all cavity effects over a single round trip [56]. Therefore, the electric field envelope will evolve smoothly over long time scales and we may replace the cavity round trip index  $m$  from our map with a *slow time* variable  $t = t_R m$  (representing long time scales over which the envelope evolves) with  $t_R$  being the round trip time. In doing this, we arrive at the well documented Lugiato-Lefever equation (LLE)[55, 62]:

$$t_R \frac{\partial A}{\partial t} = \left[ -\alpha + i(\gamma L |A|^2 - \delta_0) - i \frac{\beta_2}{2} L \frac{\partial^2}{\partial \tau^2} \right] A + \sqrt{\theta} A_{in}. \quad (3.3)$$

Now  $A \equiv A(t, \tau)$ , with  $z$  being removed by the introduction of the slow time variable  $t$ , while  $\tau$  represents the *fast time* frame which is moving at the group velocity of the intracavity field. Physically, the slow time describes changes in the field envelope over consecutive round trips, whilst the fast time describes the field's profile over a single round trip. The term  $\delta_0$  corresponds to a phase *detuning* of the driving field from a closest cavity resonance, and is linked to the round trip phase shift as  $\delta_0 = 2k\pi - \phi_0$ , where  $k$  is the order of the cavity resonance closest to the driving field frequency. The loss term  $\alpha$  represents half of the total loss per round trip and is related to the coefficient  $\rho$  from Eq. (2.28) by

$$\alpha \approx (1 - \rho)/2. \quad (3.4)$$

This LLE can be used to efficiently perform dynamic numerical simulations of Kerr nonlinear cavities over long time-scales compared to the cavity round trip time. Also of note is the exclusion of dispersion of orders larger than two. While higher-order dispersion terms may be relevant under certain conditions [63, 64], throughout this Thesis we always assume anomalous dispersion far from the ZDW such that higher-order dispersion has a negligible effect. For the purpose of this Thesis, it is advantageous to simplify the LLE by casting it to dimensionless form.

This is achieved through the following variable changes [20, 46]:

$$\begin{aligned} t &\Rightarrow \alpha \frac{t}{t_R}, & \tau &\Rightarrow \tau \sqrt{\frac{2\alpha}{|\beta_2|L}}, & A &\Rightarrow A \sqrt{\frac{\gamma L}{\alpha}}, \\ \Delta &= \frac{\delta_0}{\alpha}, & S &= A_{in} \sqrt{\frac{\gamma L \theta}{\alpha^3}}. \end{aligned}$$

Again assuming anomalous dispersion, this produces a dimensionless LLE of the form

$$\frac{\partial A(t, \tau)}{\partial t} = \left[ -1 + i(|A|^2 - \Delta) + i \frac{\partial^2}{\partial \tau^2} \right] A + S. \quad (3.5)$$

Using this form, we are able to model the full dynamics based on only two normalised parameters: the normalised pump strength  $S$  and the cavity detuning  $\Delta$ . The steady-state solutions ( $\partial A(t, \tau)/\partial t = 0$ ) can be found by directly solving for the roots of the right hand side of Eq. (3.5). The CW solutions ( $\partial A/\partial \tau = 0$ ) are the simplest as the dispersion term of Eq. (3.5) can be neglected yielding

$$A = \frac{S}{1 - i(|A|^2 - \Delta)}. \quad (3.6)$$

In this case, the normalised intracavity power  $Y = |A|^2$  of these solutions describes the nonlinear resonances which satisfy the cubic polynomial

$$X = Y^3 - 2\Delta Y^2 + (\Delta^2 + 1)Y, \quad (3.7)$$

where  $X = |S|^2$  represents the normalised pump power [20, 46]. Plotting the normalised intracavity power as a function of detuning demonstrates the nonlinear tilt mentioned previously as shown in Fig. 3.1. As this method only considers a single period of the Airy function Eq. (2.30), adjacent resonances cannot be accounted for concurrently. For this reason, the LLE loses validity if the nonlinear tilt is such that neighbouring resonances overlap [65].

### 3.3 Numerical methods

The LLE admits analytical solutions only in specific cases so we must, therefore, introduce numerical methods that we use to investigate the dynamics of Kerr nonlinear cavities. Here we describe two different methods for solving the Eq. (3.5) that are used throughout this Thesis.

### 3.3.1 Split-step Fourier method

In order to observe the evolution of the intracavity field as governed by the LLE, we will be numerically integrating Eq. (3.5) using the split-step Fourier method. In this scheme, the dispersion and nonlinear steps are assumed to act separately over small steps. This is done by dividing the total slow time interval of interest into small sections (steps) of length  $h$ . During each step, we assume the dispersive and nonlinear effects to act independently. Using Eq. (3.5) to demonstrate, we group the dispersive  $\hat{D}$  and nonlinear  $\hat{N}$  terms:

$$\frac{\partial A(t, \tau)}{\partial t} = (\hat{D} + \hat{N})A(t, \tau) + S \quad (3.8)$$

where

$$\hat{D} = i \frac{\partial^2}{\partial \tau^2}, \quad (3.9a)$$

$$\hat{N} = -1 + i(|A(0, \tau)|^2 - \Delta). \quad (3.9b)$$

Over the first step of  $h$  we ignore the dispersive term and integrate Eq. (3.8) in the time domain. Equation (3.8) is driven and is therefore an inhomogeneous differential equation known to give the following analytical solution:

$$A_{NL}(h, \tau) = \left( A(0, \tau) + \frac{S}{\hat{N}} \right) \exp(\hat{N}h) A(0, \tau) - \frac{S}{\hat{N}}. \quad (3.10)$$

Then we use the output of Eq. (3.10) as the initial condition for the dispersive second step. This is easily done in the frequency domain:

$$\frac{\partial \tilde{A}}{\partial t} = \hat{D} \tilde{A}(t, \Omega), \quad (3.11)$$

where  $\tilde{A}(t, \Omega)$  is the Fourier transform of the electric field  $\mathcal{F}[A(t, \tau)]$  and  $\hat{D} = -i\Omega^2$  ( $\mathcal{F}$  denotes the Fourier transform). When the simulation time window ( $\tau_{max} - \tau_{min}$ ) is chosen as the round trip time, the Fourier frequency grid is spaced by one FSR. Therefore, each point in the spectrum is spaced by one FSR. Combining the steps produces the following:

$$A(h, \tau) = \mathcal{F}^{-1} \left[ \exp(\hat{D}h) \cdot \mathcal{F}[A_{NL}(h, \tau)] \right]. \quad (3.12)$$

With one step complete, we can then use the final field as the initial condition for the following step. This process is repeated  $n$  times until a desired simulation time of  $t = nh$  has been achieved. This stepping method has been used to perform all of the dynamic numerical simulations that we reference in this Thesis.

### 3.3.2 Newton-Raphson method

The split-step Fourier method is instrumental in our investigations of non-stationary and dynamically evolving fields, but when studying stationary localised structures at steady-state, it becomes useful to be able to solve for the roots of the LLE. This is done by setting the left hand side of Eq. (3.5) to zero and finding the corresponding solutions  $A(t, \tau)$ . The Newton-Raphson method is a handy root-finding method that we employ to find steady state solutions. Unlike the split step method, it cannot elucidate evolution dynamics, but it does provide stability information about the solutions found. To illustrate the idea behind the Newton-Raphson method, we may consider a simple one-variable function  $f(x)$ . To find the roots of the function using the Newton-Raphson method, we first give an initial guess for the position of the root,  $x = x_0$ . According to this method, a better estimate can be obtained by finding and extending the tangent to  $f(x_0)$  in order to find where it crosses zero,  $x_1$ . Mathematically this is represented as

$$f(x_1) \approx f(x_0) + f'(x_0)(x_1 - x_0) = 0. \quad (3.13)$$

With this new estimation of the position of the root,  $x_1$ , we repeat the above expression using  $x_1$  as our initial guess. This iteration can be repeated until  $|\delta x| < \sigma$ , where  $\sigma$  is the required accuracy and  $\delta x = x_{k+1} - x_k$  where  $k$  is an integer.

We can now extend this technique to multidimensional problems such as the dimensionless LLE (Eq. (3.5)). The fast time  $\tau$  can be discretized into a vector with  $N$  elements and the partial derivatives  $\partial^2/\partial\tau^2$  transform the LLE into  $2N$  real, coupled, ordinary differential equations. This system of equations can be written as

$$\partial\mathbf{A}/\partial t = \mathbf{G}(\mathbf{A}), \quad (3.14)$$

where  $\mathbf{A}$  is a discretized vector of  $2N$  elements containing the real and imaginary components of the field envelope and  $\mathbf{G}$  is a vector-valued function representing the right-hand-side of the LLE. The steady state solutions of Eq. (3.14) satisfy  $\mathbf{G}(\mathbf{A}) = 0$ . Remembering Eq. (3.13), we choose an initial guess of  $\mathbf{A}_0$  and linearize to obtain

$$\mathbf{G}(\mathbf{A}_0 + \delta\mathbf{A}) \approx \mathbf{G}(\mathbf{A}_0) + J \cdot \delta\mathbf{A} = 0, \quad (3.15)$$

where  $J$  is the discretised Jacobian matrix of the system at  $\mathbf{A}_0$ . Equation (3.15) yields  $\delta\mathbf{A} = -J^{-1}\mathbf{G}(\mathbf{A}_0)$ , which allows us to obtain an improved estimate for the root of Eq. (3.14) as:  $\mathbf{A}_1 = \mathbf{A}_0 + \delta\mathbf{A} = \mathbf{A}_0 - J^{-1}\mathbf{G}(\mathbf{A}_0)$ . This process is iterated until  $\mathbf{G}(\mathbf{A}_n) \approx 0$  at some specified accuracy.

As stated previously, this method offers little dynamical information, though it enables us to determine the stability of the solutions we find by analysing the eigenvalues of the resulting Jacobian matrix. By solving Eq. (3.5) using this method, we are able to find steady-state solutions, stable and unstable, over wide ranges of parameters in order to trace out bifurcation curves and branches in parameter space. All results found using this method in this Thesis were obtained using a proprietary code produced by my co-supervisor Stéphane Coen.

### 3.4 Intracavity modulation instability

We will now use numerical simulations to briefly discuss two key dynamical phenomena associated with Kerr resonators. As discussed above, Kerr resonators are capable of bistability between two stable CW states. However, in the anomalous dispersion regime, the upper state is only stable to CW perturbations and will undergo a pattern forming (Turing) instability in response to periodic perturbations [56, 66]. This instability is often referred to as modulation instability (MI) and is the time-domain manifestation of degenerate Kerr FWM that occurs via phase matched SPM and XPM. In the frequency-domain, MI causes the growth of Stokes and anti-Stokes sidebands about the pump where  $\omega_{s,a} = \omega_0 \pm \Omega$ . The growth of these sidebands corresponds to the growth of a modulation of the upper state in the time domain.

In a Kerr nonlinear resonator operating in the anomalous dispersion regime, maximum MI gain is experienced when the modulation frequency  $\Omega_{\max}$  [56] satisfies

$$2Y - \Omega_{\max}^2 - \Delta = 0. \quad (3.16)$$

By performing a linear stability analysis, it can be shown that the upper CW state can exhibit MI when the normalised intracavity power  $Y = |A|^2 > 1$  and  $Y > \Delta/2$ . The MI detuning threshold is  $\Delta_{MI} = 1 - \sqrt{X - 1}$  making  $X = 1$  the minimum necessary driving power for MI [56].

To illustrate the dynamics of intracavity MI, we have chosen a fixed driving power of  $X = 10$  which is sufficient to ensure MI of the upper CW branch. Figure 3.2 shows steady-state intracavity peak powers for a single resonance. It is shown that above  $\Delta_{MI} \approx -2$ , a branch of stable patterned states emerges. At this point, the growing sidebands are spaced by  $\Omega_{MI}$  while the field in the time domain corresponds to a stable pattern representing a train of pulses. Figure 3.3 shows a numerical simulation of the system described above as the detuning is scanned

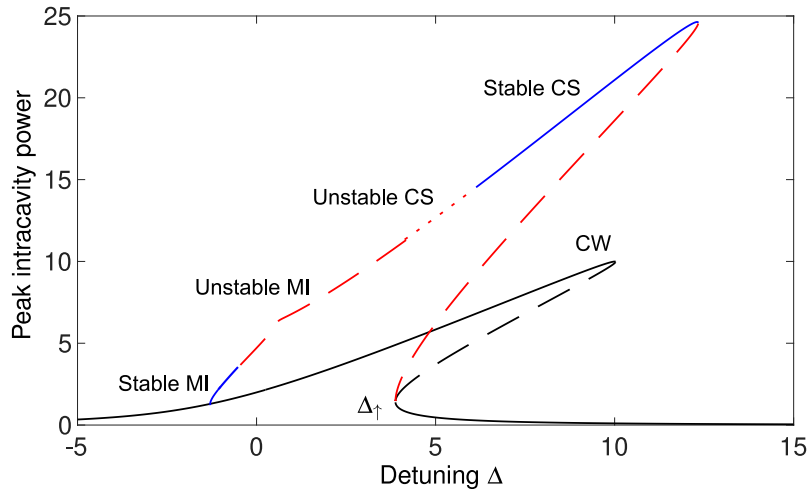


Figure 3.2: Plot of the intracavity peak power vs  $\Delta$  showing MI and CS branches over the CW nonlinear cavity resonances. Note that unstable MI corresponds to patterns that arise via MI and that are unstable, exhibiting fluctuations along the slow and fast times.

over the resonance, a common practise in experimental applications. In the region of  $\Delta = 0$  in Fig. 3.3(a) it can be seen that a stable time domain pattern has formed and coincides with the equally spaced spectral peaks in Fig. 3.3(b). As the detuning becomes large, the stable MI pattern transitions into an unstable field where the amplitudes of the frequency components evolve chaotically. This can be observed in Fig. 3.3 between  $\Delta \approx 0$  and  $\Delta_{\uparrow} \approx 4$ . As the detuning increases beyond  $\Delta_{\uparrow}$ , the intracavity field transitions into a regime characterised by unstable CSs and breather CSs sitting atop the lower CW branch. Moving further, after  $\Delta \approx 6$  the system collapses to a regime where stable CSs are supported by the lower CW field before the detuning passes out of resonance with the cavity at  $\Delta_{\max}$

### 3.5 Temporal Kerr cavity solitons

We know that degenerate FWM is responsible for MI in Kerr resonators. We also know that the upper branch MI can coexist with the stable lower CW state. One can imagine that it is possible to localise this coexistence in time such that the intracavity field corresponds to a pattern in one location with the lower CW field existing elsewhere. When this localised structure forms a single oscillation of the MI pattern, we are left with a pulse of light in the cavity which is surrounded

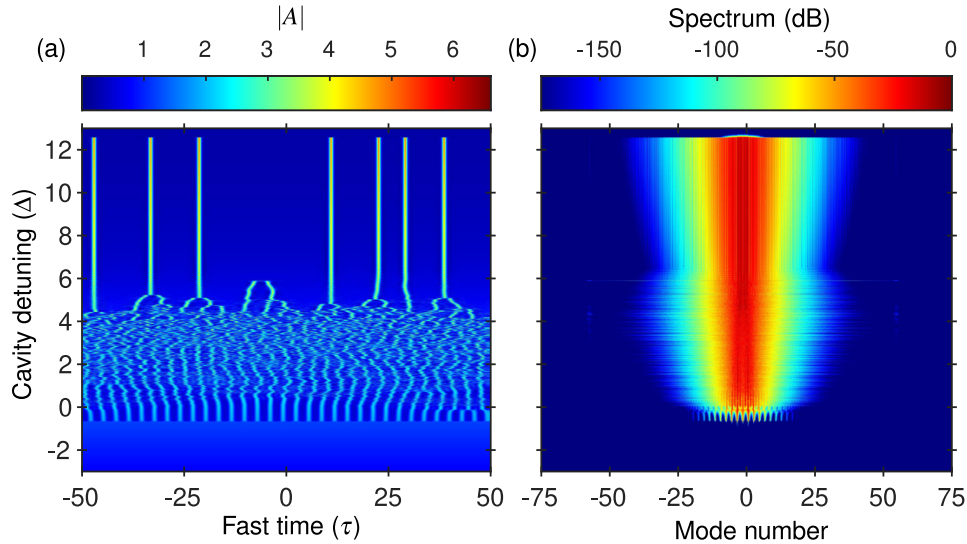


Figure 3.3: LLE simulated evolution of (a) the intracavity electric field profile and (b) the intracavity spectral profile as the normalised detuning parameter  $\Delta$  is scanned over the resonance.

by a homogeneous field, corresponding to a structure known as a temporal cavity soliton.

Temporal CSs were first proposed theoretically in 1993 [22] and only observed experimentally in 2010 [23]. However, they are rooted into a much longer history. This is because, by virtue of the analogy between spatial diffraction and temporal dispersion, temporal CSs are closely related to spatial CSs — persisting spots of light — that have been extensively studied in the context of diffractive resonators [67]. Physically, temporal CSs arise from a double balance [44]: their dispersive spreading is arrested by the Kerr nonlinearity while the losses they accumulate are compensated for by the parametric (MI) gain from the CW background field. This double balance renders CSs unique attractors: for given parameters  $(S, \Delta)$ , only one type of a CS can exist. This is in stark contrast with conservative solitons of the NLSE, which form a continuous family with different durations and peak powers (confined by the soliton condition) [68].

As stated above, CSs exist for cavity detunings where an MI patterned state coexists with the stable lower branch CW state. Figure 3.2 shows the range of  $\Delta$  for which CSs exist for a driving power  $X = 10$ . As can be seen, CSs exist from the onset of bistability ( $\Delta_{\uparrow} \approx 3(X/4)^{1/3}$  for  $X \gg 1$ ) to the detuning upper limit

for CS existence of  $\Delta_{\max} = \pi^2 X/8$  [24, 69]. It is easy here, and in Fig. 3.3, to see the relation between intracavity MI and CSs. As the detuning increases past  $\Delta_{\uparrow}$  the intracavity field transitions from an unstable MI pattern to an train of unstable CSs. after this transition, the CSs in the cavity become stable, attaining their characteristic shape.

Although they correspond to steady-state solutions of the LLE, there is no exact analytical expression that can describe a CS. However, an approximate solution exists (valid for large detuning), and reads:

$$A_{sol}(0, \tau) \approx \sqrt{2\Delta} sech[\sqrt{\Delta}(\tau - \tau_{CS})] e^{-i\phi_S} + A_{\downarrow}, \quad (3.17)$$

where  $\tau_{CS}$  is the fast time location of the CS,  $\phi_S$  corresponds to the detuning-dependent phase of the CS relative to the driving field, and  $A_{\downarrow}$  is the stable lower branch CW solution which supports the CS. As can be seen, this form corresponds to a particular NLSE soliton (with peak power  $2\Delta$  and duration  $1/\sqrt{\Delta}$ ) that sits atop the CW background which corresponds to the stable lower level CW steady-state solution of the LLE. A field in the form of Eq. (3.17) is a close approximation of a CS and will evolve into a CS under the correct set of parameters (i.e. parameters for which the CS state is a stable attractor).

While a given set of parameters can only sustain a single type of CS, several of them can coexist, independently circulating around the resonator. Because of this, CSs (both spatial and temporal) have been proposed as ideal candidates for bits in optical memories [23, 70]. Moreover, CSs exhibit a feature known as plasticity [33, 71–73], which allows the solitons to be manipulated and controlled, making them attractive for applications in all-optical information processing. The following Section will briefly describe this key phenomenon.

### 3.6 Cavity solitons in the presence of driving field inhomogeneities

Since CSs sit atop a homogeneous background, they exhibit full translation symmetry. This means that there is no opposing force to restore a CS which is perturbed from its position (e.g. along the fast time  $\tau$ ). Therefore, a CS will move under the influence of inhomogeneities in the driving field or environment and will remain displaced.

Inadvertent inhomogeneities can arise due to material defects or imperfections in the CW driving field. This is particularly problematic for *spatial* CSs in *diffractive* resonators as inhomogeneities in the 2-D transverse plane of the resonator

cause adjacent CSs to experience different local environments [74, 75]. Due to the one dimensional nature of *temporal* CS localization, each CS experiences the same average environment [35]; yet, inhomogeneities of the driving field in time can lead to unwanted motion [72]. For example, excitation of acoustic waves by one soliton has been shown to give rise to long range interactions between adjacent temporal CSs[76], thus affecting their use as bit elements in all-optical buffers[23].

Importantly, CS plasticity can also be leveraged to advantageously manipulate and control soliton configurations. This can be achieved by intentionally imposing desired inhomogeneities on the cavity driving field. In particular, imposing phase modulations on the cavity driving field has been demonstrated as an effective means to control the CSs, allowing the them to be trapped at given positions (or bit slots) [33, 73]. In what follows we illustrate such dynamics by means of numerical simulations and demonstrate how the velocity of a CS in the presence of inhomogeneities can be calculated.

### 3.6.1 Illustrative numerical simulations of phase modulation trapping

To illustrate plasticity, and more specifically trapping of CSs by phase modulations, we consider a stationary CS sitting atop a CW field. This CS is phase-locked to this driving field and will travel around the cavity at a constant group velocity. We then subject the driving field to a phase inhomogeneity:

$$S(\tau) = S_0 e^{i\phi(\tau)}, \quad (3.18)$$

with  $\phi(\tau)$  in the form of a Gaussian pulse:

$$\phi(\tau) = \phi_0 \exp\left(\frac{\tau^2}{2\tau_G^2}\right), \quad (3.19)$$

where  $\tau_G$  is the width of the pulse and  $\phi_0$  is the amplitude. Figure 3.4 shows results from a dimensionless LLE simulation with a CS initialised at  $\tau = 10$ , on the edge of the phase inhomogeneity (for other parameters, see caption). Figure 3.4(c) clearly shows the CS has moved toward and then trapped at the local maximum in the phase profile at  $\tau = 0$ . At this *trapping position* the CS will again travel at the group velocity of the driving field.

We may physically understand the soliton motion in response to phase perturbations as follows: when the soliton sits at a position with a non-zero phase gradient, it experiences a shift in its instantaneous frequency of

$$\delta\Omega = -\frac{d\phi}{d\tau}\Big|_{\tau=\tau_{CS}} = -\phi'. \quad (3.20)$$

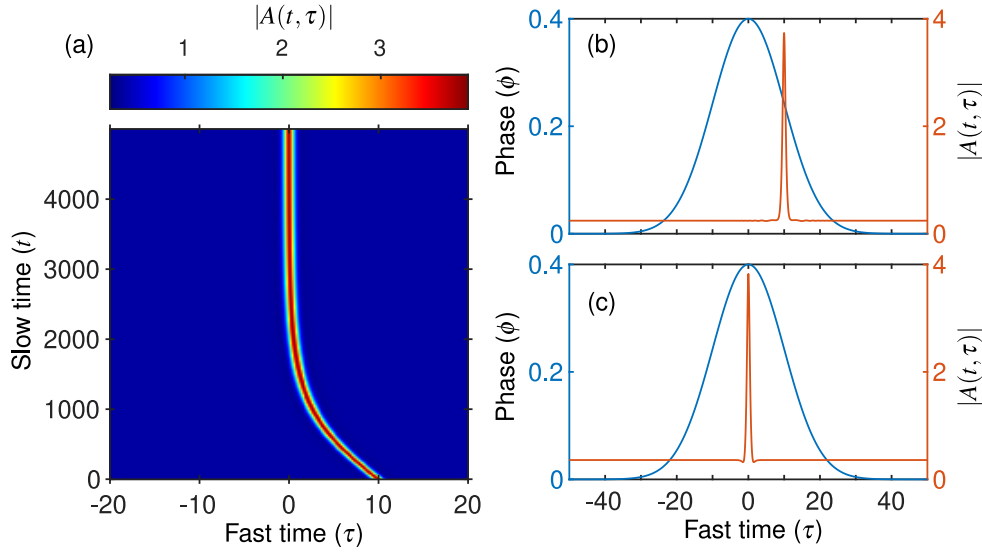


Figure 3.4: Numerical simulation of CS trapping at the peak of a Gaussian phase inhomogeneity described by Eq. (3.19) with amplitude  $\phi_0 = 0.4$  and width  $\tau_g = 10$ . The cavity detuning  $\Delta = 7$  and the CW driving field amplitude  $S_0 = 2.5$ . (a) shows the slow time evolution of the intracavity electric field amplitude. (b) shows the Gaussian phase profile  $\phi(\tau)$  which is imparted on the driving field, along with the initial intracavity field profile showing the CS's initial position at  $\tau = 10$  relative to the phase peak at  $\tau = 0$ . (c) shows the final position of the CS relative to the phase profile and it is clear that the CS has come to rest at the peak.

In dimensional units, a soliton whose frequency is shifted by  $\delta\Omega$  from a given reference frequency  $\omega_0$  propagating in a waveguide will experience a time-domain drift  $d\tau_{CS}/dz = \beta_2\delta\Omega$  due to group-velocity dispersion. Thus, the drift over a single round trip (with length  $L$ ) is given by  $\tau_{drift} = \beta_2 L \delta\Omega$ . We may thus write an equation of motion for the CS position over consecutive round trips as

$$t_R \frac{d\tau_{CS}}{dt} = \beta_2 L \delta\Omega. \quad (3.21)$$

In dimensionless units, we have  $t_R = 1$ ,  $\beta_2 = -2$  and  $L = 1$ . Remembering Eq. (3.20) the dimensionless drift is

$$V_{drift} = \frac{d\tau'_{CS}}{dt'} = 2\phi'. \quad (3.22)$$

Accordingly, a positive (negative) phase gradient will cause a decrease (increase) in the group velocity. At the maximum of the phase profile, the gradient becomes

zero and the CS experiences no drift velocity. Therefore, CSs in the presence of a phase inhomogeneity in the driving field will invariably be attracted to and trapped at the maximum.

Interestingly, if the phase modulation on the driving field is made to be slow-time dependent ( $\phi(t, \tau)$ ), we are able to dynamically shift the CS trapping position as shown in Fig. 3.4. As long as this change occurs slowly, the CS will remain trapped and will move with the phase peak. At steady state, the CS and phase peak will again travel at the original group velocity.

### 3.6.2 Theory of cavity soliton plasticity

The discussion above provided a simple physical description of CS plasticity in response to driving field phase inhomogeneities. The general case, where arbitrary perturbations can be present, is more complicated. A detailed theory has nevertheless been developed by Maggipinto et al. [72] (see also [77]). It has been shown that the response to fluctuations in the driving field is dominated by the neutral (or "Goldstone") mode, of the CS. This mode corresponds to the left eigenvector  $\mathbf{v}_0$  associated with the zero eigenvalue of the discretized Jacobian of the stationary solution,  $\mathbf{J}(\mathbf{A})$ , where  $\mathbf{A}$  is the discretized vector containing the real and imaginary components of the steady state field envelope found using the iterative Newton-Raphson method. With all other eigenvectors of a stable solution having eigenvalues with negative real parts, their effects quickly die out as  $t \rightarrow \infty$ .

Let us now consider a driving field that exhibits a small inhomogeneity  $P(\tau)$  along the fast time:  $S(\tau) = S_0 + P(\tau)$  where  $S_0 = S(\tau_{CS})$  is the local driving field amplitude at the position of the CS,  $\tau_{CS}$ . We can amend Eq. (3.14) to account for the perturbation such that

$$\frac{\partial \mathbf{E}}{\partial t} = \mathbf{G}(\mathbf{A}) + \mathbf{P}, \quad (3.23)$$

where  $\mathbf{P}$  is the discretized perturbation of  $2N$  components containing the real and imaginary parts of  $P(\tau)$ . According to the general theory behind CS plasticity [72], a CS will drift in response to the perturbation at a rate given by

$$V_{drift} = \frac{d\tau_{CS}}{dt} = \frac{\langle \mathbf{v}_0 | \mathbf{P} \rangle}{\langle \mathbf{v}_0 | \frac{d\mathbf{A}}{d\tau} \rangle}, \quad (3.24)$$

The inner product here corresponds to a dot product of the vectors with  $2N$  components. The denominator is a normalization factor and will be denoted as  $N$ . Thus far, we have used vector notation for ease of use with root finding algorithms such as the Newton-Raphson method. To facilitate further analyses, we now recast

the discretized vectors as continuous functions. Separating the real and imaginary components, we obtain

$$V_{drift} = \frac{\langle v_{0R}(\tau)|P_R(\tau)\rangle + \langle v_{0I}(\tau)|P_I(\tau)\rangle}{N}, \quad (3.25)$$

where  $v_{0R}$  and  $v_{0I}$  correspond to the real and imaginary parts of the left eigenvector and  $P_R$  and  $P_I$  correspond to the real and imaginary components of the perturbation, and the inner product now represents multiplication and integration over the fast time  $\tau$ . We then perform a Taylor series expansion of the real and imaginary parts of the perturbation at  $\tau_{CS}$  where  $P(\tau_{CS}) = 0$  giving

$$P_R(\tau) \approx 0 + (\tau - \tau_{CS}) \frac{dP_R(\tau_{CS})}{d\tau}, \quad (3.26a)$$

$$P_I(\tau) \approx 0 + (\tau - \tau_{CS}) \frac{dP_I(\tau_{CS})}{d\tau}, \quad (3.26b)$$

We can substitute Eqs. (3.26) into Eq. (3.25) to obtain

$$V_{drift} = \frac{\frac{dP_R(\tau_{CS})}{d\tau} \langle v_{0R}(\tau - \tau_{CS})|\tau - \tau_{CS}\rangle + \frac{dP_I(\tau_{CS})}{d\tau} \langle v_{0I}(\tau - \tau_{CS})|\tau - \tau_{CS}\rangle}{N}. \quad (3.27)$$

If we consider the effects of a phase profile  $\phi(\tau)$  imposed on an otherwise CW driving field, i.e.,  $S(\tau) = S_0 e^{i\phi(\tau)}$ . Assuming the phase perturbation amplitude is small, we may approximate  $S(\tau) \simeq S_0(1 + i\phi(\tau))$ . Accordingly, after a first order Taylor series expansion the perturbation can be written as

$$P(\tau) = iS_0\phi(\tau) \approx iS_0 \frac{d\phi(\tau_{CS})}{d\tau} (\tau - \tau_{CS}). \quad (3.28)$$

This perturbation is purely imaginary, leaving the expression for the drift velocity as

$$V_{drift} = \frac{\langle v_{0I}(\tau - \tau_{CS})|\tau - \tau_{CS}\rangle}{N} S_0 \frac{d\phi(\tau_{CS})}{d\tau}. \quad (3.29)$$

In Fig. 3.5 we have calculated the first term on the right hand side  $b = \langle v_{0I}(\tau - \tau_{CS})|\tau - \tau_{CS}\rangle/N$  for a range of driving strengths  $S_0$  and a fixed detuning  $\Delta = 7$ . These results were obtained by first finding the steady-state CS solution of Eq. (4.1) for a homogeneous driving field with strength  $S_0$  and detuning  $\Delta$ . We then determine the CS solution's neutral mode (technically, the even components of the left eigenvector with zero eigenvalue of the system's Jacobian) before evaluating the inner product [72]. We can see that  $b \approx 2/S_0$ , resulting in a final expression for the drift velocity:

$$V_{drift} \approx 2 \frac{d\phi(\tau_{CS})}{d\tau}, \quad (3.30)$$

in accordance with Eq. (3.22).

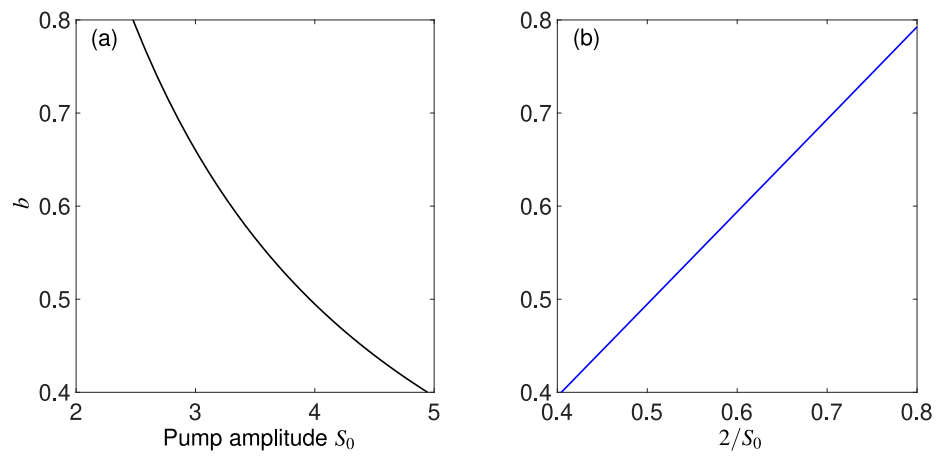


Figure 3.5: Plots showing coefficient  $b$  to establish  $2/S_0$  relationship arising from phase modulation of the driving field where (b) is the linearised version of (a).



## Chapter 4

# Intensity trapping of cavity solitons

As demonstrated in the previous Chapter, the dynamics of CS plasticity under the influence of phase inhomogeneities in a quasi-CW driving field are well understood and backed by experimental observations. However, any inhomogeneity can give rise to CS motion, not just in the phase. In contrast to the general understanding of CS motion due to phase gradients, there has been surprisingly little consideration for the details of CS motion in the presence of intensity gradients. Although numerous studies have investigated the behaviour of Kerr cavities in the presence of pulsed or amplitude-modulated driving fields [57, 78–80], the dynamics of CSs and their trapping in such configurations has not been extensively examined. Theory detailed by Maggipinto et al. [72] and introduced in the previous Chapter can, in principle, deal with amplitude inhomogeneities as well as phase modulations. This theory has been argued to predict dynamics in the presence of amplitude inhomogeneities which are similar to phase modulation, i.e., CSs moving along amplitude gradients towards maxima of the driving field. Surprisingly however, anecdotal evidence has surfaced over recent years that CSs may not always be attracted to extrema of the driving field [65, 81]. In particular, it has been shown in systems with amplitude modulated driving fields that CSs can come to rest away from the extrema of the driving field, in stark contrast to the phase trapping behaviours [65].

Before describing the dynamics of CSs in the presence of driving field amplitude inhomogeneities, we briefly discuss the motivation behind this work. Though CW driving is arguably the simplest method of sustaining CSs as of yet, it comes with certain disadvantages. Cavity solitons are localised states which draw energy only

from the portion of the intracavity field with which they overlap. Since the CSs are typically orders of magnitude shorter than the characteristic round trip time of the resonator, energy contained in the background field that is outside of the CS profile is effectively wasted. If the driving field is instead intensity modulated into a train of short pulses, energy can be more efficiently supplied to the soliton [34]. An added advantage of such pulsed pumping is the ability to achieve greater power levels than those possible in pure CW operation as a train of pulses can be amplified more efficiently.

As alluded to above, disadvantages of CW driving can be mitigated by pumping the resonator with a train of short pulses whose periodicity is synchronized with the cavity round trip time. Such “pulsed pumping” has been widely employed in both fibre ring resonator and microresonator experiments [57, 78–83] and it has been shown that CSs supported by a pulse have essentially the same functional form as those supported by a CW driving field [34]. The localised nature of the driving field, coupled with the plasticity of CSs, has an added benefit of ensuring that the repetition rate of the CS remains locked to that of the driving field. With growing interest in complex pulsed driving systems, it is important that we uncover more about the physics underlying CSs and their interactions with pulsed (or more generally amplitude modulated) driving fields. In this Chapter, we will explore, in detail, the dynamics of CSs in the presence of driving field amplitude inhomogeneities.

## 4.1 Numerical model

In order to study the dynamics of CSs in the presence of driving field amplitude inhomogeneities we rely on numerical simulations of our system. We consider a dispersive, Kerr-nonlinear ring-type resonator exhibiting anomalous dispersion that is being driven by a pulsed pump source. We will assume for this Chapter that the driving pulse is always synchronised to the cavity round trip time, and therefore the natural round trip time of the CS [we will discuss CS behaviour without this assumption in the next Chapter]. The evolution of the slowly varying field envelope  $A(t, \tau)$  can be modelled by the dimensionless LLE, Eq. (3.5), though with the inclusion of a fast time variant driving field  $S(\tau)$ :

$$\frac{\partial A(t, \tau)}{\partial t} = \left[ -1 + i(|A|^2 - \Delta) + i \frac{\partial^2}{\partial \tau^2} \right] A + S(\tau). \quad (4.1)$$

The lack of slow time dependence of the driving field means that the driving pulse is synchronised to the cavity round trip time. Importantly, we assume that the

driving pulse width is large when compared to the characteristic width of the CS. This is done in order to more accurately portray generic parameters achievable in Kerr resonator systems and to assure that the CS experiences a quasi-homogeneous background which is perturbed by an approximately constant gradient.

We begin by considering a situation where we drive our cavity with a train of Gaussian pulses which are synchronised to the cavity round trip time. This yields the following normalised driving field amplitude:

$$S(\tau) = S_0 \exp\left(-\frac{\tau^2}{2\tau_G^2}\right), \quad (4.2)$$

where the width of the driving pulse  $\tau_G = 20$  is chosen to be much broader than the width of the CS ( $\tau_{CS} < 1$ ). In order to study the dynamics of CS motion in the presence of this field, we use the split-step Fourier method to numerically integrate Eq. (4.1). We begin with an initial condition  $A(0, \tau) = \sqrt{2\Delta} \text{sech}[\sqrt{\Delta}(\tau - \tau_0)]$  which approximates a CS that is temporally offset from the driving pulse maximum by  $\tau_0$ . By allowing this split-step simulation to run until the field reaches steady-state, we will be able to draw our conclusions about the behaviours of CSs in such systems.

## 4.2 Illustrative simulations

To start our investigation into the motion of CSs in the presence of driving field amplitude inhomogeneities, we fix our normalised cavity detuning to  $\Delta = 4$  and run simulations for differing pulse amplitudes. In Fig. 4.1, we show the results of CSs which are excited off peak for two peak amplitudes. Figure 4.1(a,c) correspond to driving field amplitude of  $S_0 = 1.9$  while Fig. 4.1(b,d) correspond to  $S_0 = 2.3$ . In both instances, the CS is launched in the same position with respect to the peak ( $\tau_0 = 5$ ). For the first case, we can see that the CS drifts towards the peak and comes to rest at  $\tau = 0$ , at the maximum of the driving field. However, when we increase the amplitude we note that the CS actually moves away from the peak before coming to rest on the edge of the driving field. In this case, the field reaches steady state when the CS reaches a position,  $\tau_{CS} \approx 11$ , where the local value of the driving field  $S(\tau_{CS}) = 1.98$ .

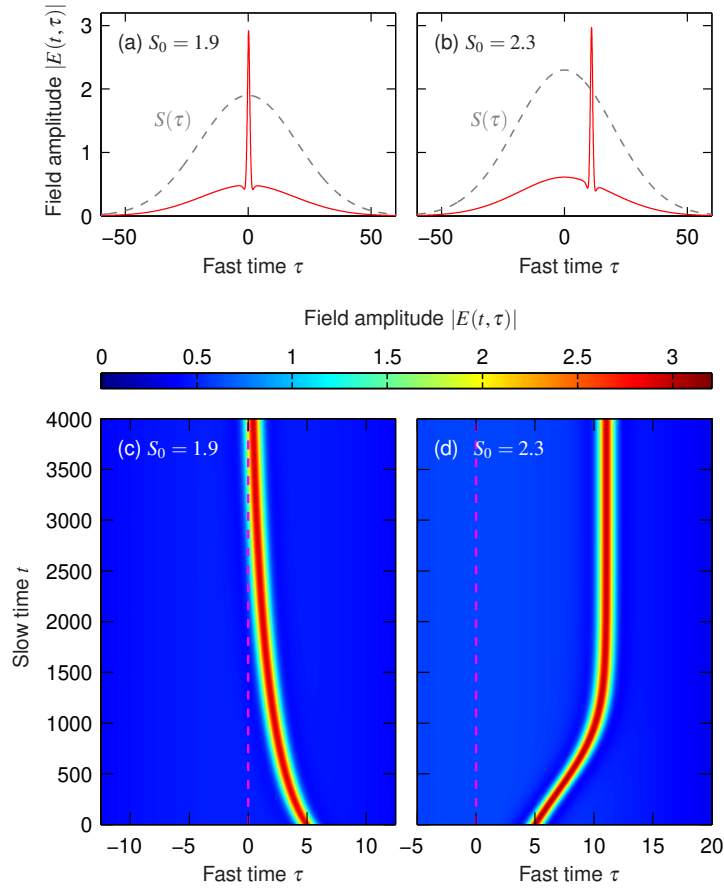


Figure 4.1: (a,b) Steady-state intracavity field solutions (red curves) for peak driving amplitudes (a)  $S_0 = 1.9$  and (b)  $S_0 = 2.3$ . Gray dashed curves show the corresponding Gaussian driving field amplitude profiles. (c,d) Dynamical intracavity field evolutions corresponding to (a) and (b), respectively. The initial soliton position  $\tau_0 = 5$ . Dashed vertical magenta line highlights the position of the maximum driving field amplitude ( $\tau = 0$ ). Note the different x-axes in (c) and (d).

The results above show that the CS can be attracted toward or away from the driving field maximum depending on the value of that maximum. This behaviour is surprising in that it comes in stark contrast to predictions and observations of CS dynamics in the presence of phase inhomogeneities, as well as theoretical calculations presented by Maggipinto et al. [72]. In order to gain more insights into this behaviour, we fix our cavity detuning and run simulations for a range of values of the peak driving field amplitude  $S_0$ . We allow each simulation to reach steady state before extracting the final position of the CS and the corresponding local field amplitude  $S(\tau_{CS})$ . In Fig. 4.2(a) we plot the driving field value  $S(\tau_{CS})$  at which

the CS comes to rest at steady-state for increasing peak amplitude values  $S_0$ . We initially observe a region where  $S(\tau_{CS}) = S_0$ , corresponding to the CS coming to rest at the peak of the driving field. However, when the peak of the driving pulse increases beyond a critical value  $S_c$  the CS will be attracted towards a position away from the peak such that the local value  $S(\tau_{CS}) = S_c$  regardless of the peak amplitude.

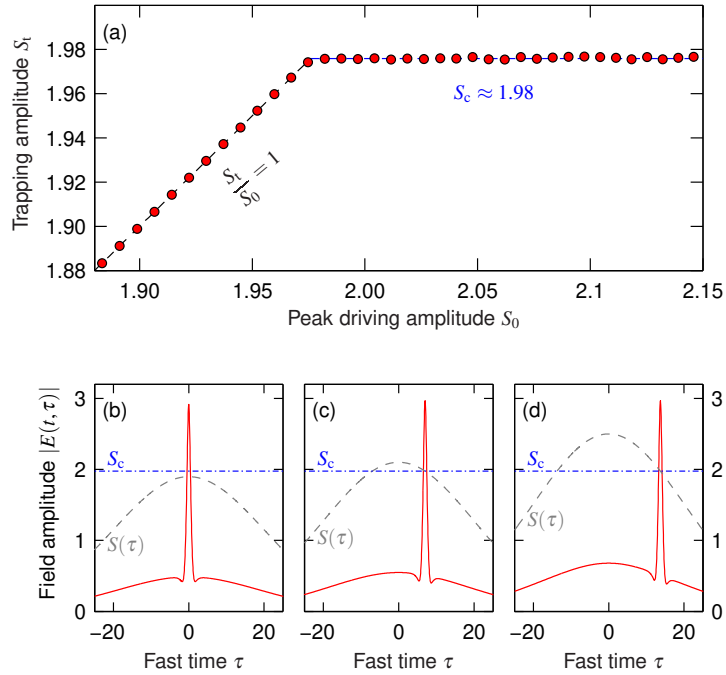


Figure 4.2: (a) Driving field amplitude at the steady-state CS trapping position [ $S_t = S(\tau_{CS})$ ] as a function of the peak driving amplitude  $S_0$ . For  $S_0 < S_c$ , the CS will trap at the peak, while for  $S_0 > S_c$  the CS will trap at a fast time value  $\tau_{CS}$  such that  $S(\tau_{CS}) = S_c$ . (b)–(d) Red curves show steady-state intracavity field profiles for three different driving amplitudes: (b)  $S_0 = 1.9$ , (c)  $S_0 = 2.1$ , and (d)  $S_0 = 2.5$ . Gray dashed curves show the corresponding Gaussian driving field profiles  $S(\tau)$ . Dash-dotted horizontal blue line indicates the critical driving value  $S_c = 1.98$ . A detuning  $\Delta = 4$  was used in all calculations and the driving field was assumed to be a Gaussian with duration  $\tau_G = 20$ .

The behaviour described above is clearly demonstrated in Fig. 4.2(b-d) where we plot the resulting steady-state field profiles when driving with three different peak amplitudes  $S_0 = 1.9, 2.1$ , and  $2.5$  respectively. In Fig. 4.2(b),  $S_0 < S_c$  and the CS is attracted to the peak. In Figs. 4.2(c,d)  $S_0 > S_c$  and therefore the driving field encompasses the critical value  $S_c$ . This forces the CS to be attracted to a point away from the peak of the driving field and settle at a position where  $S(\tau_{CS}) = S_c$ .

The results presented above suggest that CSs in the presence of amplitude modulated driving fields are attracted to positions where the driving field presents the nearest value to the critical value  $S_c$ . If the driving field profile does not contain  $S_c$ , the CS will be attracted to the extrema of the field (maximum or minimum) which achieves a local field value  $S(\tau)$  as near to  $S_c$  as possible. Extensive additional simulations (not shown here) confirm this hypothesis.

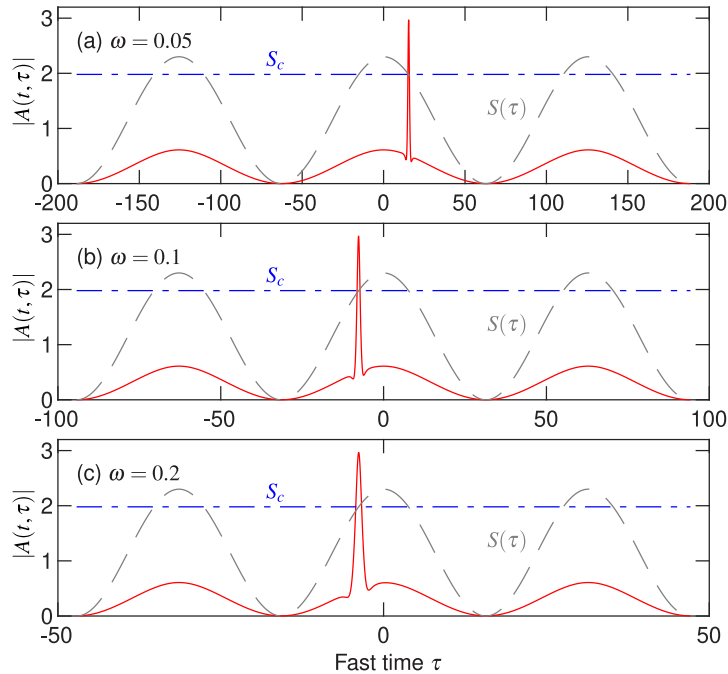


Figure 4.3: Steady-state field profiles (red curves) for a co-sinusoidal driving field with modulation frequencies (a)  $\omega = 0.05$ , (b)  $\omega = 0.1$ , and (c)  $\omega = 0.2$ . The CSs were initially excited at (a)  $\tau_0 = 1$ , (b)  $\tau_0 = -1$ , and (c)  $\tau_0 = -1$ . Gray dashed curves show the corresponding driving field profiles, while the dash-dotted horizontal blue curve highlights  $S_c = 1.98$ . All calculations use  $S_0 = 2.3$  and  $\Delta = 4$ . Note the different fast time axes in (a)-(c).

Additional simulations show that the critical value  $S_c$  towards which CSs are attracted does not depend on the driving field profile or the amplitude gradient at the position where  $S(\tau) = S_c$ , assuming the assumptions we stated previously about the width of the driving pulse relative to the CS remain true. In order to

show this, we consider a co-sinusoidal driving field of the form  $S(\tau) = (S_0/2)[1 + \cos(\omega\tau)]$ . By changing the frequency of the modulation,  $\omega$ , while leaving the peak amplitude constant, we can observe that the critical value  $S_c$  does not change even though the amplitude gradient at  $\tau_{CS}$  is different in each case. This is clearly shown in Fig. 4.3 where we can see that for three modulation frequencies, the value of  $S_c$  does not change. Because our driving field profile is symmetric about  $\tau = 0$ , there are two locations which satisfy  $S(\tau) = S_c$ . The position where the CS will come to rest is dependent on the initial position  $\tau_0$  of the CS in relation to the peak of the driving field  $\tau = 0$  as shown in Fig. 4.3.

The above simulations show that the critical value  $S_c$  does not depend on the profile or gradient of the driving field for a given value of the cavity detuning  $\Delta$ . This raises the question of the dependence of  $S_c$  on the detuning  $\Delta$ . To explore this, we repeat the simulations described above over a range of detunings, beginning with the onset of CS existence (approximately  $\Delta = 2$ ). We must also ensure that the driving pulse amplitude is sufficiently large to encompass the trapping value (whatever it may be). Therefore we use a Gaussian pulse with amplitude  $S_0$  which is approximately equal to the upper limit of CS existence for a given detuning  $\Delta$  [23]

$$S_0 \approx S_{\uparrow} = \left[ \frac{2}{27} \left( \Delta^3 + 9\Delta + \sqrt{\Delta^2 - 3} \right)^3 \right]^{1/2}. \quad (4.3)$$

This amplitude corresponds to the upper bound of the homogeneous bistability cycle of Eq. (4.1), and therefore the maximum driving amplitude for CS existence. After running a simulation for each value of  $\Delta$ , we extract the corresponding value of  $S_c$ .

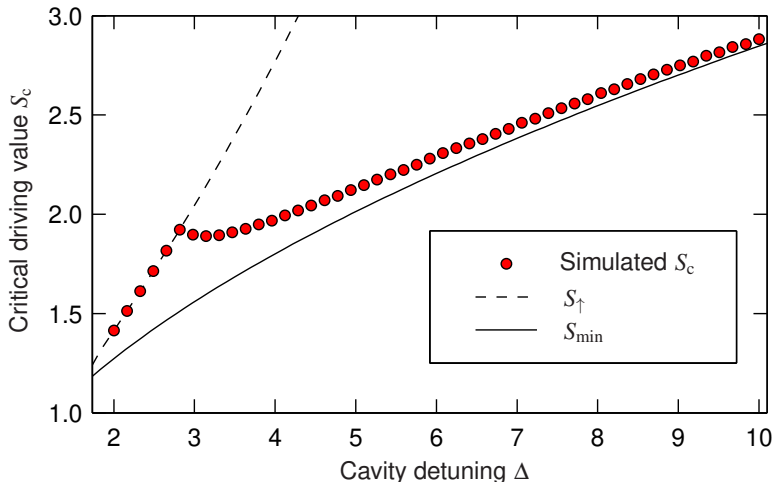


Figure 4.4: Critical driving field values  $S_c$  as a function of detuning. Red solid circles correspond to values extracted from numerical simulations, while the solid black curve highlights the minimum driving amplitude needed for CS existence:  $S_{\min} = (8\Delta/\pi^2)^{1/2}$ . Dashed black curve highlights the upswitching point  $S_{\uparrow} = [2/27(\Delta^3 + 9\Delta + \sqrt{\Delta^2 - 3^3})]^{1/2}$ , above which the homogeneous response of the LLE is monostable. CSs can exist between the dashed and solid curves.

In Fig. 4.4 we plot the critical driving value  $S_c$  obtained from our simulations as a function of the cavity detuning  $\Delta$ . Also shown are the maximum ( $S_{\uparrow}$ , dashed line) and minimum ( $S_{\min}$ , solid line) driving field amplitudes between which CSs can exist. Two different regimes showing qualitatively different behaviour can be identified. For small values of cavity detuning, ( $\Delta \lesssim 2.9$ ) we find that  $S_c \approx S_{\uparrow}$ . In this regime, a CS will always be attracted toward the local maximum of the driving field  $S_0$ . In contrast, for larger  $\Delta$ , the trapping level  $S_c$  approaches the minimum driving field amplitude  $S_{\min}$ . In this regime, the CS will be trapped at the edge of the driving field profile, and in the limit of  $\Delta \gg 1$ , drift to the lowest possible local value of  $S$  for which it can still exist. This latter behaviour is similar to the dynamics observed in quadratically nonlinear systems [84], where soliton motion was explained by their tendency to approach conditions of nonlinear resonance. Indeed, we find that, for a given detuning  $\Delta$ , our Kerr CSs reach their maximum amplitude and they are precisely in phase with the driving field when  $S \approx S_{\min}$ , thus evidencing the realization of resonance conditions.

The observation that, for  $\Delta \gtrsim 2.9$ , Kerr CSs can be trapped at the edge of the driving field profile is amenable to an interpretation in terms of the spontaneous symmetry breaking instability [79]. This can be readily seen by plotting the possible steady-state CS positions  $\tau_{CS}$  as a function of the peak driving strength  $S_0$ .

An example of such a bifurcation curve is shown in Fig. 4.5; the steady-state field profiles were obtained using a Newton-Raphson continuation algorithm with a Gaussian driving field and  $\Delta = 4$ . For small  $S_0$ , the CSs sit stably at the driving field maximum and there is only a single steady-state configuration (with  $\tau_{CS} = 0$ , blue curves). However, as  $S_0$  increases past the critical level  $S_c$ , a clear pitchfork bifurcation can be observed: the symmetric state with a CS at  $\tau_{CS} = 0$  becomes unstable and a pair of new asymmetric stable states emerge that consist of a CS sitting on either side of the driving field maximum.

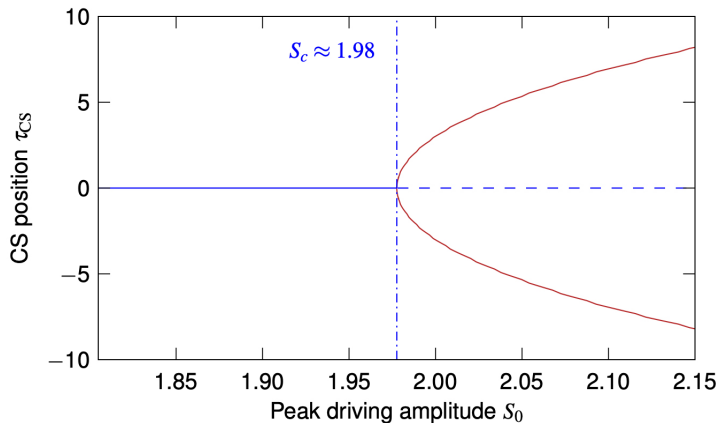


Figure 4.5: Cavity soliton symmetry breaking bifurcation curve for a Gaussian driving field with  $\tau_G = 20$  and  $\Delta = 4$ . Blue and red curves show the steady-state positions of the CS solutions as a function of the maximum driving amplitude for symmetric and asymmetric states, respectively, with the dashed part being unstable. The dash-dotted vertical line indicates the critical driving value  $S_c$ .

### 4.3 Intensity-modulation-induced drift rate

It is somewhat surprising that Kerr CSs can be trapped at a position where the driving field amplitude gradient is non-zero. As described by Maggipinto et. al. [see also Section 3.6] the CS's drift velocity, to first order, can be shown to be directly related to the local gradient of the driving field [72, 85]. Specifically, and as discussed in Section 3.6, the CS drift velocity can be expressed as

$$V_{drift} = \frac{d\tau_{CS}}{dt} = \frac{\langle v_0 | P(\tau) \rangle}{N}. \quad (4.4)$$

A purely amplitude modulated driving field can be locally approximated in the vicinity of a CS at  $\tau_{CS}$  as  $S(\tau) = S(\tau_{CS}) + P(\tau)$  where  $P(\tau) = dS/d\tau(\tau - \tau_{CS})$ .

Thus, we may write Eq. (4.4) as

$$V_{drift} = a \frac{dS}{d\tau} \Big|_{\tau=\tau_{CS}}, \quad (4.5)$$

where the proportionality coefficient  $a$  is described by

$$a = \frac{\langle v_0 | \tau - \tau_{CS} \rangle}{N}. \quad (4.6)$$

Equation (4.5) appears to predict that, as for phase inhomogeneities, CSs should remain stationary at driving field extrema where  $dS/d\tau = 0$ . The apparent discrepancy between our findings and Eq. (4.5) is explained by the fact that the CS's neutral mode changes with the driving strength (and detuning). As a consequence (and similarly to quadratically nonlinear systems [84]), the proportionality coefficient  $a$  in Eq. (4.5) also depends on the driving strength (and detuning), i.e.,  $a = a(S_H, \Delta)$ , where  $S_H = S(\tau_{CS})$ . This is illustrated in Fig. 4.6, where we explicitly show  $a(S_H, \Delta)$  computed for a range of cavity driving strengths and detunings. This was calculated from the neutral modes of steady-state CS solutions for homogeneous driving field of strengths  $S_H$  which are projected along the fast time variation represented by the perturbation before being normalised to the characteristic CS.

As can be seen, the coefficient  $a$  decreases with increasing driving strength and for  $\Delta \gtrsim 2.9$  crosses zero within the region of CS existence. Moreover, we see that the curve  $a(S_H, \Delta) = 0$  matches exactly with the critical driving field values found through direct split-step simulations of Eq. (4.1) with an inhomogeneous driving field (cf. Fig. 4.4). These findings fully corroborate our observations of CS behaviour in the presence of driving field amplitude inhomogeneities. Specifically, when a CS drifts along an amplitude gradient, the coefficient  $a$  it experiences changes continuously. At the critical level  $S_c$ , the coefficient passes through zero and changes sign, thus enabling robust trapping at that level. On the other hand, while the maximum (or minimum) of the driving field (with  $dS/d\tau = 0$ ) always corresponds to an equilibrium position, that equilibrium position is unstable (cf. Fig. 4.5) if the maximum (minimum) is larger (smaller) than the critical driving value  $S_c$ . There is therefore no contradiction between our findings and Eq. (4.5). The CS velocity is ‘‘locally’’ proportional to the driving field gradient [as described by Eq. (4.5)], but because the proportionality coefficient changes as the CS drifts, the overall relationship is more complex. Rigorously speaking, the CS velocity is proportional to the driving field gradient only over short slow time intervals

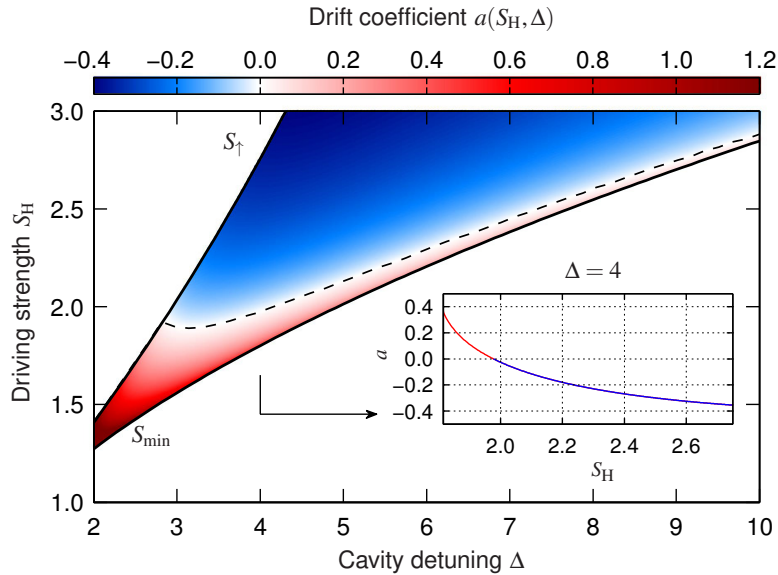


Figure 4.6: Drift coefficient  $a(S_H, \Delta)$  calculated from the neutral mode of a steady-state CS solution for a range of homogeneous driving strengths  $S_H$  and cavity detunings  $\Delta$ . The solid black curves correspond to  $S_{\min}$  and  $S_{\uparrow}$  as defined previously. The black dashed curve shows the critical driving field values  $S_c$  obtained from direct numerical simulations of the LLE with a Gaussian driving field profile. The inset shows the curve  $a(S_H, \Delta = 4)$ .

during which the local driving strength, and hence the coefficient  $a(S_H, \Delta)$ , experienced by the CS remains approximately constant. It is also worth highlighting that, because the drift coefficient  $a(S_H, \Delta)$  only depends on the local value of the driving field  $S_H$  and the detuning  $\Delta$ , the analysis above readily explains why the critical trapping level  $S_c$  does not depend on the precise profile of the driving field (provided that the driving field varies slowly compared to the CS duration).

### 4.3.1 Physics of cavity soliton motion

To better understand the physics that underpins the CS behaviour identified above, we next present results from simulations of an Ikeda-like map[52]. Unlike the mean-field approximation of Eq. (4.1), this approach allows us to isolate effects due to (i) propagation through the Kerr medium over a single cavity round-trip and (ii) the coherent injection of the driving field into the cavity. We write the map equations in dimensionless form that allows immediate comparison with

results from Eq.(4.1):

$$\frac{\partial A_m(\xi, \tau)}{\partial \xi} = i \frac{\partial^2 A_m}{\partial \tau^2} + i |A_m|^2 A_m, \quad (4.7)$$

$$A_{m+1}(\xi = 0, \tau) = \sqrt{1 - 2\alpha} A_m(\xi = \alpha, \tau) e^{-i\delta_0} + \alpha S(\tau). \quad (4.8)$$

Here Eq. (4.7) is the NLSE which describes the evolution of the intracavity field over one cavity round-trip, with  $\xi = \alpha z/L$  a dimensionless propagation coordinate, while Eq. (4.8) is the boundary condition that describes the addition of the coherent driving field to the intracavity light field at  $\xi = 0$ . For high-finesse cavities, the loss coefficient  $\alpha \ll 1$  and the above map equations can be averaged to the LLE, Eq. (3.5). To better capture the evolution of the CS over one cavity round-trip, we have used a comparatively large value of  $\alpha = 0.15$  in the simulations that will follow.

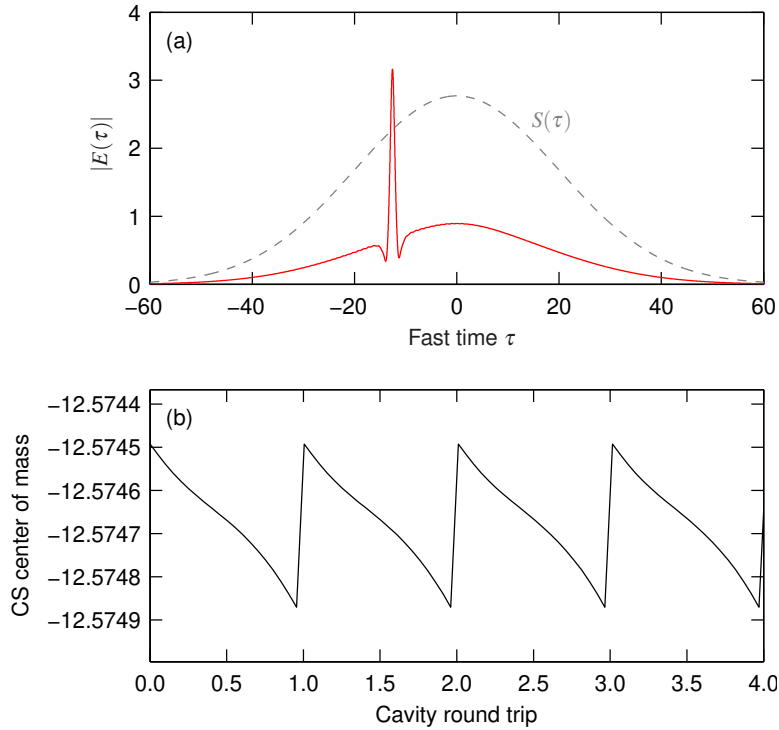


Figure 4.7: Simulation results from an Ikeda-like cavity map. (a) Steady-state intracavity field profile (red curve) for a Gaussian driving field (gray dashed curve). (b) Evolution of the CS's center of mass over four cavity transits (in dimensionless fast time in the standard LLE reference frame where solitons are stationary in the absence of inhomogeneities).

Figure 4.7(a) shows a steady-state intracavity field obtained from the Ikeda map with  $\Delta = 4$  and a Gaussian driving field profile with  $S_0 = S_{\uparrow} \approx 2.77$  and  $\tau_G = 20$ . One first notes that the Ikeda map reproduces the salient result of the LLE simulation, i.e., the CS trapping at a position where the driving field gradient is non-zero. The precise trapping value  $S_c \approx 2.27$  is somewhat larger than the value found in corresponding mean field simulations, which we attribute to the comparatively large value of  $\alpha$ . Indeed, we have carefully verified that the Ikeda map reproduces the LLE result in the limit of very small  $\alpha$ .

To gain insights into the interplay between propagation over one round-trip [described by Eq. (4.7)] and addition of the coherent driving [Eq. (4.8)], Fig. 4.7(b) shows the evolution of the CS's center of mass in the fast time dimension (calculated over the CS's half maximum points) over four consecutive round-trips after steady state is reached. As can be seen, the CS drifts gently downward away from the driving field maximum during propagation, but is pulled back to its original position at the boundary. This competition between propagation and coherent driving underpins the behaviour of CSs in the presence of pulsed or amplitude modulated driving fields. Specifically, if the propagation effect is stronger (weaker) than the driving effect, the coefficient  $a$  in Eq. (4.5) is negative (positive) such that the CS will drift away from (towards) the maximum. In contrast, at the critical driving strength  $S_c$ , the two effects are precisely balanced.

The physics behind the two competing effects identified above can be qualitatively explained as follows. First, the addition of the driving field can be intuitively understood to shift the CS towards its maximum because the two are almost in phase. In contrast, the CS's drift away from the maximum during propagation is due to the phase shift between the CS and the intracavity background field. Considering a superposition field  $A(\xi, \tau) = A_s(\xi, \tau) + \delta A(\xi, \tau)$  that consists of an NLSE soliton  $A_s$  perturbed by a small amplitude background field  $\delta A$ , it is well known that the perturbation can cause the soliton to drift, with the rate of drift given by the inverse group velocity [86]

$$\frac{\Delta\tau_S}{\Delta\xi} = -\frac{1}{B} \text{Im} \int \frac{\partial A_s^*}{\partial \tau} \delta A dt, \quad (4.9)$$

where  $\Delta\tau_S$  and  $B$  represent the soliton's temporal position and amplitude, respectively. Straightforward analysis of Eq. (4.9) confirms that, when  $\Delta\phi = \phi_S - \phi_\delta \in [0, \pi]$ , where  $\phi_S$  and  $\phi_\delta$  denote respectively the phases of the soliton [as seen in Eq. (3.17)] and the phase of the background, the soliton will drift away from the perturbation maximum while the opposite is true for  $\Delta\phi > \pi$ . (We have also confirmed these predictions by means of direct numerical simulations of the NLSE

Eq. (4.7).) For Kerr CSs, the two phases are approximately (in the mean-field limit) given by [22, 24]

$$\phi_S \approx \cos^{-1} \left( \frac{\sqrt{8\Delta}}{\pi S} \right), \quad (4.10)$$

$$\phi_\delta \approx -\tan^{-1}(\Delta). \quad (4.11)$$

As CSs exist only for  $\Delta > 0$ , one always finds  $\Delta\phi \in [0, \pi]$ , explaining the soliton's downward motion over a single cavity round trip. It is worth noting that, if the CS sits at an extremum of the driving field (where  $\partial A_s^*/\partial\tau = 0$ ), this motion vanishes [see Eq. (4.9)]. Because the addition of a parity symmetric driving field will likewise induce no shifts in this situation, we can see how the driving field extrema indeed correspond to equilibria, whose stability is governed by the relative strengths of the two competing effects.

## 4.4 Summary

We have investigated the dynamics of Kerr CSs in the presence of driving fields with inhomogeneous amplitude profiles. In stark contrast to the case of phase inhomogeneities, we have shown that the CSs are not in general attracted to maxima (or minima) of an amplitude-modulated driving field. Instead, the CSs are attracted to, and trapped at, positions associated with particular values of the driving field. We have described the underlying physics in terms of a spontaneous symmetry breaking instability that arises from a competition between the coherent addition of the driving field and propagation in the Kerr medium [39].

## Chapter 5

# Impact of desynchronization on intensity trapping of temporal cavity solitons

In the previous Chapter we assumed that the driving pulse train was synchronized to the round-trip time of the cavity, allowing us to investigate the dynamics in the absence of external or undesirable variables. In practice, this synchronization is generally difficult or impossible to achieve. While it is well known that a mismatch between the pump pulse repetition rate and the cavity round-trip time can have significant impact on the bistability dynamics of driven passive Kerr resonators [87], the influence of such desynchronization on CSs has not yet been extensively studied. Parra-Rivas et al. considered the impact of desynchronization when the driving field is composed of a small-intensity perturbation (shorter than the CSs) atop a cw driving field, demonstrating that the resulting temporal drift can affect the stability of CSs [80].

Findings from these early studies [80, 87] cannot, however, be immediately translated to situations pertinent to recent experiments where the driving field comprises of temporally localized pulses longer than the CSs with no CW background [81–83]. Preliminary simulations show that, in accordance with the general behaviour of dissipative solitons in the presence of convective drift [33, 88, 89], CSs can remain (frequency) locked to the driving pulse train over a finite range of desynchronization, but their trapping positions are shifted compared to the situation of perfect synchronization (as was considered in the previous Chapter). Due to the significant application potential of CSs in resonators driven by optical

pulses [81–83], there is clearly a need for a more detailed understanding of the impact of desynchronization on CS dynamics.

In this Chapter we show that, for typical driving pulse profiles, desynchronization gives rise to asymmetric shifts of the CS trapping positions, which can influence the multiplicity of possible CS configurations that the system can support. In particular, we show that desynchronization can be leveraged to guarantee operation in the single-soliton regime, which due to the smooth spectral envelope characteristic of the regime is often most attractive for practical applications, especially those involving soliton-based microresonator frequency combs [89]. We also investigate the interplay between stimulated Raman scattering and pump-resonator desynchronization, finding evidence of rich dynamics that explain the CS behaviors observed—but not fully explained—in recent experiments [81].

## 5.1 Numerical model

We again consider a Kerr resonator with anomalous dispersion that is driven with a train of pulses. As detailed in the previous Chapter, under suitable parameter conditions, a short CS can form atop the driving pulse envelope. In this Chapter, however, we are interested in situations where the period of the driving pulse train,  $t_P$ , is different from the intrinsic cavity round-trip time,  $t_R = FSR^{-1}$ . As shown in ref. [77], this can be represented as a slow time varying driving field such that  $S(\tau) \rightarrow S(\tau + d \times t)$  where  $d$  describes the drift (in fast time) of the intracavity field with respect to the pump pulse per unit slow time (in the absence of any trapping). Changing reference frames such that the pump is stationary,  $\tau \rightarrow \tau - d \times t$ , we can model this system using a dimensionless LLE that includes a convective drift term [87]:

$$\frac{\partial A(t, \tau)}{\partial t} = \left[ -1 + i(|A|^2 - \Delta) - d \frac{\partial}{\partial \tau} + i \frac{\partial^2}{\partial \tau^2} \right] A + S(\tau). \quad (5.1)$$

Because Eq. (5.1) is expressed in a reference frame where the driving pulse is stationary, desynchronization manifests itself as a constant time-domain drift of intracavity features that are not (fully or partially) locked to the driving pulse. The drift coefficient  $d$  is related to the corresponding dimensional parameter  $\Delta t = t_R - t_P$  through the normalization  $d = \Delta t \sqrt{2\mathcal{F}} / (|\beta_2| L \pi)$ . Again, we consider a Gaussian driving field profile,  $S(\tau) = S_0 \exp[-\tau^2 / (2\tau_g^2)]$ , where  $\tau_g$  and  $S_0$  represent the duration and amplitude of the driving pulse, respectively. In line with recent experiments and the previous Chapter, we focus on the situation where the duration

of the driving pulses are (much) longer than the duration of the CSs ( $\tau_g > \Delta^{-1/2}$ ), though we must emphasize that our general findings are not restricted to any particular driving field profile or set of parameters.

As noted in Ref. [80], there are numerous distinct mechanisms that can give rise to desynchronization and drift. In addition to the pump pulse repetition rate being offset from the cavity FSR, drifts can arise due to higher-order linear and nonlinear effects (such as higher-order dispersion or stimulated Raman scattering) that shift the center wavelength of the CS away from the driving wavelength. The drift term  $d$  in Eq. (5.1) can at least qualitatively capture the salient dynamics regardless of the physical origins of desynchronization. Of course, if the higher-order linear or nonlinear effects are sufficiently strong—such that their impact is not restricted to simply inducing a drift—then Eq. (5.1) must be augmented with additional terms that more rigorously describe the pertinent effects. We will demonstrate this by analysing the impact of stimulated Raman scattering (SRS) in Section 5.3.

## 5.2 Illustrative simulations

As stated in the previous Chapter, for typical parameters of interest ( $\Delta \gg 1$  and  $S_0 \gg S_{\min}$  where  $S_{\min}$  is the minimum driving amplitude for which CSs can be supported), only the  $a(S, \Delta) = 0$  equilibria are stable, in accordance with Eq. (4.5). Therefore, a CS will be attracted to (and trap at) positions  $\tau$  for which  $a(S, \Delta) = 0$ . In the  $\Delta \gg 1$  regime, driving field value  $S_c$  at this trapping position approaches the minimum value for supporting CSs  $S_{\min}$ . Figure 5.1(a) depicts a typical drift velocity profile due to the intensity gradient in the  $S_0 > S_c$  regime (red dashed line), together with the intensity profile of the corresponding driving pulse (blue line) [see caption for parameters]. As expected, there are two stable trapping positions  $\tau_c$  [i.e., positions where  $S(\tau_c) = S_c$ ] that are symmetrically detuned with respect to the peak of the driving pulse. In steady-state, a CS can be trapped at either one of those positions, either singly or simultaneously. This is illustrated in Figs. 5.1(b)–(g), which show examples of temporal [Figs. 5.1(b–d)] and spectral [Figs. 5.1(e–g)] profiles of numerically simulated steady state field configurations with no desynchronization present. These results were obtained by numerically integrating Eq. (5.1) with a split-step Fourier algorithm, assuming initial conditions that result in the excitation of a CS slightly to the left [Fig. 5.1(b, e)] or right [Fig. 5.1(c, f)] of the peak of the driving field [Fig. 5.1(d, g) was obtained by simultaneously exciting CSs at both sides of the peak].

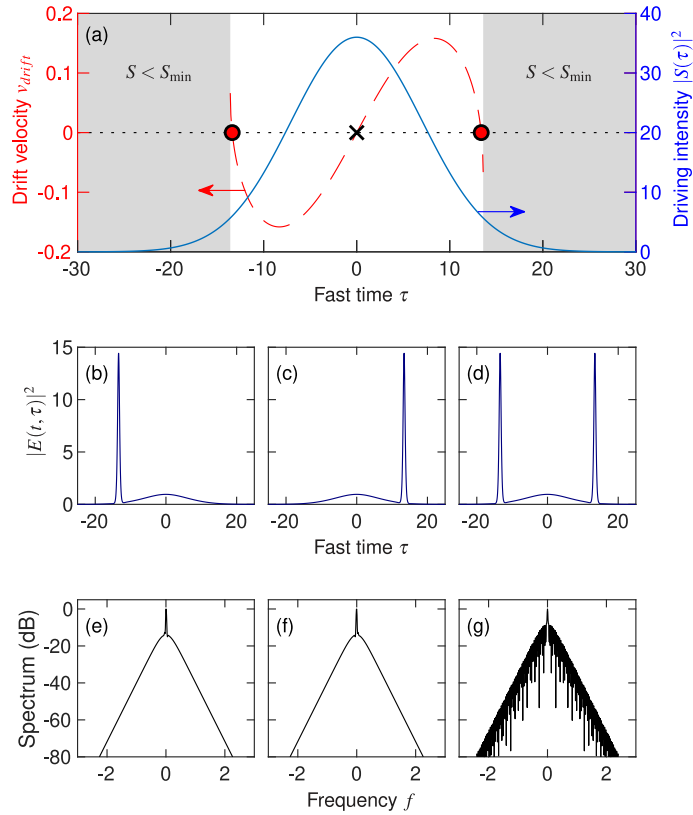


Figure 5.1: (a) Red dashed curve shows the drift velocity due to the amplitude inhomogeneity of a Gaussian driving field (blue solid curve) with amplitude  $S_0 = 6$  and duration  $\tau_g = 10$ . The cavity detuning  $\Delta = 7$ . Red solid circles (black cross) highlight stable (unstable) trapping positions. CSs do not exist in the gray shaded area, where the local driving field level is smaller than the minimum required for CS existence. (b–d) Temporal profiles of the three possible CS states that can manifest themselves for the parameters listed in (a). (e–g) Spectral profiles corresponding to (b–d), respectively.

It is interesting to note that the three configurations shown in Fig. 5.1 are the *only* CS configurations that the chosen simulation parameters support. In particular, we find that excitation of multiple CSs on the same side of the pump pulse leads to merging or annihilation at the corresponding trapping position [90]. This behaviour appears to be universal as we have not identified parameters that would permit states with more than two CSs. However, in the presence of strong

higher-order effects that can give rise to bound soliton states [91] we expect this behaviour to change.

In this Chapter, we are interested in the effect desynchronization has on the trapping positions and overall dynamics of CSs driven by a pulsed driving field. With the introduction of desynchronization, ( $d \neq 0$ ), a CS will experience an additional convective drift, at a rate that is governed by the drift coefficient  $d$  [80]. The total drift of the CS relative to the pump pulse is then:

$$v = a(S, \Delta) \left. \frac{dS}{d\tau} \right|_{\tau=\tau_{CS}} + d. \quad (5.2)$$

Because of desynchronization, the stable CS trapping sites are shifted to new positions where  $a(S, \Delta)dS/d\tau = -d$ ; at these positions, drift due to desynchronization is exactly balanced by the motion induced by the inhomogeneity of the driving field. It should be clear that, for typical pulsed driving fields (with  $S_0 > S_c$ ), both trapping positions shift in the same direction, thus breaking the symmetry of the double-soliton state [cf. Fig. 5.1(a)]. Compounded by the localized nature of a pulsed driving field, such shifting can influence the number of possible CS configurations. This is particularly evident at higher detunings ( $\Delta \gtrsim 5$ ), where the trapping positions in the absence of desynchronization are already very close to the minimum driving field value for which CSs can exist ( $S_{\min}$ ) as described in the previous Chapter. In this regime, even a small desynchronization can cause one of the trapping positions to fall below this minimum value, hence reducing the number of possible CS configurations from three to one, thus ensuring single-soliton operation. The advantage of single-soliton operation is highlighted in Fig. 5.1(e–g) where the contrast between the smooth spectrum of a single CS and the modulated spectrum of dual CSs is evident.

Figure 5.2(a) shows results from numerical simulations that illustrate the dynamics described above [parameters as in Fig. 5.1]. Here, desynchronization is initially absent ( $d = 0$ ) and two CSs are excited at either side of the pump pulse. At a slow time of  $t = 50$ , we introduce a desynchronization ( $d = -0.1$ ) which causes both CS trapping positions to shift towards the leading (left) edge of the pump pulse. Significantly, while the trailing (right) CS simply adjusts to its new trapping position, the leading CS ceases to exist as it is pushed below the minimum driving field amplitude  $S_{\min}$ .

A more comprehensive analysis of the impact of desynchronization in the large- $\Delta$  regime is shown in Fig. 5.2(b). Here, the solid blue (dashed red) curves show steady-state positions of stable (unstable) CSs solutions of Eq. (3.3) as a function

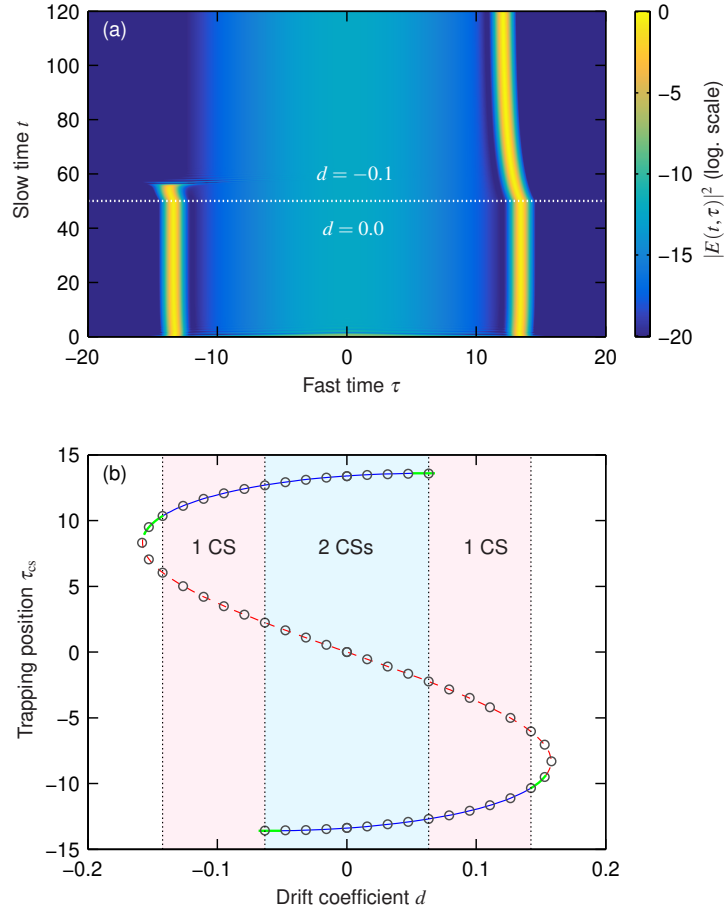


Figure 5.2: (a) False color plot showing the evolution of the intracavity field intensity when de-synchronization with  $d = -0.1$  is abruptly introduced at slow time  $t = 50$  (highlighted by the horizontal dotted line). Other parameter as in Fig. 5.1. (b) Solid blue, dashed red, and solid green curves show the positions of CS solutions of Eq. (5.1) as a function of the drift coefficient  $d$ , obtained using a Newton continuation algorithm. The solid blue curve corresponds to stable solutions, dashed red curve corresponds to the trivially unstable  $dS/d\tau = 0$  trapping position, while the solid green curves indicate more complex instabilities [see main text]. An additional branch of trivially unstable CSs that connects the two end-points is not shown for clarity. Open gray circles show trapping positions found by directly solving the roots of the equation  $v = 0$ , where  $v$  is given by Eq. (5.2).

of the drift parameter  $d$ , obtained using a Newton continuation algorithm. Also shown, as open circles, are the trapping positions predicted by directly finding the roots of Eq. (5.2). Several conclusions can be drawn. First, we see that the roots of Eq. (5.2) agree very well with the trapping positions extracted from Newton calculations. Second, for drift values close to zero, possible stable CS positions exhibit

bistability (blue shaded area), i.e., all three CS configurations demonstrated in Fig. 5.1 can be sustained. (Note: while the CS positions exhibit *bistability*, the CS configurations in fact exhibit *tristability*, as CSs can occupy the possible trapping positions either independently or simultaneously.) Last, for values of  $d$  outside this region of bistability, only one stable CS configuration, consisting of a single CS trapped either on the trailing ( $d < 0$ ) or leading ( $d > 0$ ) edge of the pump pulse, is possible (red shaded areas).

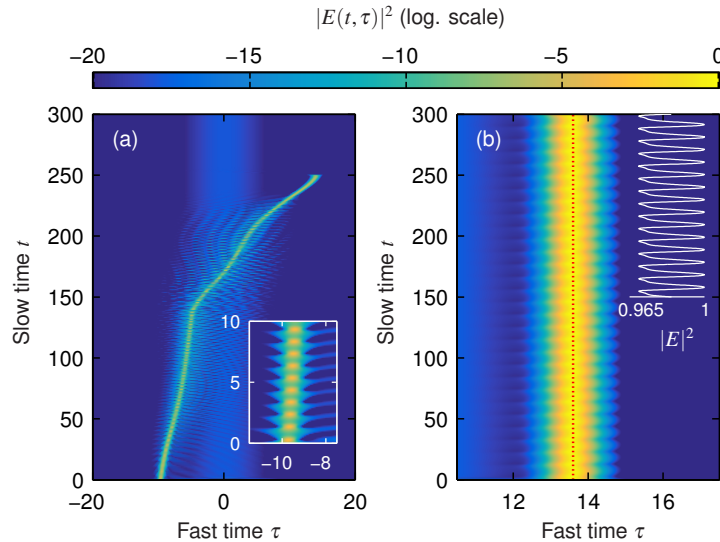


Figure 5.3: Simulated intracavity dynamics of unstable CSs for (a)  $d = 0.15$  and (b)  $d = 0.06$  with other parameters as in Fig. 5.1. Both simulations use an initial condition comprised of a soliton-like perturbation close to its predicted trapping position. The inset in (a) shows the evolution over a smaller range of slow time so as to highlight the oscillatory nature of the instability. The dotted vertical line in (b) indicates the temporal position  $\tau_{\min}$  which satisfies  $S(\tau_{\min}) = S_{\min}$ . The inset in (b) shows the evolution of the normalized soliton amplitude  $|E|^2 = |E(t, \tau_{\min})|^2 / \max[|E(t, \tau_{\min})|^2]$  from slow time  $t = 150$  onwards. Note the different x-axes in (a) and (b).

In addition to affecting the possible CS configurations, desynchronization can also give rise to CS instabilities. In particular, for sufficiently large driving amplitudes, it is possible that one of the trapping positions shifts to a position where the local value of the driving field exceeds the well-known CS Hopf bifurcation threshold [35]. Indeed, this situation can be observed in Fig. 5.2(b), where the CS solutions are found to become unstable for drift values  $|d| > 0.14$  (solid green curves). Dynamical split-step simulations show that, in this regime, the CSs breathe with

slow time  $t$  (as in the case of CW driving [35]), but do not remain trapped at a specific position. Rather, as shown in Fig. 5.3(a), they become unlocked, pass over the peak of the driving pulse, and subsequently cease to exist. Interestingly, instabilities can also arise when desynchronization shifts the CSs away from the peak of the driving pulse and closer to the minimum driving amplitude  $S_{\min}$ . More specifically, we find that, for a small range of de-synchronizations, a CS can exhibit persistent temporal oscillations around the point where their existence would be expected to cease under conditions of CW driving [see Fig. 5.3(b)]. The range of desynchronizations where such instabilities manifest themselves (as well as the magnitude of the temporal oscillations) appears to increase as the pump pulse duration decreases, presumably due to the corresponding increase in the underlying amplitude gradient.

The behaviour summarized in Fig. 5.2 manifests itself at higher detuning values ( $\Delta \gtrsim 5$ ), as it is only in this regime that the trapping positions in the absence of desynchronization are very close to the minimum value of CS existence. However, we have found that desynchronization also affects CS existence at lower detunings, though a slightly different mechanism causes this. At these lower detunings, CS trapping positions in the absence of desynchronization lie between the minimum and maximum values of CS existence. Accordingly, a CS can tolerate a considerable shift *away* from the peak to a lower value of the driving field without ceasing to exist, in stark contrast to the larger detuning case discussed above. A situation can then arise where the trapping position shifting towards the peak of the pump pulse ceases to exist before the one shifting away from the peak. In this situation, if two CSs co-exist initially, desynchronization forces the CSs to collide, leaving just one CS at the only remaining trapping position.

Figure 5.4(a) shows simulation results that illustrate these dynamics [see caption for parameters]. The simulation starts from a two-soliton configuration in the absence of desynchronization. At a slow time of  $t = 300$ , we introduce a small desynchronization ( $d = -0.07$ ) and observe how the trailing CS becomes unlocked, traveling over the peak of the pump pulse towards the one remaining trapping position. As the leading CS is already occupying this position, the two CSs interact and merge together. In Fig. 5.4(b), we plot the CS trapping positions as a function of the drift coefficient for  $\Delta = 4$  [curves obtained in the same fashion as those shown in Fig. 5.2(b)]. We again see the S-shape characteristic to bistability; however, in contrast to the large-detuning case [cf. Fig. 5.2(b)], the sign of the drift coefficient required to ensure a single trailing or leading CS is the opposite. This

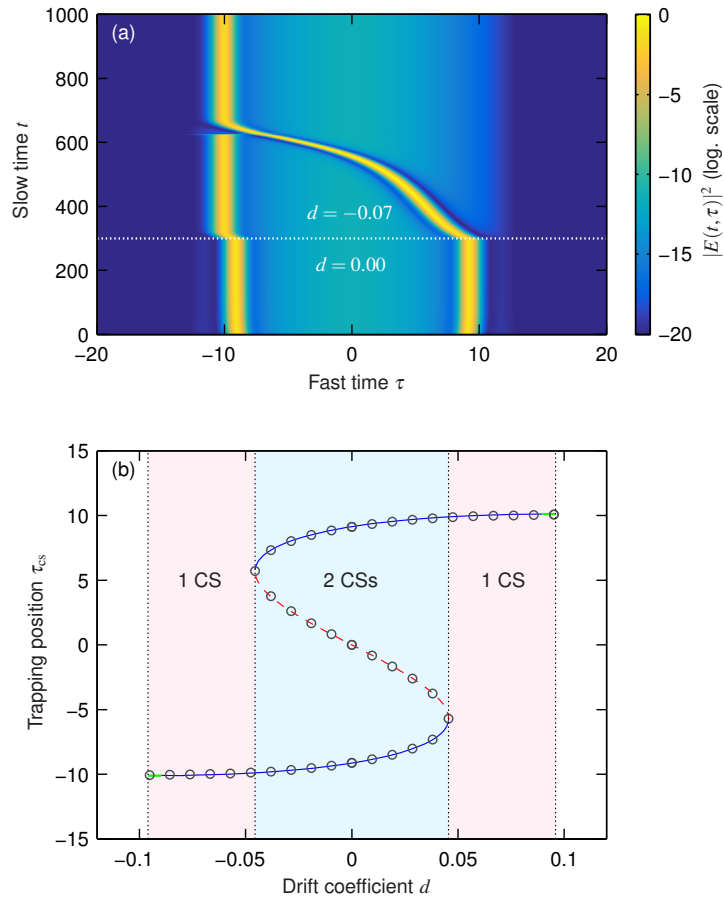


Figure 5.4: Numerical results for a cavity detuning of  $\Delta = 4$ , driving pulse amplitude  $S_0 = 3$ , and driving pulse width  $\tau_g = 10$ . (a) Evolution of the intracavity field intensity when de-synchronization with  $d = -0.07$  is abruptly introduced at slow time  $t = 300$  (highlighted by the horizontal dotted curve). (b) As in Fig. 5.2, blue, green, and red curves show the positions of stable and unstable CS solutions of Eq. (5.1) as a function of the drift coefficient  $d$ . Open gray circles show trapping positions found by directly solving the roots of the equation  $v = 0$ , where  $v$  is given by Eq. (5.2).

is simply a manifestation of the different mechanism that underpins the removal of the two-soliton state.

The results reported above show that pump desynchronization can be harnessed to ensure single-soliton operation in Kerr resonators via two qualitatively different mechanisms. Due to the fashion in which the CS trapping positions depend on the detuning, the mechanism shown in Fig. 5.2 (Fig. 5.4) is more likely to manifest itself for larger (smaller) detunings. Nonetheless, it should be clear

that the precise pump amplitude and profile also play a role in determining which one of the scenarios prevails (i.e., which of the trapping positions persists longer as the de-synchronization increases). Moreover, there exists a set of pump and detuning parameters for which both stable trapping positions disappear simultaneously; in this case, protected single-soliton operation cannot be achieved for any desynchronization.

Regardless of the mechanism, it should be clear that (single) soliton operation can be sustained only for sufficiently small desynchronizations [within the shaded regions of Fig. 5.2(b) and Fig. 5.4(b)] so that one of the trapping positions persists, allowing a CS to remain (frequency) locked to the driving field. The locking range, i.e., the range of desynchronization that a CS can tolerate, can be obtained from Eq. (5.2). Specifically, the maximum desynchronization that can be compensated for by the pump inhomogeneity is:

$$|d_{\max}| = \max \left| a(S, \Delta) \frac{dS}{d\tau} \right|. \quad (5.3)$$

In dimensional units, this yields a maximum tolerable drift per round trip of  $\Delta t_{\max} = d_{\max} \sqrt{|\beta_2| L \pi / (2\mathcal{F})}$  and a corresponding repetition frequency mismatch of  $\Delta f_{\max} = \text{FSR}^2 \Delta t_{\max}$ . Because the coefficient  $a(S, \Delta)$  depends on the local value of the driving field, it is not possible to express the locking range as a simple product involving a constant coefficient and the maximum slope of the driving field (as is the case for phase modulated driving fields [33]). Rather, evaluating the locking range requires knowledge of the full functional dependence of  $a(S, \Delta)$  as discussed in the previous Chapter.

### 5.3 Detuning dependent dynamics and effect of stimulated Raman scattering

Our analysis has so far revolved around isolated values of the cavity detuning. To gain more insights, we next consider how desynchronization affects the cavity dynamics as the detuning is continuously (and adiabatically) scanned over a resonance as this method is commonly used to study CSs experimentally [81]. To facilitate comparisons with prior studies, we consider experimental results reported by Obuzurd et. al. in [81] where pico-second pulses were used to drive a Fabry-Pérot type microresonator in order to generate soliton-based frequency combs. The repetition rate of this pulse train could be tuned in order to change the

repetition rate of the CS: a close analogy to our model of CS trapping is the presence of desynchronization. Comparing our results to such experimental results can help us gain a more in depth understanding of the effects that desynchronization can have on CS dynamics in resonators driven with amplitude modulated driving fields. To this effect, we choose a comparatively short pulse width of  $\tau_G = 4$  and perform simulations for a wide range of different drift coefficients  $d$ . For each value, we simulate the intracavity dynamics as the detuning is slowly scanned from negative to positive values, mimicking the experimental procedure employed in [81]. Figures 5.5(a)–(c) depict the evolution of the average intracavity power as the detuning is scanned for three different values of the drift coefficient  $d$  [see caption]. For each value, the evolution of the intracavity power is indicative of the well-known Kerr cavity dynamics covered in Chapter 3. Indeed, as the detuning increases, a chaotic modulation instability regime is followed by a distinct “soliton step” [24]. The length of the soliton step is found to decrease with increasing magnitude of the drift coefficient  $|d|$  – a feature that will be discussed in the following paragraph. Figure 5.5(d) shows temporal dynamics for the  $d = 0$  case, and we see how, at a detuning of about  $\Delta \approx 5$ , a single CS forms on the leading edge of the driving pulse, persisting until the detuning reaches the maximum value of CS existence,  $\Delta_{\max} = \pi^2 S_0^2 / 8 \approx 18.5$ . It is worth noting that, because for  $d = 0$  the system is perfectly symmetric, a CS can be expected to form with equal probability on the leading or the trailing edge of the driving pulse. In contrast, for  $d \neq 0$ , the symmetry of the system is explicitly broken [92], and the CSs preferentially form either on the leading ( $d < 0$ ) or the trailing ( $d > 0$ ) edge of the pump pulse.

Figure 5.5(e) shows the evolution of the average intracavity power over a much wider range of drift coefficients. We can make two important observations. First, the CS portions of the scan traces are (approximately) symmetric with respect to  $d = 0$  (as expected based on the symmetry of the driving pulse). Second, the range of CS existence (in detuning) decreases as the magnitude of the drift coefficient increases. This latter observation can be explained as follows. As detuning increases, the critical driving field value  $S_c$  towards which the CSs are attracted in the absence of desynchronization ( $d = 0$ ) asymptotically approaches  $S_{\min}$  — the minimum value for which CSs can still exist. For  $d > 0$  ( $d < 0$ ), the explicit symmetry breaking induced by the desynchronization favours CS formation on the trailing (leading) edge of the driving pulse, which is also the direction towards which the CS trapping positions are shifted. Taken together, as the detuning increases, the desynchronization needed to push the CS below the minimum driving

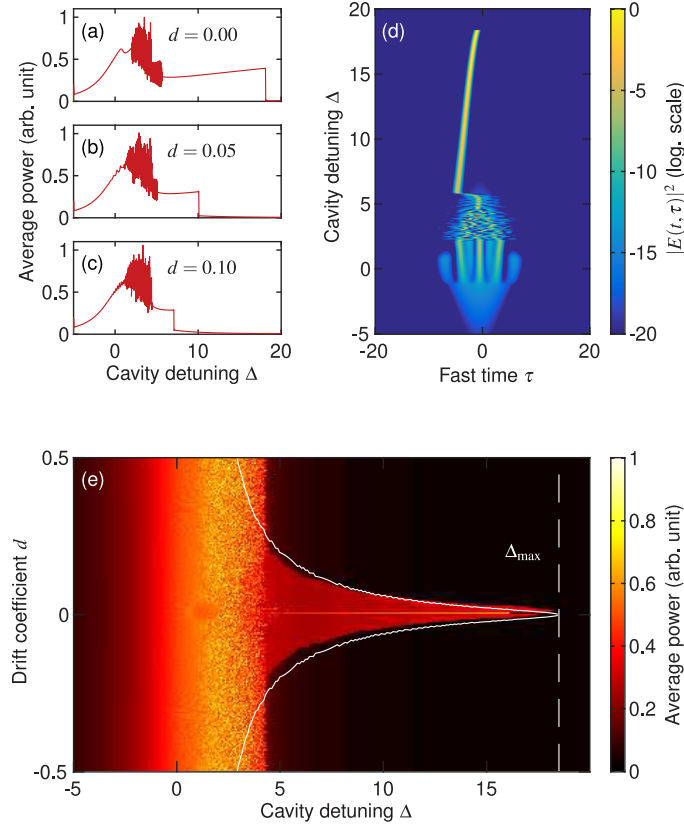


Figure 5.5: (a–c) Average intracavity power as the detuning is scanned over the cavity resonance for different drift coefficients  $d$  as indicated. (d) Dynamical evolution of the intracavity field intensity as the detuning is scanned over the resonance for  $d = 0$ . (e) False colour plot of scan traces as in (a–c) for a range of different drift coefficients  $d$ . Solid white curves highlight the maximum de-synchronization that a CS can tolerate when excited by scanning the detuning [as described in the main text]. The dashed vertical white line corresponds to the absolute maximum detuning of CS existence, i.e.,  $\Delta_{\max} = \pi^2 S_0^2 / 8$ . Simulations use  $S_0 = \sqrt{15}$  and  $\tau_g = 4$ .

level  $S_{\min}$  decreases. Accordingly, the range of detunings over which CSs can exist decreases as the magnitude of desynchronization increases.

To corroborate our explanation, the white curves in Fig. 5.5(e) highlight the maximum de-synchronization that a CS on the trailing or leading edge of the pump pulse can tolerate when  $d > 0$  or  $d < 0$ , respectively, as a function of detuning  $\Delta$ .

These curves were obtained by evaluating the velocity  $v = a(S_{\min}, \Delta)dS/d\tau|_{\tau=\tau_{\min}}$ , where  $\tau_{\min}$  satisfies  $S(\tau_{\min}) = S_{\min}$ . As can be seen, the theoretical predictions are in excellent agreement with the range of CS existence observed in numerical simulations. It is worth emphasizing that the maximum tolerable de-synchronization depicted in Fig. 5.5(e) does not coincide with  $d_{\max}$  given by Eq. (5.3): the latter represents an absolute maximum, and may require that the CS resides on the leading (trailing) edge of the driving pulse when  $d > 0$  ( $d < 0$ ), which is not the case when the CSs form spontaneously as the detuning is scanned.

It is very interesting to note that the simulation results shown in Fig. 5.5(e) differ markedly from corresponding experimental results reported in Ref. [81]. In particular, experiments show soliton steps that are distinctly asymmetric as a function of desynchronization. We suspect this discrepancy arises from the presence of some other mechanism that explicitly breaks the system's symmetry, hence affecting the soliton trapping positions. Recalling that the resonator used in Ref. [81] was made out of fused silica, we may identify stimulated Raman scattering (SRS) as a potential process that could explain the observations.

To test our hypothesis, we have repeated the simulations shown in Fig. 5.5(d) with the inclusion of the full Raman response of fused silica. More specifically, our simulations use the following modified LLE [93]:

$$\begin{aligned} \frac{\partial A(t, \tau)}{\partial t} = & \left[ -1 - i\Delta - d\frac{\partial}{\partial \tau} + i\frac{\partial^2}{\partial \tau^2} \right] A + S(\tau) \\ & + i \left[ (1 - f_R)|A|^2 + f_R [\Gamma(\tau, \tau_s) * |A|^2] \right] A. \end{aligned} \quad (5.4)$$

Here,  $f_R$  is the fraction of the instantaneous nonlinearity that is due to SRS and  $\Gamma(\tau, \tau_s)$  is a normalized response function that is related to the usual Raman response function  $h_R(\tau)$  through  $\Gamma(\tau, \tau_s) = \tau_s h_R(\tau, \tau_s)$ , where the normalization timescale  $\tau_s = \sqrt{\mathcal{F}|\beta_2|L/(2\pi)}$ . Modelling the silica fiber Fabry-Perot resonator of Ref. [81], we have  $f_R = 0.18$ ,  $\tau_s = 300$  fs, and we use the well-known multiple-vibrational mode model to evaluate the response function  $h_R(\tau)$  [94].

Figure 5.6(a) shows numerically simulated soliton steps as a function of the drift coefficient  $d$  in the presence of SRS. Comparing the results with those obtained in the absence of SRS [cf. Fig. 5.5(d)], we immediately notice two important differences. First, in accordance with corresponding experimental findings [81], we now find the steps to be asymmetric with  $d$ . Second, we observe that the soliton steps manifest themselves only when  $d < 0$ . These observations can be understood by recalling that the redshift induced by SRS gives rise to a time-domain

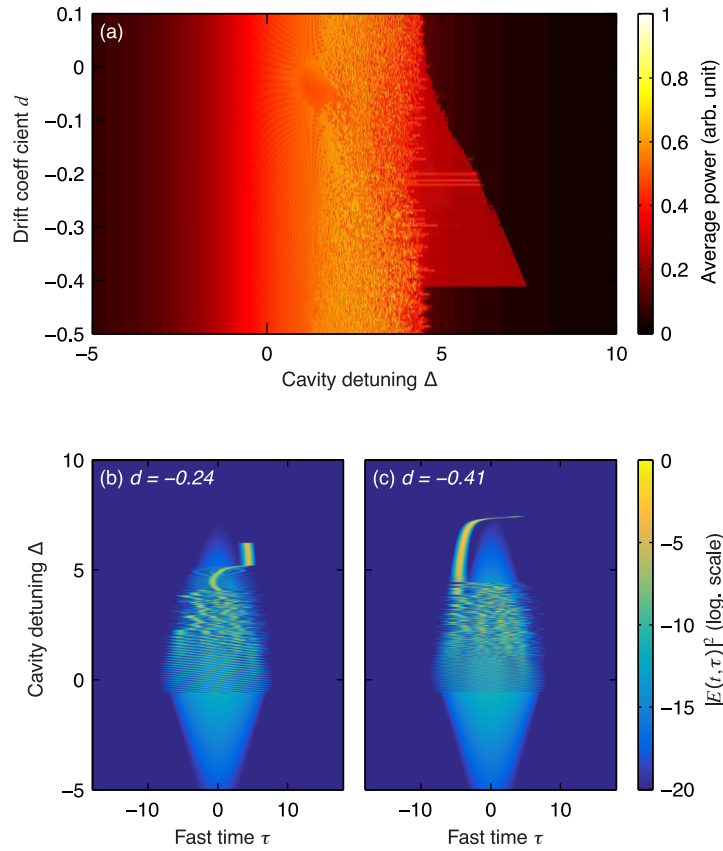


Figure 5.6: (a) Soliton steps as a function of the drift coefficient  $d$  when SRS is included in the cavity model. Note the different axes limits compared to Fig. 5.5(e). (b, c) Dynamical evolutions of the intracavity field intensity for drift coefficients as indicated. The Raman response function used in the simulations corresponds to fused silica [94], with  $f_R = 0.18$ . Other parameters as in Fig. 5.5.

drift [64, 93] that shifts the CS trapping positions towards the trailing edge of the driving pulse. For the parameters under study, the effect is so strong that a negative desynchronization is required to compensate for the SRS-induced drift and to push the trapping positions above the minimum level of soliton existence ( $S_{\min}$ ). This competition between SRS and desynchronization also explains why the range of soliton existence initially increases as the magnitude of the drift coefficient increases: a larger drift pushes the trapping positions further away from the minimum level of soliton existence, thus allowing the solitons to withstand the opposing effect of SRS over a wider range of detunings. (Note in this context that the SRS-induced soliton redshift is known to grow stronger with increasing detuning [93].) It is worth noting that the interplay between SRS and desynchronization

can be seen as an example of *asymmetric balance*, whereby two distinct mechanisms of explicit symmetry breaking (here SRS and desynchronization) compete and compensate for each other [92].

Another conspicuous effect of SRS is the overall reduction in the range of soliton existence. Indeed, whilst solitons are found to exist up to  $\Delta \approx 18.5$  in the absence of SRS [cf. Fig. 5.5(d)], they cease to exist already at  $\Delta \approx 7.5$  in the presence of SRS (under optimal de-synchronization). This behaviour agrees with recent research that shows SRS to limit the range of CS existence [93]. Figures 5.6(b) and (c) show typical evolutions of the intracavity field intensity for two different values of the drift coefficient. When the magnitude of the drift coefficient  $d$  is small, the CSs are formed on the trailing edge of the driving pulse due to SRS being the dominant mechanism of explicit symmetry breaking. As the magnitude of the drift coefficient increases, this ceases to be the case, and the CSs begin to predominantly form on the leading edge of the pulse. In both cases, we see complex dynamics that eventually lead to the CS ceasing to exist.

The results shown in Fig. 5.6(a) are in reasonable qualitative agreement with experimental results in [81]. In dimensional units corresponding to those experiments, our simulations predict that the CSs can exist over a 27 kHz range of desynchronization. While smaller than the 100 kHz observed in experiments, we attribute the discrepancy to differences in the driving pulse characteristics (e.g. peak power and phase profile) as well as the rate with which the detuning is changed. On the other hand, the (reduced) range of detunings over which the CSs exist in our simulations appears to be in very good agreement with the range observed experimentally. Taken together, we believe that the interplay between pump-cavity de-synchronization and SRS underpins the asymmetric soliton steps observed in Ref. [81]. Of course, we must emphasize that other higher-order effects that give rise to CS drift — such as e.g. higher-order dispersion or self-steepening — are also expected to give rise to asymmetric soliton steps, provided these effects are sufficiently strong. For the silica resonator used in [81], it is however reasonable to assume SRS to be the dominant perturbation.

## 5.4 Summary

We have performed a systematic numerical and theoretical investigation of the effects of desynchronization and drift on Kerr CS frequency comb generation in the presence of pulsed driving fields. Our results show that desynchronization

can impact the positioning, stability, and existence of CSs. In particular, we have shown that desynchronization can be leveraged to ensure the generation of single-soliton states via two different mechanisms depending on the cavity detuning. We have also studied the interplay between SRS and pump-cavity desynchronization, obtaining strong evidence that asymmetric soliton steps observed in recent experiments arise precisely due to such interplay [40].

## Chapter 6

# Internally pumped optical parametric oscillation in $\chi^{(2)}$ microresonators

In the preceding Chapters, we focused on the dynamics of structures present in third-order, Kerr nonlinear resonators. High-Q microresonators exhibiting third-order nonlinearity have attracted particular attention in the area of frequency comb generation due to their ability to enable strong nonlinear interactions at low pump powers [64, 95]. The generation of such microresonator frequency combs is understood to be intimately related to the temporal CSs described in the preceding Chapters [24]: a periodic train of CSs extracted from the resonator corresponds to a frequency comb in the spectral domain.

Interestingly, recent studies have demonstrated that it is also possible to generate frequency combs in resonators dominated by the second-order  $\chi^{(2)}$  nonlinearity: experimental observations have been reported in resonators designed for second-harmonic generation (SHG) [36, 96], parametric down-conversion (PDC) [97], and the electro-optic effect [98, 99]. The first experimental demonstrations of comb generation via SHG were reported in a macroscopic free-space system under conditions of large phase mismatch [96] – a regime well-known to *mimic* the  $\chi^{(3)}$  Kerr nonlinearity [100]. Later studies [36] unveiled that frequency combs can be generated even under conditions of perfect phase-matching through so-called internally-pumped optical parametric oscillation (OPO) [101, 102]: the second-harmonic signal acts as an internally-generated pump for a PDC process that produces equally-spaced spectral sidebands around the pump [see Fig. 6.1(a)].

Second-order resonators offer specific advantages over their third-order counterparts. Indeed, the second-order susceptibility can be orders of magnitude stronger than the third-order susceptibility, allowing stronger interactions at low pump powers. These  $\chi^{(2)}$  resonators also allow access to regions of the electromagnetic spectrum which have been hard to explore in  $\chi^{(3)}$  resonators. Firstly, because the parametric processes achievable in second-order nonlinear resonators allow an external pump to be converted in order to internally pump a resonance in another region of the spectrum. In turn, sidebands are generated around both the external pump and the parametric signal. Though similar internal pumping functions can be achieved in third-order resonators via Brillouin or Raman scattering [103, 104], sidebands will not form around the external pump as they do with second-order cavity systems and the small frequency shifts prevent access to significantly new spectral regions. Also, whilst generation of frequency combs in Kerr nonlinear resonators typically requires anomalous dispersion – thus further limiting the accessible spectra regions – second-order resonators can permit comb generation even in the regime of normal dispersion [24, 36, 62].

In this chapter, we are interested in comb generation via cavity-enhanced SHG. Whilst the initial demonstrations of comb generation in systems designed for cavity-enhanced SHG were achieved using macroscopic free-space resonators [36], recent experiments performed in periodically-poled waveguide Fabry-Perot resonators have shown strong evidence that the concept can be translated into a miniaturised format [37, 38]. Interestingly,  $\chi^{(2)}$  comb generation has not yet been widely studied in monolithic whispering gallery mode resonators (WGM). Such WGM resonators correspond to axially-symmetric dielectric structures where total internal reflection confines the internal field to modes around the circumference of the device. Simple examples include cylindrical resonators [105] and microspheres [106, 107] that can be constructed easily from optical fibre, while shapes such as microtoroids [108, 109] and microdiscs [26, 110–112] (like the one employed in our experiment) often require more involved fabrication techniques. The extremely low scattering loss and potentially low material absorption allow these resonators to offer superior finesses compared to alternative resonator platforms. Coupling high finesse and a small mode volume enables WGM resonators to facilitate strong nonlinear interactions [95]. These platforms have been used successfully to perform SHG and PDC [25–29], though somewhat surprisingly, no signals of comb formation have been observed as of yet. In this chapter, we will demonstrate that comb formation via cavity SHG can be achieved in a monolithic whispering-gallery-mode microresonator.

## 6.1 Illustrative simulations of a doubly resonant $\chi^{(2)}$ cavity

The cavity enhanced SHG system we consider in this chapter corresponds to a so-called doubly resonant configuration where spectral components around both the fundamental pump frequency and the internally generated second-harmonic frequency are resonant in the cavity as shown schematically in Fig. 6.1.

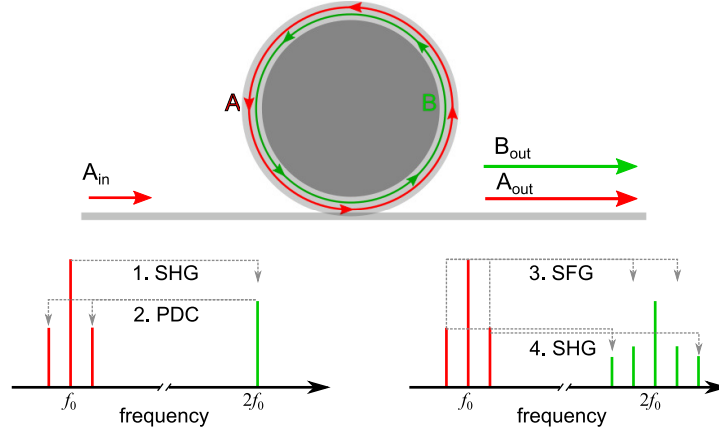


Figure 6.1: Top: Schematic illustration of the doubly resonant  $\chi^{(2)}$  cavity system. Bottom: Schematic showing generation of spectral sidebands around the fundamental and second-harmonic frequencies  $f_0$  and  $2f_0$ , respectively. SFG: sum-frequency generation.

Accordingly, both fields obey the associated resonator boundary conditions which relate the slowly-varying intracavity field envelopes  $A_m$  and  $B_m$  at the end of the  $m_{th}$  trip around the cavity to the field at the beginning of the next round trip [113]:

$$A_{m+1}(0, \tau) = \sqrt{\rho_1} A_m(L, \tau) e^{-i\delta_1} + \sqrt{\theta} A_{in}, \quad (6.1a)$$

$$B_{m+1}(0, \tau) = \sqrt{\rho_2} A_m(L, \tau) e^{-i\delta_2}. \quad (6.1b)$$

Here,  $\rho_1$  and  $\rho_2$  represent the portions of the fields which remain inside the cavity at  $\omega_0$  and  $2\omega_0$ , respectively, while  $\theta$  is the power transmission of the external cw driving field and  $\delta_{1,2}$  represent the respective phase detunings. The detuning  $\delta_2$  is related to  $\delta_1$  and the wave vector mismatch  $\Delta\beta$  via the relationship  $\delta_2 = 2\delta_1 + \Delta\beta L$  [114].

As stated in Subsection 2.5.4, the set of coupled equations Eqs. (2.21) can be used to model the propagation of light in a second-order nonlinear waveguide

system [43, 115]. Together with Eqs. (6.1), we can model the spectral and temporal dynamics of second-order nonlinear resonators. In the mean-field limit however, the high finesse allows the boundary and propagation equations to be merged into a set of two coupled mean-field equations [113, 114]:

$$t_R \frac{\partial A}{\partial t} = \left[ -\alpha_1 - i\delta_1 - i \frac{\beta_{2A} L}{2} \frac{\partial^2}{\partial \tau^2} \right] A + i\kappa L B A^* + \sqrt{\theta} A_{in}, \quad (6.2a)$$

$$t_R \frac{\partial B}{\partial t} = \left[ -\alpha_2 - i\delta_2 - \Delta\beta_1 L \frac{\partial}{\partial \tau} - i \frac{\beta_{2B} L}{2} \frac{\partial^2}{\partial \tau^2} \right] B + i\kappa L A^2. \quad (6.2b)$$

Here,  $\kappa$  is assumed to be real and corresponds to the nonlinear coupling coefficient defined by Eq. (2.22). Simulations of the coupled mean-field equations revealed that a doubly resonant SHG system can produce optical frequency combs via internally pumped OPO [113]. The external pump which is coupled into the cavity first undergoes SHG under phase matched conditions ( $\Delta\beta = 0$  and  $\delta_2 = 2\delta_1$ ) whereupon the second harmonic will act as an internally generated pump for a PDC process which creates side bands about the external pump [see Fig. 6.1].

To illustrate the comb formation dynamics, we have performed numerical simulations of Eqs. (6.2) using parameters estimated for the experimental parameters present in our work. Our resonator has a cavity length of  $L \approx 11.9\text{mm}$  and a finesse of  $\mathcal{F} = 2300 = \pi/\alpha_1$ . For simplicity we assume  $\alpha_1 = \alpha_2$  and the cavity is critically coupled ( $\alpha_1 = \theta$ ). We drive our system with 1064 nm light with an input power of  $P_{in} = 100\text{mW}$  chosen to approximate our experiment. Since we do not have knowledge of the spatial mode in which our experiments operate, we use dispersion parameters corresponding to those obtained for bulk lithium niobate using the Sellmeier equation:  $\beta_{2B} = .714\text{ps}^2/\text{km}$ ,  $\beta_{2A} = .234\text{ps}^2/\text{km}$ ,  $\Delta\beta_1 = 792\text{ps}/\text{m}$  and  $\kappa = 11.14\text{W}^{-1/2}\text{m}^{-1}$  [43]. Figure 6.2 shows spectra around the pump and the second harmonic resulting from a detuning scan which begins blue detuned and is stopped at the normalised pump detuning value of  $\delta = -0.002$ . Scanning speed is noted not to effect the outcome, rather is only used in simulations for congruity with experiments. This field is then allowed to reach an approximate steady state for 40,000 round trips, after which, a stable temporal pattern has formed, and spectral sidebands have grown around the pump and the second harmonic.

These results show that a resonator in the mean-field limit which is near phase matching between the pump and second harmonic can indeed support combs around the fundamental and the internally generated second harmonic. The phase matching condition for this process, as stated in Subsection 2.5.2, requires that the wave number mismatch  $\Delta\beta$  be very close to zero in order to achieve efficient

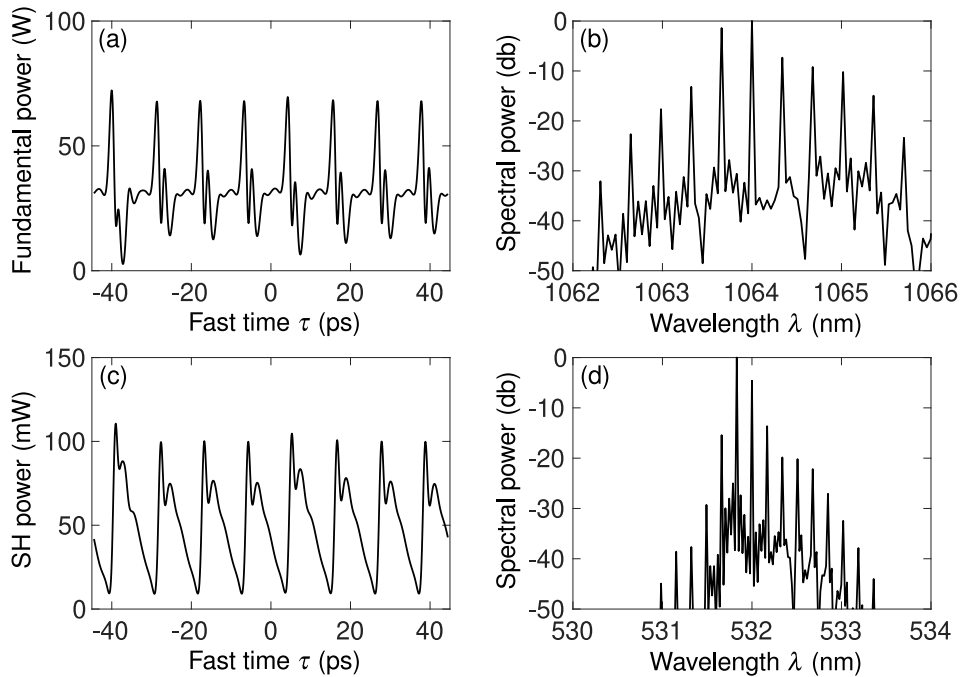


Figure 6.2: Intracavity field profiles for (a) pump and (c) second harmonic resulting from detuning scan stopped at  $\delta = -0.002$  and allowed to come to steady-state. (b) and (d) show the corresponding spectra.

frequency conversion. With these results demonstrating the feasibility of comb formation in monolithic WGM resonators, which are well modelled by the mean-field model [113], we developed an experiment in order to demonstrate the phenomenon.

## 6.2 Experimental methods and results

In this Section, we report on experimental observations of internally pumped OPO and the initial stages of comb formation in a naturally phase matched lithium niobate WGM resonator. Our experimental configuration, which is schematically illustrated in Fig. 6.3, is similar to the one used previously for observations of naturally-phase matched SHG in WGM resonators [26], though we note that no signatures of comb formation were detected in the study reported in ref. [26]. The resonator used was fabricated from a  $z$ -cut, 5% MgO-doped congruent lithium niobate window via single-point diamond turning and subsequent mechanical polishing. It has a radius of 1.9 mm, corresponding to a FSR of about 11.2 GHz. We

measured a typical resonance width to be about 5 MHz at the driving wavelength of 1064 nm, corresponding to a Q-factor of  $5.6 \times 10^7$  and a finesse of 2300.

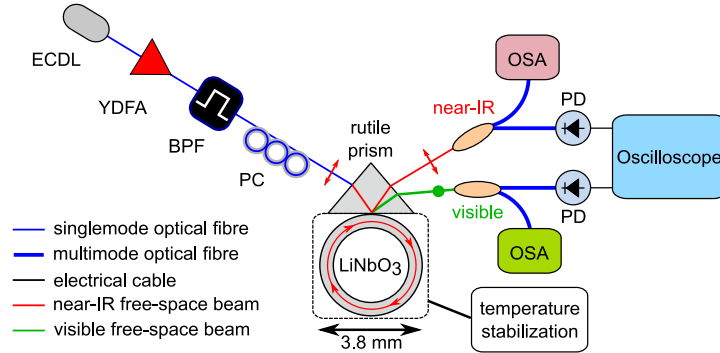


Figure 6.3: Schematic illustration of the experimental setup. ECDL, external-cavity diode laser; YDFA, ytterbium-doped fibre amplifier; BPF, band-pass filter; PC, polarization controller; OSA, optical spectrum analyzer; PD, photodetector.

Our driving source is an external cavity diode laser that is tunable from 1030 nm to 1070 nm. An ytterbium-doped fibre amplifier is used to amplify the laser output, and a tunable bandpass filter is used to remove amplified spontaneous emission. The pump is coupled into the resonator using frustrated total internal reflection from a rutile prism; a pigtailed ferrule and a GRIN lens is used to focus the pump on the backside of the prism. The beam input angle and divergence, as well as the size of the beam at the back face of the prism can all be tuned to achieve optimum coupling of the pump to the cavity. At the output of the prism, we detect the signals around the pump (near-IR) and its second harmonic (visible) using two photodetectors connected to an oscilloscope as well as two optical spectrum analyzers (OSAs) that operate in the near-IR and the visible, respectively.

To achieve natural phase-matching for SHG, the pump is coupled into an ordinary polarized mode (polarization perpendicular to the optical axis), whilst the second-harmonic is generated in an extra-ordinary mode (polarization along the optical axis). Due to the birefringence of lithium niobate, heating the crystal structure changes the refractive index experienced by fields in the orthogonally polarised modes with respect to each other [116]. This enables us to tune the temperature until the refractive indices experienced by the pump and the second harmonic are the same, satisfying the phase-matching condition  $2\beta(\omega_p) \approx \beta(2\omega_p)$ . The resonator is mounted on a brass rod whose temperature is stabilized to a set

level so as to thermally tune the phase-matching condition. We achieve a temperature accuracy of  $0.01^\circ\text{C}$  by employing a PID controlled resistive heating coil which is wrapped around the brass mounting rod. By testing several different temperatures, we found that a temperature of approximately  $94^\circ\text{C}$  yielded optimal SHG. We are confident in this value as it is close to the phase-matching temperature found in [26]. Additional, fine thermal control is achieved by shining a blue laser with variable intensity directly onto the resonator mode volume.

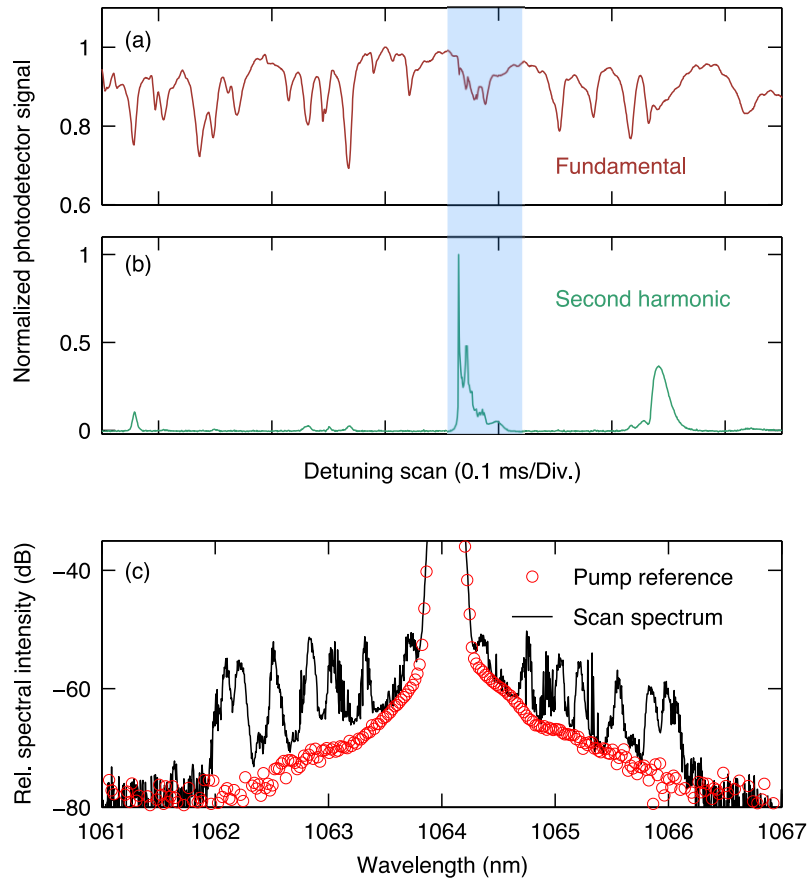


Figure 6.4: (a) Fundamental and (b) second harmonic intensity measured at the resonator output as the laser frequency is linearly scanned in time. Both curves are normalized to unity. (c) Solid black curve shows the optical spectrum measured around the fundamental wavelength at the resonator output when the laser frequency is scanned over a single cavity resonance indicated by the shaded area in (a) and (b). The open red circles depict the pump spectrum for reference.

With the temperature stabilized at  $94^\circ\text{C}$ , we find that several different mode families produce observable SHG. Figures 6.4(a) and (b) show illustrative oscillo-

scope recordings of the fundamental and second-harmonic intensities, respectively, when the laser frequency is scanned over several modes. Here the fundamental power right before the pigtailed ferrule was measured to be about 100 mW (same power used in all of our measurements). Losses through the prism coupling scheme we employed are expected to be large, though a realistic value for the input power is difficult to measure and therefore difficult to extract for comparison to the simulations shown in Fig. 6.2. Though the realistic input power level is expected to decrease from the measured 100 mW, at this power level, the SHG produced by some of the resonator modes is sufficiently strong so as to act as an internally-generated pump for an OPO process, giving rise to spectral sidebands around the pump. Indeed, Fig. 6.4(c) shows a spectral measurement around the pump, obtained as the pump frequency is scanned back and forth over one of the cavity resonances [indicated by the shaded area in Figs. 6.4(a) and (b)]. The generation of new spectral components around the pump is obvious. Note that the OSA sweep speed is much slower than the pump frequency scan, and so the spectrum in Fig. 6.4(c) traces out the envelope of all the different signals that can be generated at different detunings. Moreover, the resolution of our OSA is larger than the 11.2 GHz FSR of the resonator, prohibiting us from distinguishing the presence of individual lines with that spacing.

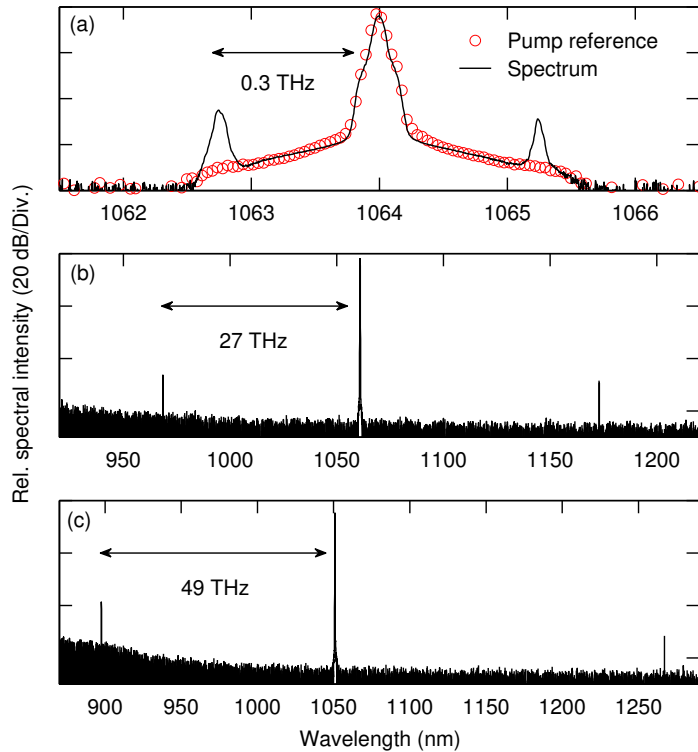


Figure 6.5: Experimentally measured spectra around the pump obtained for different pump wavelengths: (a) 1064 nm, (b) 1061 nm, (c) 1051 nm. The open red circles in (a) indicate the pump spectrum for reference.

To observe steady-state signals, we tune the pump laser into selected resonances from the blue, leveraging passive thermal locking [117]. For each resonance, we fine-adjust the coupling and resonator temperature so as to optimise nonlinear frequency conversion. Figures 6.5(a)–(c) show illustrative examples of spectra measured around the pump for different pump wavelengths. We clearly see optical sidebands generated via the PDC of the internally-generated SHG signal. By pumping different WGM resonances, we can observe a wide variety of different sideband frequency shifts, ranging from hundreds of GHz [Fig. 6.5(a)] to almost 50 THz [Fig. 6.5(c)]. Even when pumping a single resonance, we find that small adjustments of the pump-resonator detuning can yield sidebands with noticeably different frequency shifts.

By optimizing the pump wavelength and polarization, we are able to observe the cascaded generation of several sideband pairs. Figures 6.6(a) and (b) show illustrative spectra measured around the pump and the second-harmonic, respectively, when operating under such conditions. We clearly see the emergence of

second-order sidebands around the fundamental, representing the initial stages of quadratic comb generation [36]. New frequency components are also generated around the second-harmonic [Fig. 6.6(b)] via sum-frequency generation and SHG processes involving the spectral components around the fundamental. We must note that the resolution of our spectral measurements around the second-harmonic is limited by the OSA used in that frequency range.

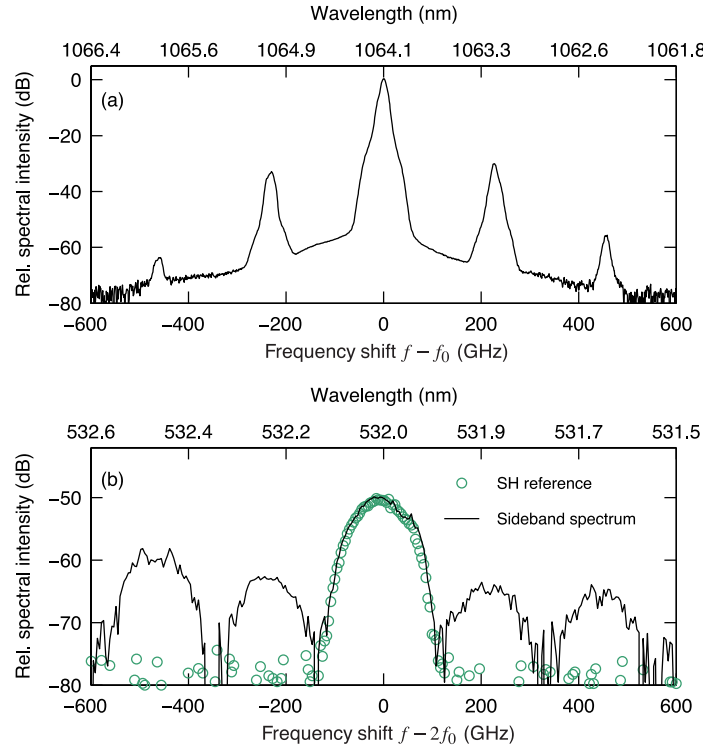


Figure 6.6: Experimentally measured spectrum around the (a) pump and (b) second-harmonic wavelengths. For reference, the green open circles in (b) show the second-harmonic (SH) spectrum in the absence of sidebands around the fundamental, normalized such that its noise floor is similar to the main recording shown as the black solid curve.

Figure 6.7 shows an additional example of the initial stages of quadratic comb generation. Here we see six pairs of spectral sidebands around the pump [Fig. 6.7(a)], spaced from one another by about 100 GHz in frequency (corresponding to nine free-spectral ranges). Because of the smaller sideband spacing compared to results shown in Fig. 6.6, we are not able to resolve the individual sidebands around the second-harmonic; rather, their presence is manifest in the broadening of the second-harmonic spectrum [Fig. 6.7(b)].

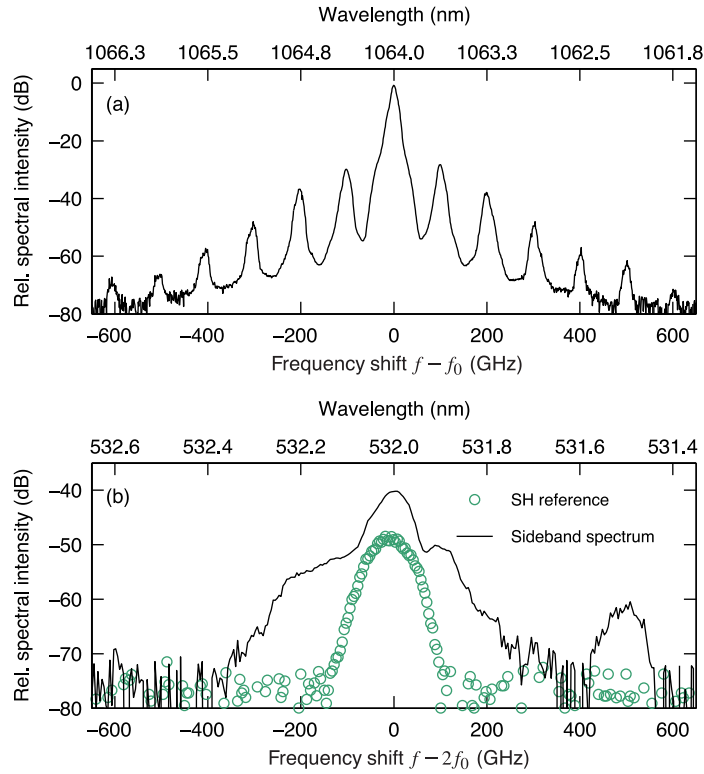


Figure 6.7: Experimentally measured spectrum around the (a) pump and (b) second-harmonic wavelengths. For reference, the green open circles in (b) show the second-harmonic (SH) spectrum in the absence of sidebands around the fundamental, normalized such that its noise floor is similar to the main recording shown as the black solid curve.

Quantitative comparison between our experimental findings and results pertaining to theoretical studies of the models described in this Chapter, e.g. [43, 113, 118, 119], is prohibited by poor knowledge over salient model parameters. In particular, our current experimental configuration does not allow us to identify the precise mode families involved in the nonlinear interactions, which results in significant uncertainty in the nonlinear coupling coefficients. Moreover, we do not currently have the capability to measure the value of the pump-cavity detuning nor the residual phase-mismatch, both of which can significantly influence the nonlinear cavity dynamics. We must nevertheless emphasize that the experimental observations reported above cannot be ascribed to direct  $\chi^{(3)}$  Kerr nonlinearity. Indeed, lithium niobate exhibits very large normal dispersion around 1060 nm, which is prohibitive for the phase-matching of degenerate four-wave mixing. The

fact that our observations of sideband generation is always correlated with strong SHG provides further evidence of the sidebands'  $\chi^{(2)}$  origins.

While our present experimental configuration permits us to reliably generate sidebands around the pump and the second-harmonic, we are unable to maintain stable operation for more than some tens of seconds at a time. In addition to sub-optimal thermal isolation, the linewidth of our pump laser ( $\sim 200$  kHz) necessitates sacrifices with regards to the resonator Q-factor, which in turn leads to increased pump power requirements that can impede system stability. Recently, encouraging results with a 2 mW comb generation power threshold was reported in a system otherwise similar to ours but with a better resonator Q-factor and pump laser linewidth [120].

### **6.3 Summary**

We have reported on the experimental observation of internally-pumped parametric oscillation and initial stages of quadratic comb formation in a  $\chi^{(2)}$  WGM microresonator. Whilst our current experimental configuration has enabled the proof-of-principle demonstrations reported in this work, there are a number of improvements that are left for future work. For example, operation in the fundamental mode family is envisaged to significantly enhance the nonlinear interactions, while better temperature control is expected to improve the phase-matching as well as the overall system stability [41].

## Chapter 7

# Conclusions

In this Thesis, we have theoretically and experimentally investigated novel dynamics in nonlinear resonators. We first investigated the interactions between Kerr CSs and pulsed driving fields and detailed the dynamics of intensity trapping of CSs. We demonstrated via numerical simulations that CSs which are synchronously pumped with a train of pulses will be attracted toward and trap at a specific "preferred" value of the driving field. We showed that this trapping value arises due to a spontaneous symmetry breaking instability and is determined by the cavity detuning. Assuming a driving field profile such that the CS can move toward and be trapped at this value, it will remain at the trapping position indefinitely.

We built on the ability to trap CS with pulsed driving fields and extended it to encompass the effects of desynchronization, which is generally present in experimental configurations. We found that small amounts of desynchronization between the CS and the driving pulse has the effect of shifting the steady-state trapping positions identified in Chapter 4. In fact, we were able to show that desynchronization can be used to ensure single-soliton operation. By shifting the trapping positions, you can shift one to a position where CSs cannot exist, leaving a single position available to be occupied by a CS. We then investigated the interplay of stimulated Raman scattering with desynchronization. We reported on a strong qualitative agreement with experimental observations which demonstrated asymmetric soliton steps with respect to desynchronization in a pulsed driving system [81]. We demonstrated that the combination of desynchronization and other, competing effects can lead to such asymmetric steps. We numerically investigated the effects of desynchronization on the trapping of CSs and the potential benefits of engineering desynchronization in order to ensure single soliton operation—the preferred operating scheme for frequency comb applications.

We then reported on preliminary experimental investigations into frequency comb generation in  $\chi^{(2)}$  microresonators. We demonstrated the experimental observation of internally pumped parametric oscillations in a lithium niobate whispering-gallery-mode resonator. We were able to produce sidebands around the pump and the second harmonic, and cascade the processes generating these sidebands in the initial stages of comb formation. We demonstrated that frequency comb formation can be achieved in a naturally phase matched microresonator dominated by the second order nonlinearity, greatly increasing spectral access for comb generation and applications.

As the study into CSs in the presence of pulsed or amplitude modulated driving fields is still attracting significant interest, there is naturally still much to be explored. The investigation into desynchronization and its interplay with SRS was a step toward accurate models and predictions of real experimental systems, though there are still many interactions that have not been studied in the context of pulsed driving. The addition of phase modulations and higher-order dispersion would need to be investigated in order to gain a more complete understanding of experimentally achievable systems. Although existing experimental measurements are in good qualitative agreement with our theoretical predictions, there has yet to be demonstrations of intensity trapping of CSs that can be directly compared to the predictions reported in this Thesis. Though anecdotal evidence has been observed in similar systems, a specific experimental investigation into the interplay of trapping and desynchronization would provide a means by which to improve current theories.

Our experimental observations of the initial stages of comb formation in a quadratically nonlinear microresonator, though successful, could be improved in a number of ways for future work. Knowledge of the coupled mode family, and the ability to better couple into a desired mode family could greatly increase the nonlinear interactions. More accurate temperature control and measurement would greatly increase the stability and reliability of the experiment. Our work nevertheless demonstrates the viability of observing and studying cascaded quadratic nonlinear phenomena in WGM microresonators.

Recent works have also demonstrated the intriguing possibility of merging the two areas covered in this Thesis. The generation of CS combs in quadratically nonlinear microresonators has begun to shed light on the dynamics of temporal localised structures in quadratically nonlinear cavities [119, 121, 122]. These quadratic CSs bring with them the benefit of low pumping thresholds due to the

stronger second-order nonlinearity, while also exhibiting very high conversion efficiency from the pump to the CS state. There has also been an investigation into the interplay of second and third-order nonlinearities which occur simultaneously in a cavity [123]. Due to the fact that soliton microcombs have gained immense interest in Kerr cavities, and the fact that all materials exhibit the third-order nonlinear susceptibility, studies such as these are vital to gaining a full understanding of comb formation in quadratic media.



# Bibliography

- [1] T. H. Maiman. “Stimulated optical radiation in ruby”. In: *Nature* 187 (1960), pp. 493–494.
- [2] e. P. Franken et al. “Generation of optical harmonics”. In: *Physical Review Letters* 7 (1961), p. 118.
- [3] J. A. Giordmaine and R. C. Miller. “Tunable coherent parametric oscillation in LiNb O 3 at optical frequencies”. In: *Physical Review Letters* 14 (1965), p. 973.
- [4] S. Harris, M. Oshman, and R. Byer. “Observation of tunable optical parametric fluorescence”. In: *Physical Review Letters* 18 (1967), p. 732.
- [5] R. Stolen and E. Ippen. “Raman gain in glass optical waveguides”. In: *Applied Physics Letters* 22 (1973), pp. 276–278.
- [6] R. Stolen and A. Ashkin. “Optical Kerr effect in glass waveguide”. In: *Applied Physics Letters* 22 (1973), pp. 294–296.
- [7] R. H. Stolen. “The early years of fiber nonlinear optics”. In: *Journal of Lightwave Technology* 26 (2008), pp. 1021–1031.
- [8] J. K. Ranka, R. S. Windeler, and A. J. Stentz. “Visible continuum generation in air–silica microstructure optical fibers with anomalous dispersion at 800 nm”. In: *Optics letters* 25 (2000), pp. 25–27.
- [9] T. Birks, W. Wadsworth, and P. S. J. Russell. “Supercontinuum generation in tapered fibers”. In: *Optics letters* 25 (2000), pp. 1415–1417.
- [10] J. M. Dudley, G. Genty, and S. Coen. “Supercontinuum generation in photonic crystal fiber”. In: *Reviews of modern physics* 78 (2006), p. 1135.
- [11] T. W. Hänsch. “Nobel lecture: passion for precision”. In: *Reviews of Modern Physics* 78 (2006), p. 1297.

- [12] J. L. Hall. “Nobel Lecture: Defining and measuring optical frequencies”. In: *Reviews of Modern Physics* 78 (2006), p. 1279.
- [13] D. J. Jones et al. “Carrier-envelope phase control of femtosecond mode-locked lasers and direct optical frequency synthesis”. In: *Science* 288 (2000), pp. 635–639.
- [14] A. S. Davydov. “Solitons and energy transfer along protein molecules”. In: *Journal of Theoretical Biology* 66 (1977), pp. 379–387.
- [15] N. J. Zabusky and M. D. Kruskal. “Interaction of " solitons" in a collisionless plasma and the recurrence of initial states”. In: *Physical review letters* 15 (1965), p. 240.
- [16] Y. S. Kivshar and G. P. Agrawal. *Optical solitons: from fibers to photonic crystals*. Academic press, 2003.
- [17] J. H. Nguyen et al. “Collisions of matter-wave solitons”. In: *Nature Physics* 10 (2014), pp. 918–922.
- [18] J. Scott-Russell. “Report on waves”. In: *Proc. Roy. Soc. Edinburgh*. Vol. 319. 1844.
- [19] A. Scott. *Nonlinear science: emergence and dynamics of coherent structures*. Oxford Univ. Press, 2003.
- [20] G. P. Agrawal. *Nonlinear Fiber Optics*. 6th ed. Academic Press, 2019.
- [21] D. Mc Laughlin, J. V. Moloney, and A. C. Newell. “Solitary waves as fixed points of infinite-dimensional maps in an optical bistable ring cavity”. In: *Physical review letters* 51 (1983), p. 75.
- [22] S. Wabnitz. “Suppression of interactions in a phase-locked soliton optical memory”. In: *Opt. Lett.* 18 (1993), pp. 601–603.
- [23] F. Leo et al. “Temporal cavity solitons in one-dimensional Kerr media as bits in an all-optical buffer”. In: *Nature Photonics* 4 (2010), pp. 471–476.
- [24] T. Herr et al. “Temporal solitons in optical microresonators”. In: *Nature Photonics* 8 (2014), pp. 145–152.
- [25] V. S. Ilchenko et al. “Nonlinear Optics and Crystalline Whispering Gallery Mode Cavities”. In: *Phys. Rev. Lett.* 92 (2004), p. 043903.
- [26] J. U. Fürst et al. “Naturally Phase-Matched Second-Harmonic Generation in a Whispering-Gallery-Mode Resonator”. In: *Phys. Rev. Lett.* 104 (2010), p. 153901.

- [27] T. Beckmann et al. “Highly Tunable Low-Threshold Optical Parametric Oscillation in Radially Poled Whispering Gallery Resonators”. In: *Phys. Rev. Lett.* 106 (2011), p. 143903.
- [28] G. Schunk et al. “Interfacing transitions of different alkali atoms and telecom bands using one narrowband photon pair source”. In: *Optica* 2 (2015), pp. 773–778.
- [29] M. Förtsch et al. “Highly efficient generation of single-mode photon pairs from a crystalline whispering-gallery-mode resonator source”. In: *Phys. Rev. A* 91 (2015), p. 023812.
- [30] S.-K. Meisenheimer et al. “Continuous-wave optical parametric oscillation tunable up to an 8  $\mu\text{m}$  wavelength”. In: *Optica* 4 (2017), pp. 189–192.
- [31] P. Marin-Palomo et al. “Microresonator-based solitons for massively parallel coherent optical communications”. In: *Nature* 546 (2017), pp. 274–279.
- [32] J. Riemensberger et al. “Massively parallel coherent laser ranging using a soliton microcomb”. In: *Nature* 581 (2020), pp. 164–170.
- [33] J. K. Jang et al. “Temporal tweezing of light through the trapping and manipulation of temporal cavity solitons”. In: *Nature Communications* 6 (2015), p. 7370.
- [34] M. Malinowski et al. “Optical frequency comb generation by pulsed pumping”. In: *APL Photonics* 2 (2017), p. 066101.
- [35] F. Leo et al. “Dynamics of one-dimensional Kerr cavity solitons”. In: *Opt. Express* 21 (2013), pp. 9180–9191.
- [36] I. Ricciardi et al. “Frequency comb generation in quadratic nonlinear media”. In: *Phys. Rev. A* 91 (2015), p. 063839.
- [37] R. Ikuta et al. “Frequency comb generation in a quadratic nonlinear waveguide resonator”. In: *Opt. Express* 26 (2018), pp. 15551–15558.
- [38] M. Stefszky et al. “Towards optical-frequency-comb generation in continuous-wave-pumped titanium-indiffused lithium-niobate waveguide resonators”. In: *Phys. Rev. A* 98 (2018), p. 053850.
- [39] I. Hendry et al. “Spontaneous symmetry breaking and trapping of temporal Kerr cavity solitons by pulsed or amplitude-modulated driving fields”. In: *Physical Review A* 97 (2018), p. 053834.

- [40] I. Hendry et al. “Impact of desynchronization and drift on soliton-based Kerr frequency combs in the presence of pulsed driving fields”. In: *Physical Review A* 100 (2019), p. 023829.
- [41] I. Hendry et al. “Experimental observation of internally pumped parametric oscillation and quadratic comb generation in a  $\chi(2)$  whispering-gallery-mode microresonator”. In: *Optics Letters* 45 (2020), pp. 1204–1207.
- [42] D. J. Griffiths. *Introduction to Electrodynamics*. 4th ed. Boston, MA: Pearson, 2013.
- [43] F. Leo et al. “Walk-Off-Induced Modulation Instability, Temporal Pattern Formation, and Frequency Comb Generation in Cavity-Enhanced Second-Harmonic Generation”. In: *Phys. Rev. Lett.* 116 (2016), p. 033901.
- [44] N. Akhmediev and A. Ankiewicz. *Dissipative solitons: from optics to biology and medicine*. Vol. 751. Springer Science & Business Media, 2008.
- [45] L. F. Stokes, M. Chodorow, and H. J. Shaw. “All-single-mode fiber resonator”. In: *Optics Letters* 7 (1982), pp. 288–290.
- [46] S. Coen and M. Erkintalo. “Universal scaling laws of Kerr frequency combs”. In: *Optics letters* 38 (2013), pp. 1790–1792.
- [47] V. Braginsky, M. Gorodetsky, and V. Ilchenko. “Quality-factor and nonlinear properties of optical whispering-gallery modes”. In: *Physics letters A* 137 (1989), pp. 393–397.
- [48] F. A. Jenkins and H. E. White. *Fundamentals of optics*. Tata McGraw-Hill Education, 1937.
- [49] N. L. B. Sayson et al. “Widely tunable optical parametric oscillation in a Kerr microresonator”. In: *Opt. Lett.* 42 (2017), pp. 5190–5193.
- [50] N. L. B. Sayson et al. “Octave-spanning tunable parametric oscillation in crystalline Kerr microresonators”. In: *Nature Photonics* 13 (2019), pp. 701–706.
- [51] O. Svelto and D. C. Hanna. *Principles of lasers*. Vol. 1. Springer, 2010.
- [52] K. Ikeda. “Multiple-valued stationary state and its instability of the transmitted light by a ring cavity system”. In: *Opt. Commun.* 30 (1979), pp. 257–261.
- [53] F. M. Mitschke and L. F. Mollenauer. “Discovery of the soliton self-frequency shift”. In: *Optics letters* 11 (1986), pp. 659–661.

- [54] K. Tai, A. Hasegawa, and A. Tomita. “Observation of modulational instability in optical fibers”. In: *Physical review letters* 56 (1986), p. 135.
- [55] L. A. Lugiato and R. Lefever. “Spatial Dissipative Structures in Passive Optical Systems”. In: *Phys. Rev. Lett.* 58 (1987), pp. 2209–2211.
- [56] M. Haelterman, S. Trillo, and S. Wabnitz. “Dissipative modulation instability in a nonlinear dispersive ring cavity”. In: *Optics Communications* 91 (1992), pp. 401–407.
- [57] G. Steinmeyer et al. “Dynamical pulse shaping in a nonlinear resonator”. In: *Phys. Rev. A* 52 (1995), pp. 830–838.
- [58] S. Coen and M. Haelterman. “Modulational instability induced by cavity boundary conditions in a normally dispersive optical fiber”. In: *Physical review letters* 79.21 (1997), p. 4139.
- [59] F. Hopf et al. “Anomalous switching in dispersive optical bistability”. In: *Optics Communications* 31 (1979), pp. 245–250.
- [60] A. Kaplan and P. Meystre. “Directionally asymmetrical bistability in a symmetrically pumped nonlinear ring interferometer”. In: *Optics Communications* 40 (1982), pp. 229–232.
- [61] H. Gibbs. *Optical bistability: controlling light with light*. Elsevier, 2012.
- [62] S. Coen et al. “Modeling of octave-spanning Kerr frequency combs using a generalized mean-field Lugiato-Lefever model”. In: *Opt. Lett.* 38 (2013), pp. 37–39.
- [63] P. K. A. Wai, H. H. Chen, and Y. C. Lee. “Radiations by "solitons" at the zero group-dispersion wavelength of single-mode optical fibers”. In: *Phys. Rev. A* 41 (1990), pp. 426–439.
- [64] C. Milián et al. “Solitons and frequency combs in silica microring resonators: Interplay of the Raman and higher-order dispersion effects”. In: *Phys. Rev. A* 92 (2015), p. 033851.
- [65] M. Anderson et al. “Coexistence of Multiple Nonlinear States in a Tristable Passive Kerr Resonator”. In: *Phys. Rev. X* 7 (2017), p. 031031.
- [66] F. Copie et al. “Competing Turing and Faraday instabilities in longitudinally modulated passive resonators”. In: *Physical Review Letters* 116 (2016), p. 143901.

- [67] N. N. Akhmediev. “Spatial solitons in Kerr and Kerr-like media”. In: *Optical and Quantum Electronics* 30 (1998), pp. 535–569.
- [68] P. Grelu and N. Akhmediev. “Dissipative solitons for mode-locked lasers”. In: *Nature photonics* 6 (2012), pp. 84–92.
- [69] I. V. Barashenkov and Y. S. Smirnov. “Existence and stability chart for the ac-driven, damped nonlinear Schrödinger solitons”. In: *Phys. Rev. E* 54 (1996), pp. 5707–5725.
- [70] S. Barland et al. “Cavity solitons as pixels in semiconductor microcavities”. In: *Nature* 419 (2002), pp. 699–702.
- [71] W. Firth and A. Scroggie. “Optical bullet holes: robust controllable localized states of a nonlinear cavity”. In: *Physical review letters* 76.10 (1996), p. 1623.
- [72] T. Maggipinto et al. “Cavity solitons in semiconductor microresonators: Existence, stability, and dynamical properties”. In: *Phys. Rev. E* 62 (2000), pp. 8726–8739.
- [73] F. Pedaci et al. “Positioning cavity solitons with a phase mask”. In: *Applied physics letters* 89.22 (2006), p. 221111.
- [74] E. Caboche et al. “Microresonator defects as sources of drifting cavity solitons”. In: *Physical review letters* 102.16 (2009), p. 163901.
- [75] T. Ackemann, W. Firth, and G.-L. Oppo. “Fundamentals and applications of spatial dissipative solitons in photonic devices”. In: *Advances in atomic, molecular, and optical physics* 57 (2009), pp. 323–421.
- [76] J. K. Jang et al. “Ultraweak long-range interactions of solitons observed over astronomical distances”. In: *Nature Photonics* 7 (2013), pp. 657–663.
- [77] M. Erkintalo, S. G. Murdoch, and S. Coen. “Phase and intensity control of dissipative Kerr cavity solitons”. In: *Journal of the Royal Society of New Zealand* (2021), pp. 1–19.
- [78] J. García-Mateos, F. C. Bienzobas, and M. Haelterman. “Optical bistability and temporal symmetry-breaking instability in nonlinear fiber resonators”. In: *Fiber and Integrated Optics* 14 (1995), pp. 337–346.
- [79] Y. Xu and S. Coen. “Experimental observation of the spontaneous breaking of the time-reversal symmetry in a synchronously pumped passive Kerr resonator”. In: *Opt. Lett.* 39 (2014), pp. 3492–3495.

- [80] P. Parra-Rivas et al. “Effects of inhomogeneities and drift on the dynamics of temporal solitons in fiber cavities and microresonators”. In: *Opt. Express* 22 (2014), pp. 30943–30954.
- [81] E. Obrzud, S. Lecomte, and T. Herr. “Temporal solitons in microresonators driven by optical pulses”. In: *Nature Photonics* 11 (2017), pp. 600–607.
- [82] X. Xue, X. Zheng, and A. M. Weiner. “Soliton trapping and comb self-referencing in a single microresonator with  $\chi(2)$  and  $\chi(3)$  nonlinearities”. In: *Opt. Lett.* 42 (2017), pp. 4147–4150.
- [83] E. Obrzud et al. “A microphotonic astrocomb”. In: *Nature Photonics* 13 (2019), pp. 31–35.
- [84] S. Fedorov et al. “Effects of spatial inhomogeneities on the dynamics of cavity solitons in quadratically nonlinear media”. In: *Phys. Rev. E* 64 (2001), p. 036610.
- [85] J. Javaloyes et al. “Dynamics of Localized Structures in Systems with Broken Parity Symmetry”. In: *Phys. Rev. Lett.* 116 (2016), p. 133901.
- [86] J. P. Gordon and H. A. Haus. “Random walk of coherently amplified solitons in optical fiber transmission”. In: *Opt. Lett.* 11 (1986), pp. 665–667.
- [87] S. Coen et al. “Convection versus Dispersion in Optical Bistability”. In: *Phys. Rev. Lett.* 83 (1999), pp. 2328–2331.
- [88] S. Barland et al. “Temporal localized structures in optical resonators”. In: *Advances in Physics: X* 2 (2017), pp. 496–517.
- [89] D. C. Cole et al. “Kerr-microresonator solitons from a chirped background”. In: *Optica* 5 (2018), pp. 1304–1310.
- [90] J. K. Jang et al. “Controlled merging and annihilation of localised dissipative structures in an AC-driven damped nonlinear Schrödinger system”. In: *New Journal of Physics* 18 (2016), p. 033034.
- [91] Y. Wang et al. “Universal mechanism for the binding of temporal cavity solitons”. In: *Optica* 4 (2017), pp. 855–863.
- [92] B. Garbin et al. “Asymmetric balance in symmetry breaking”. In: *Phys. Rev. Research* 2 (2020), p. 023244.
- [93] Y. Wang et al. “Stimulated Raman Scattering Imposes Fundamental Limits to the Duration and Bandwidth of Temporal Cavity Solitons”. In: *Phys. Rev. Lett.* 120 (2018), p. 053902.

- [94] D. Hollenbeck and C. D. Cantrell. “Multiple-vibrational-mode model for fiber-optic Raman gain spectrum and response function”. In: *J. Opt. Soc. Am. B* 19 (2002), pp. 2886–2892.
- [95] G. C. Righini et al. “Whispering gallery mode microresonators: fundamentals and applications”. In: *La Rivista del Nuovo Cimento* 34 (2011), pp. 435–488.
- [96] V. Ulvila et al. “Frequency comb generation by a continuous-wave-pumped optical parametric oscillator based on cascading quadratic nonlinearities”. In: *Opt. Lett.* 38 (2013), pp. 4281–4284.
- [97] S. Mosca et al. “Modulation Instability Induced Frequency Comb Generation in a Continuously Pumped Optical Parametric Oscillator”. In: *Phys. Rev. Lett.* 121 (2018), p. 093903.
- [98] A. Rueda et al. “Resonant electro-optic frequency comb”. In: *Nature* 568 (2019), pp. 378–381.
- [99] M. Zhang et al. “Broadband electro-optic frequency comb generation in a lithium niobate microring resonator”. In: *Nature* 568 (2019), pp. 373–377.
- [100] G. I. Stegeman, D. J. Hagan, and L. Torner. “ $\chi(2)$  cascading phenomena and their applications to all-optical signal processing, mode-locking, pulse compression and solitons”. In: *Optical and Quantum Electronics* 28 (1996), pp. 1691–1740.
- [101] M. A. M. Marte. “Competing nonlinearities”. In: *Phys. Rev. A* 49 (1994), R3166–R3169.
- [102] S. Schiller et al. “Subharmonic-pumped continuous-wave parametric oscillator”. In: *Applied Physics Letters* 68 (1996), pp. 3374–3376.
- [103] G. Lin et al. “Universal nonlinear scattering in ultra-high Q whispering gallery-mode resonators”. In: *Opt. Express* 24 (2016), pp. 14880–14894.
- [104] G. Lin, A. Coillet, and Y. K. Chembo. “Nonlinear photonics with high-Q whispering-gallery-mode resonators”. In: *Adv. Opt. Photon.* 9 (2017), pp. 828–890.
- [105] T. Birks, J. Knight, and T. Dimmick. “High-resolution measurement of the fiber diameter variations using whispering gallery modes and no optical alignment”. In: *IEEE Photonics Technology Letters* 12 (2000), pp. 182–183.

- [106] A. Chiasera et al. “Spherical whispering-gallery-mode microresonators”. In: *Laser & Photonics Reviews* 4 (2010), pp. 457–482.
- [107] J. Ward and O. Benson. “WGM microresonators: sensing, lasing and fundamental optics with microspheres”. In: *Laser & Photonics Reviews* 5 (2011), pp. 553–570.
- [108] D. Armani et al. “Ultra-high-Q toroid microcavity on a chip”. In: *Nature* 421 (2003), pp. 925–928.
- [109] T. Kippenberg, S. Spillane, and K. Vahala. “Kerr-nonlinearity optical parametric oscillation in an ultrahigh-Q toroid microcavity”. In: *Physical review letters* 93 (2004), p. 083904.
- [110] J. Sarma and K. Shore. “Electromagnetic theory for optical disc resonators”. In: *IEEE Proceedings J (Optoelectronics)* 132 (1985), pp. 325–330.
- [111] S. McCall et al. “Whispering-gallery mode microdisk lasers”. In: *Applied physics letters* 60 (1992), pp. 289–291.
- [112] M. Borselli et al. “Rayleigh scattering, mode coupling, and optical loss in silicon microdisks”. In: *Applied Physics Letters* 85 (2004), pp. 3693–3695.
- [113] F. Leo et al. “Frequency-comb formation in doubly resonant second-harmonic generation”. In: *Phys. Rev. A* 93 (2016), p. 043831.
- [114] X. Xue et al. “Second-harmonic-assisted four-wave mixing in chip-based microresonator frequency comb generation”. In: *Light: Science & Applications* 6 (2017), e16253–e16253.
- [115] A. V. Buryak et al. “Optical solitons due to quadratic nonlinearities: from basic physics to futuristic applications”. In: *Physics Reports* 370 (2002), pp. 63–235.
- [116] O. Gayer et al. “Temperature and wavelength dependent refractive index equations for MgO-doped congruent and stoichiometric LiNbO<sub>3</sub>”. In: *Applied Physics B* 91.2 (2008), pp. 343–348.
- [117] T. Carmon, L. Yang, and K. J. Vahala. “Dynamical thermal behavior and thermal self-stability of microcavities”. In: *Opt. Express* 12 (2004), pp. 4742–4750.
- [118] T. Hansson et al. “Single envelope equation modeling of multi-octave comb arrays in microresonators with quadratic and cubic nonlinearities”. In: *J. Opt. Soc. Am. B* 33 (2016), pp. 1207–1215.

- [119] A. Villois and D. V. Skryabin. “Soliton and quasi-soliton frequency combs due to second harmonic generation in microresonators”. In: *Optics express* 27 (2019), pp. 7098–7107.
- [120] J. Szabados et al. “Frequency Comb Generation via Cascaded Second-Order Nonlinearities in Microresonators”. In: *Phys. Rev. Lett.* 124 (2020), p. 203902.
- [121] T. Hansson et al. “Quadratic soliton combs in doubly resonant second-harmonic generation”. In: *Optics letters* 43 (2018), pp. 6033–6036.
- [122] A. W. Bruch et al. *Pockels Soliton Microcomb*. 2020. arXiv: 2004.07708 [physics.optics].
- [123] A. Villois et al. “Frequency combs in a microring optical parametric oscillator”. In: *Optics letters* 44 (2019), pp. 4443–4446.